Universidade do Minho
Escola de Engenharia

Aureliano da Costa Fertuzinhos

Experimental and numerical characterization of the viscoelastic behaviour of cartilages and soft tissues of the human nose

Outubro de 2017

DECLARAÇÃO

Nome: Aureliano da Costa Fertuzinhos

Endereço eletrónico: aurelianoscp1993@gmail.com   Telefone: 911743840

Bilhete de Identidade/Cartão do Cidadão: 14495782

Título da dissertação: Experimental and numerical characterization of the viscoelastic behaviour of cartilages and soft tissues of the human nose/Caracterização experimental e numérica do comportamento viscoelástico de cartilagens e tecidos moles do pavilhão nasal humano

Orientadores:

Professor Doutor Nuno Miguel Magalhães Dourado

Professor Doutor João Paulo Flores Fernandes

Ano de conclusão: 2017

Mestrado Integrado em Engenharia Biomédica – Biomateriais, Reabilitação e Biomecânica

Universidade do Minho, _____/_____/_____

Assinatura:

To my sister, my mother, and my godparents for their love and support.

To all those people who have inspired me.

ACKNOWLEDGEMENTS

providing me one of the most scary and challenging tasks of my life, and to prove, once again, that everything can be possible when Engineering and Medicine work together.

My friends know how important they are for me. I must recognize that sometimes I did not spend enough time with them, avoiding our nights out, dinners, coffees, but now you all are part of this. And it is done! I would like to express my gratitude to some specific people and, for that reason, I will share who they are. To my sweet team during these five years that we kindly call "Manos" (Filipa Vasques, Nuno Azevedo, and Raphael Espanha). There is no words to express how grateful I am for having you in my life, sharing knowledge and stories, amazing moments and confidences, *engineering mornings*,... You have been there for a long time, and I hope you can still be there for much longer.

My outstanding group "Gang das Taipas" (Joana, Abílio, Fábio, and Tiago) who always have been there for the craziest moments, to support me and advise me. "*Anyone knows when and where is the next barbeque?*". One word to you as well, volleyball group, I apologize for missing the games along this year. Thank you!

To Ana Sousa, my sweetheart, your manager is about to be master. Thank you for your patience and unwavering friendship. You are the person responsible for some of the happiest moments of my life. To David Sousa, my best friend, you were the best partner I ever had. To all my friends, all of you that I did not name, and classmates, you made these five years unforgettable.

For last and undoubtedly the most important, to my nuclear family. To my sister Verónica, my youngest inspiration, for all the encouragement, words of support, caution, and proud. To my mother, Maria Gracinda, for the patience, resilience, and unconditional love and support in all the moments of my life. To my godparents, Albertina and Aureliano, for making this academic experience possible (as well as many other experiences and learnings), for the unconditional love and support without requiring anything in return, for the stories of the past that helped me to grow up, for taking care of me...

I am very grateful to all the people and Institutions who contributed to the realization of this Thesis. Thank you very much!

Aureliano Fertuzinhos, October 2017

RESUMO

A cirurgia plástica facial, e em particular a área da rinoplastia, é indubitavelmente um mercado em crescimento. As técnicas cirúrgicas têm evoluído no sentido de dar resposta aos desejos mais específicos de cada paciente não só por razões funcionais, mas também para resolução de problemas estéticos. Atualmente, é uma área que movimenta muito dinheiro em todo o mundo, tornando-se numa evidente oportunidade científica e comercial.

O nariz humano está dividido em três regiões principais separadas por duas zonas de transição (áreas K e S) que são muito difíceis de manipular em períodos de recuperação pós-cirurgia. O comportamento viscoelástico de tecidos moles, especialmente o das cartilagens nasais e dos tecidos subcutâneo/adiposo adjacentes, é pouco conhecido. Atualmente, não existem estudos sobre a caracterização de propriedades mecânicas da cartilagem septal nem das cartilagens laterais superiores ou inferiores em fluência e relaxação (características de comportamentos viscoelásticos). A determinação de propriedades mecânicas em função da frequência de oscilação e da temperatura para estes mesmos materiais através de uma análise de DMA em tensão e compressão, assim como informações gerais sobre fenómenos de degradação térmica por DSC e TGA, também não são reportados. Assim sendo, parte desta dissertação pretende preencher esta lacuna da literatura, contribuindo para a compreensão da composição e arquitetura internas da cartilagem e da especificidade dos mecanismos ativados sob influência de uma tensão ou deformação constantes. Além disso, foram levadas a cabo simulações numéricas baseadas numa formulação matemática de híper-viscoelasticidade num *software* de elementos finitos desenvolvido na Instituição (V-Biomech) e foram encontrados os valores dos parâmetros que permitem replicar o comportamento experimental de fluência e relaxação de cartilagens de diferentes regiões do septo nasal. Assim, uma lei constitutiva que agrega conceitos de híper-elasticidade, viscoelasticidade e permeabilidade, acoplando o distinto comportamento de materiais sólidos e fluidos, foi desenvolvida e validada.

Além das simulações do comportamento viscoelástico das amostras colhidas a partir da região anterior do septo, um conjunto de outras ferramentas para aplicação dos mesmos conceitos numa geometria mais complexa foi também desenvolvido e apresentado. Um trabalho que ainda continua.

Palavras-chave: rinoplastia, cartilagens nasais, análise mecânica dinâmica/térmica, viscoelasticidade, fluência e relaxação, Método dos Elementos Finitos.

ABSTRACT

The facial plastic surgery, and particularly the area of rhinoplasty, is undoubtedly a growing up market. Surgical techniques have been evolving to respond to very specific patient desires not only for functional reasons, but also to resolve aesthetic issues. Actually, it is moving plenty of money around the world, being a great scientific and commercial opportunity among researchers.

The human nose is composed of three major portions separated by two well-defined regions of transition (K-area and S-area) that are very complicated to deal with in postoperative periods. The viscoelastic behaviour of soft biological tissues, especially that of nasal cartilages and adjacent subcutaneous/fatty tissues, is barely known. There are no studies on the viscoelastic characterization of the mechanical properties of nasal septum (NS), upper lateral cartilages (ULC), and lower lateral cartilages (LLC) in creep and relaxation (basic viscoelasticity features) neither on the determination of frequency- and temperature-dependent properties of these tissues through dynamic mechanical analysis (DMA) in tension and compression. General information on thermal degradations through differential scanning calorimetry (DSC) and thermogravimetric analysis (TGA) is also missing. Therefore, part of this work intends to fill this lack of the literature giving some insights into the cartilage internal composition and architecture, as well as the specificity of the activated mechanisms under constant stress or strain. Furthermore, numerical simulations were performed based on a hyper-viscoelastic mathematical formulation using a home-made open-source finite element (FE) solver (V-Biomech) in order to find a set of basic constitutive parameters that allow to replicate the experimental creep and relaxation behaviours of nasoseptal cartilage specimens from distinct regions of the quadrilateral cartilage (QLC). Thus, a complete standard biphasic poro-hyper-viscoelastic constitutive law was developed and validated.

Finite Element Models (FEM) are gaining relevance to analyse soft biological components. As example, numerical simulations of the viscoelastic behaviours of the specimens harvested from anterior part of the QLC were performed to understand which of the constitutive parameters were more sensitive to achieve the best numerical-experimental agreement. The tools to reproduce these simulations in a more complex geometry (the whole nasal structure, with bony and cartilaginous components) were also developed and presented. The work still goes on it.

Keywords: rhinoplasty, nasal cartilages, dynamic/thermal mechanical analysis, viscoelasticity, creep and relaxation, Finite Element Method.

LIST OF CONTENTS

LIST OF FIGURES

LIST OF TABLES

LIST OF ACRONYMS AND NOMENCLATURE

ACRONYM	DESCRIPTION
CoV	Coefficient of Variance
CT	Computational Tomography
DAL	Dorsal Aesthetic Lines
DEM	Discrete Element Models
DKA	Dorsal Keystone Area
DMA	Dynamic Mechanical Analysis
DSC	Differential Scanning Calorimetry
DTA	Differential Thermal Analysis
DTG	(first) Derivative of the Thermogravimetric (analysis)
ECM	Extracellular Matrix
FE	Finite Element
FEA	Finite Element Analysis
FEM	Finite Element Models
GAGs	Glycosaminoglycans
HFS	Head First Supine
LKA	Lateral Keystone Area
LLC	Lower Lateral Cartilages
MRI	Magnetic Resonance Imaging
NS	Nasoseptal Cartilages/Nasal Septum
PAC	Porcine Auricular Cartilages
PBS	Phosphate-buffered Saline (solution)
PGs	Proteoglycans
QLC	Quadrilateral Cartilage
QLV	Quasi-Linear Viscoelasticity (theory)
ROI	Regions of Interest

SEDF	Strain Energy Density Function
SMAS	Superficial Muscular Aponeurotic System
SRT	Spare Roof Technique
$\mathbf{T_g}$	Glass Transition Temperature
TGA	Thermogravimetric Analysis
$\mathbf{T_m}$	Melting Temperature
ULC	Upper Lateral Cartilages
UTS	Ultimate Tensile Stress
WL	Weight Loss

NOMENCLATURE

SYMBOL   **DESCRIPTION**

δ	Phase angle
E'	Storage modulus
E''	Loss modulus
$E*$	Dynamic/Complex modulus
η''	Stored energy
η'	Energy loss
t_{rise}	Rise time of the force
fr	Frequency of the sine wave
Ω_0	Reference configuration of an arbitrary body of interest
Ω	Current configuration of an arbitrary body of interest
$\mathbf{X}$	Position vector of a material point in the reference configuration
$\mathbf{x}$	Position vector of a material point in the current configuration
$\mathbf{C}$	Right Cauchy-Green strain tensor
$\mathbf{F}$	Deformation gradient tensor
$\mathbf{I}$	Second-order unit/identity tensor
$\mathbf{u}$	Displacement field

J	Jacobian of the deformation gradient tensor (local volume ratio)
$\overline{\mathbf{C}}$	Modified right Cauchy-Green strain tensor
$\overline{\mathbf{F}}$	Isochoric deformation gradient tensor
$W(\mathbf{C})$	Strain energy density function
$\mathbf{\Pi}$	Second Piola-Kirchhoff stress tensor
$\mathbf{\Pi}^s$	Solid component of the second Piola-Kirchhoff stress tensor
$\mathbf{\Pi}^f$	Fluid component of the second Piola-Kirchhoff stress tensor
I_1, I_2, I_3	Isotropy-related invariants of the right Cauchy-Green strain tensor
$\mathbf{a}_1, \mathbf{a}_2$	Unit vectors of fibre directions
$I_4, ..., I_9$	Anisotropy-related invariants of the right Cauchy-Green strain tensor
λ_i^2	Squares of fibres stretches in the referential directions
$\overline{W}_H(J)$	Volumetric component of the strain energy density function
$\overline{W}(\mathbf{C}, \mathbf{a}_1, \mathbf{a}_2)$	Isochoric component of the strain energy density function
$\overline{I}_1, ..., \overline{I}_9$	Isochoric contribution of the invariants $I_1, ..., I_9$
$\overline{W}_{iso}(\overline{\mathbf{C}})$	Isotropic part of the total isochoric strain energy function
$\overline{W}_{aniso}(\overline{\mathbf{C}}, \mathbf{a}_1, \mathbf{a}_2)$	Anisotropic part of the total isochoric strain energy function
C_{10}^{MR}, C_{01}^{MR}	Material parameters of the Mooney-Rivlin model
k_1, k_2	Material parameters of the Holzapfel model
$U(J)$	Volumetric energy function
k	Penalty parameter playing the role of a bulk modulus
$\overline{p}$	Hydrostatic pressure of the Cauchy stress tensor
s	Solid (used as an index)
f	Fluid (used as an index)
n_α	Solid/Fluid volume fractions
$\boldsymbol{\sigma}^{total}$	Total Cauchy stress tensor
$\boldsymbol{\sigma}^s$	Effective solid Cauchy stress tensor
$\boldsymbol{\sigma}^f$	Fluid part of the total Cauchy stress tensor
∇p^f	Fluid (or pore) pressure gradient
μ^f	Water chemical potential

$\Delta\pi$	Osmotic pressure gradient
$\mathbf{w}$	Flux of the fluid through the porous solid matrix
$\mathbf{K}$	Hydraulic permeability tensor
$k(J)$	Deformation-dependent permeability
k_0	Initial permeability
M	Positive material constant of the deformation-dependent Darcy's law
$\varepsilon(t)$	Strain function
$J(t)$	Creep function/Compliance of the Kelvin-Voigt model
K_0	Instantaneous elastic response/rigidity
K_i	Purely elastic spring
τ_i	Damper characteristic time
$\sigma(t)$	Stress function
$R(t)$	Relaxation function of the Maxwell model
t	Time
$\mathbf{\Pi}^e$	Elastic stress tensor of the second Piola-Kirchhoff stress tensor
$\mathbf{H}_k$	Internal variable to calculate the total second Piola-Kirchhoff stress tensor
E	Young's modulus
σ^{ut}	Ultimate tensile stress
ε^{ut}	Failure strain
D	Heat flow
T	Temperature
ΔH	Enthalpy

MOTIVATION, AIM AND OVERVIEW

MOTIVATION

Rhinoplasty alone or combined with other surgical procedures, e.g., septoplasty or osteotomy, is a very known technique in the field of facial plastic surgery (Kovacevic et al., 2016), representing the third more performed cosmetic procedure in the United States of America for nose reshaping cases, after breast augmentation and liposuction. These data are refereed according to Plastic Surgery Statics Report of 2015 by the American Society of Plastic Surgeons® (ASPS), which is a leading authority and information source on subjects related to cosmetic and reconstructive plastic surgery.

The prediction of the geometrical configuration of the structures that are involved in the human middle third nose, mainly cartilages and soft tissues in patients submitted to rhinoplasties, is a major concern among the otolaryngologist's community. Clinical interventions in this region may be generally justified by functional reasons (e.g., nasal obstruction), reconstruction after trauma, and correction of the aesthetic lines (Kutubidze, 2015). The main objectives are the re-establishment of normal respiratory functions and the required well-defined anatomical aesthetic lines (Lekakis et al., 2016a).

There are several surgical techniques that can be basically differentiated by the cutting strategy, area of intervention, and cartilage management, particularly in the middle vault. Although this might contribute for a large spectrum of solutions to respond to each patient's desire, excessive lateral tension can be produced in nasoseptal (NS) and upper lateral cartilages (ULC) during fixation sutures (Kovacevic et al., 2015). For that reason, surgical techniques have been evolving to improve the operational methods preserving cartilage's integrity as much as possible.

Due to lack of experimental data on viscoelastic behaviour of soft tissues and cartilages, it is not possible to precisely quantify the lateral stresses installed in these anatomical regions, either to predict its response to specific actions as the ones that are provided in a surgical procedure or postoperative periods. The study of these parameters through numerical simulations could be very relevant for a successful primary rhinoplasty, considering all the contingencies in the preoperative plan.

AIM OF THE THESIS

The present work is oriented toward the development of a computational framework to study the features of the nasal cartilages, in particular the septum, the upper lateral cartilages (ULC), and the lower lateral cartilages (LLC).

The methodology adopted here starts with a review of the literature to understand the anatomy and physiology of the complex human nose, as well as the most frequent issues that usually come following a rhinoplastic intervention. Additionally, a state-of-the-art concerning the numerical modelling of general soft tissues (especially the articular cartilage and meniscus) is presented to establish the development of an own developed numerical model.

It is the authors of the Thesis believe that the present study will produce valuable information on the viscoelastic behaviour of cartilaginous tissues harvested from both porcine samples (used to test and validate the experimental procedures) and human cadaveric samples to provide viscoelastic parameters data to employ in the simulations.

Therefore, four major objectives may be defined in this work:

1. Determination of general thermal features of the human nasal cartilages, such as melting temperatures, glass transitions, and weight loss, using Differential Scanning Calorimetry (DSC) and Thermogravimetric Analysis (TGA);

2. Frequency-dependent viscoelastic characterization of the nasoseptal cartilages (NS) in tension and compression, using Dynamic Mechanical Analysis (DMA), from a standard walking pace (1 Hz) up to traumatic heel-strike frequencies (20 Hz). The evaluation of creep and stress-relaxation time-dependent responses (instantaneous response and damper characteristic times) will be accomplished using the same equipment;

3. Identification of mechanical properties and load intensities of the nasal cartilages to establish an accurate numerical framework. This will allow the representation of the respective rheological behaviour through a structured hyper-viscoelasticity mathematical formulation;

4. Cartilaginous septum creep and relaxation numerical simulations using an own Finite Element (FE) solver (simulation of both creep tests of about 1500 s and relaxation tests for an elapsed time of 400 s) will be accomplished to fit the experimental results. In addition, the evaluation of stress and displacement fields will be performed through Finite Element Analysis (FEA). The development of an accurate 3D FE model of the human nasal structure from Computational Tomography (CT) image segmentation and mesh building have also been successively accomplished. In a near future, this model will permit evaluating the mechanical behaviour of those structures along time.

OVERVIEW

The present MSc Thesis is globally structured in five Chapters: Introduction, Materials and Methods, Results and Discussion, Concluding Remarks, and References. These Chapters are briefly described below.

Chapter 1 (Introduction) aims at giving the reader the essential information of the anatomy and physiology of the human nose, the most common pathologies in the middle-third vault, which is the most challenging region to deal with, and the respective surgical solutions. Moreover, a state-of-the-art on the FEA of general cartilaginous tissues is presented, since its beginning in 1743 until our days. Finally, some insights into the viscoelasticity concepts are given, as well as the general Kelvin-Voigt and Maxwell discrete element models (DEM).

Chapter 2 (Materials and Methods) describes the methodology adopted to undergo the estimation of thermal features and viscoelastic time-dependent parameters, focusing both the adopted experimental details and the equipment that has been employed to accomplish such aim. This chapter also includes the mathematical formulation and generation of the FE mesh to be applied to a home-developed FE solver, whose functioning and modelling features are also addressed.

Chapter 3 (Results and Discussion) includes experimental and numerical results obtained on samples harvested from the auricular region of an animal model (porcine), as well as tissues obtained from the nasal region of human donors (septum, ULC, and LLC). Results from DSC, TGA, and DMA are described and compared with benchmark literature. This Chapter also presents the outcomes of the FE study in a simplified mesh that results from the geometrical configuration of each specimen, either in creep or stress-relaxation loading actions. Numerical-experimental agreements are presented and detailed. The intrinsic constitutive numerical parameters of NS in creep and stress-relaxation are exhibited, as well as the stress and displacement fields in the straight region of the used specimen.

Chapter 4 (Concluding Remarks) conceals the wide-ranging description of the essential outcomes of the present work, being accomplished with a small critical review. Additionally, further investigations are pointed out to improve what has been done so far that will lead to increase the complexity of the FE model.

Chapter 5 (References) contains the bibliographic references that have been consulted to prepare this MSc Thesis.

CHAPTER 1

Introduction

The present chapter is a comprehensive description of the human nose covering the grounds of anatomy, physiology, and functionality based on a literature review. The presentation of the most common pathologies affecting the human nasal structures is made, especially in the middle-third vault, where the cartilage and its soft adjacent tissues play a major role. In addition, a description of the current and adapted surgical techniques is presented. Finally, a state-of-the-art on the cartilage FEM are revised and detailed focusing the most relevant publications in the domain, with some positive outcomes for the improvement of clinical applications.

1. INTRODUCTION

The preoperative consultation in rhinoplasty involves a multitude of actions that are mandatory for the decision-making process (Lekakis et al., 2016a). The surgeon takes a thorough history assessing functional and/or aesthetic aspects, asks for patient's wishes, conducts a nasal photographic analysis, and communicates the goals and pitfalls of the surgery. Computer imaging (or morphing) of the preoperative pictures has drawn a lot of interest in the last decade, which is a sign of the evolution on the preoperative consultation that is occurring. Technological advances in the context of rhinoplasties have led to the development of three-dimensional (3D) imaging techniques that aids the surgeon to demonstrate the expected outcome (Lekakis et al., 2016a; Lekakis et al., 2016b). Presently, computer imaging is processing from 2D to 3D models (Lekakis et al., 2016a). Besides the advantages, some drawbacks must be addressed with care. The cost of the equipment is not a negligible aspect as well as the good-quality imaging software that can reach thousands of dollars (Lee, 2004). There is also a learning curve in developing realistic morphed images just as there is in producing the desired aesthetic changes. As computer imaging has been made technically easier, the hidden danger is to reproduce the simulated results into postoperative outcomes (Adelson et al., 2008; Koch et al., 1998). Further investigations on this topic may change drastically the future of rhinoplasty surgeries.

1.1 Contextualization

Considering the statistics of 2015 of the International Society of the Aesthetic Plastic Surgery (ISAPS), South Korea is the ranking leader in performing rhinoplastic surgeries, with approximately 9.9% of the procedures at the world-wide scale, followed by Brazil with 8.9%. According to the American Society of Plastic Surgeons (ASPS), nose reshaping rhinoplasties occur predominantly in teens and adult women. Statistically, 70% of these cases are in the range of 13 to 39 years and, from those, 76% are women. It has increased 1% from 2014 to 2015 in this gender, whereas a decrease of 3% was verified in male during the same period. However, nose reshaping remains the first reason for men to be submitted to this kind of surgery.

In Portugal, according to the Portuguese Radio and Television (RTP) station and doctor José Carlos Neves in interview, who is a specialist in facial surgery, until 2015 the most common reasons for a rhinoplasty were functional (nasal septal deviation and trauma) and aesthetic (size of the nose, dorsal hump, wide and rounded tip, and fallen tip). Septo-rhinoplasties were then the most executed.

Nowadays, these are not very painful but the edema remains for the first 5-7 days. It is necessary a recovery period of 10-15 days for complete healing. A rhinoplasty can cost between 3500 and 5000 € depending on the time to complete the surgical plan and the spending resources.

1.2 Anatomy and Physiology of the Human Nose

A comprehensive knowledge of the nasal anatomy and physiology is a crucial point to preserve or achieve normal airflow while providing an aesthetically pleasing and natural, permanent long-term result (Kovacevic et al., 2016; Palhazi et al., 2015; Rohrich et al., 2004). This includes a full understanding of the three-dimensional structures of the nose, intranasal and external nasal anatomy as well as the properties and predictable behaviour of different tissue types (Kovacevic et al., 2016; Kutubidze, 2015; Stevens and Emam, 2012).

AN OVERVIEW

The human nose is a very complex structure that can be subdivided into three distinct portions, according to their functional and cosmetic aspects. Its specific functions are the humidification, filtration, and temperature regulation of the inspired air, as well as the sense of smell, which are effectively controlled by nasal cavities, nasal turbinates, internal and external valves, and mucus layers (Kutubidze, 2015; Stevens and Emam, 2012). The bony-cartilaginous pyramid of the external nose is composed by the upper rigid bony third, the middle semi-rigid cartilaginous third, and the lower flexible cartilaginous third, with some well-defined regions of transition (Figure 1a) (Kutubidze, 2015). Figure 1b shows a tripod-like structure, which is similar to a perfect pyramid (Anderson, 1971). The conjoined medial crura make one leg of the tripod and each of the two lateral crura comprises the others. The main purpose of this analogy is to easily characterize some techniques that modify tip rotations, tip projections, and nasal length (Sajjadian and Guyuron, 2010).

(a)   (b)
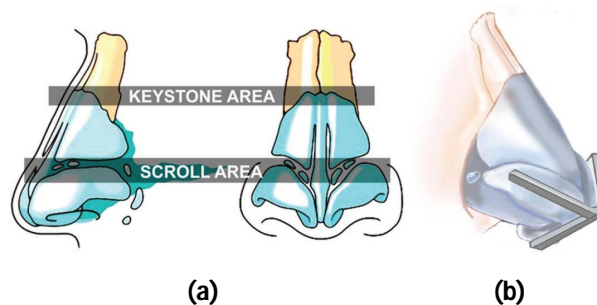
Figure 1: (a) Schematic representation of the keystone area and the scroll area (Kutubidze, 2015); **(b)** Tripod-like structure of the tip composed of columella and the paired lower lateral cartilages (Sajjadian and Guyuron, 2010).

The keystone area (i.e., K-area) is one of the most important regions in the middle third that is involved in the structural stability of the whole nasal dorsum, which connects the radix to the lateral projections of the crura. In that confluent area, there are four solid structural elements that interact with each other – nasal bones, bony septum, cartilaginous septum, and the upper lateral cartilages (ULC) –, all firmly connected by muco-periosteum, muco-perichondrium, and dense fibrous tissues. Cartilaginous septum and ULC have the same embryologic origin so they can be considered as a unique structural component called quadrilateral cartilage (QLC) (Kim et al., 2008).

In the K-area (Figure 1a), nasal bones variably overlap the ULC dorsally (known as dorsal keystone area, DKA), along 7-10 mm (Stevens and Emam, 2012), and laterally (lateral keystone area, LKA). It is the widest portion of the nasal dorsum (Kovacevic et al., 2016; Rohrich et al., 2004). Palhazi et al. (2015) have estimated an average length of the DKA measured along dorsal septum of 8.9 mm (range, 4-14 mm) and an average width of 4.9 mm (range, 3-9 mm), which was determined in fifteen Caucasians cadavers' dissections without signs of nasal trauma or previous rhinoplasty. The LKA was recognized in 80% of the cases as highly variable. *En bloc* elevation of the nasal bones enabled a distinguishable visualization of the K-area, allowing to identify three patterns of transitions between DKA and LKA: continuous (I), stepped (II and III) or minimal (IV) – Figure 2 (Palhazi et al., 2015).
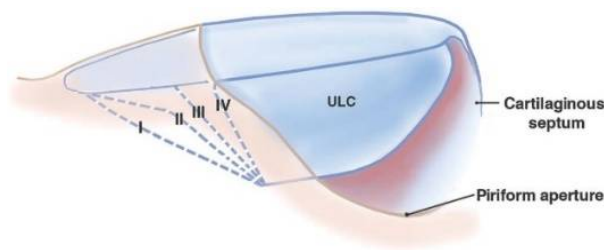
Figure 2: Illustration of the transitions from DKA to LKA: I, continuous; II, rounded stepped; III, sharp-edged stepped; IV, minimal joint (Palhazi et al., 2015).

Figure 3 shows a transition between DKA and LKA in a real human nose after *en bloc* dissection (Figure 3a) against an ideal transition (Figure 3b) drawn by Palhazi et al. (2015).

(a)

(b)
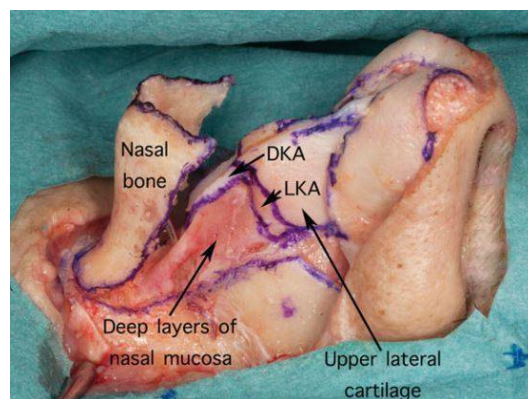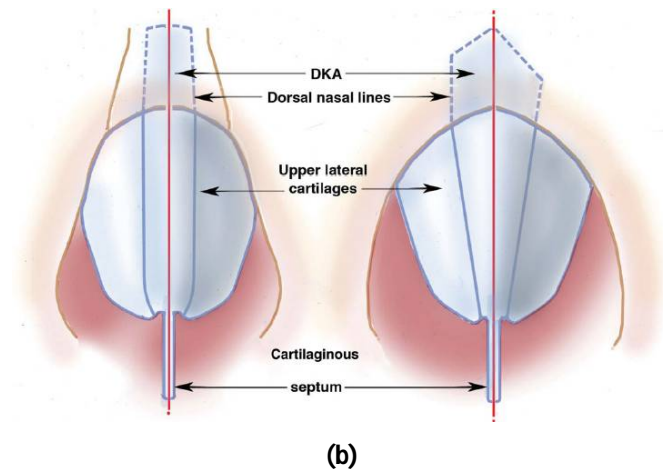
Figure 3: (a) Oblique view of the osseocartilaginous vault with the nasal bones raised during dissection. Identification of the transitions between DKA and LKA; **(b)** Illustration of the cartilaginous relationship between dorsal lines and DKA in a relatively narrow and wide dorsum (adapted from Palhazi et al., 2015).

A set of different overlap patterns between nasal bones and the cephalic borders of the ULC was identified by Kim et al. (2008), presenting four classifications for the caudal shape of the nasal bones and three classifications for the overlap area between the ULC and nasal bones.

In the scroll area (S-area) (Figure 1a), the caudal margin of the ULC are overlapped by the cephalic margin of the lower lateral cartilages (LLC), along 4-6 mm (Kovacevic et al., 2016; Palhazi et al., 2015; Rohrich et al., 2004). Hafezi et al. (2010) described the LLC as three-dimensional hemispheric forms attached to the ULC by dense fibrous tissue that play the role of an internal support mechanism of the nasal tip (Stevens and Emam, 2012; Han et al., 2004).

The middle third is the transition segment linking the rigid bony pyramid to the tip projection. The QLC widens dorsally and creates the so-called T-shaped cross-section (Figure 4) of the middle nasal vault (Ferreira et al., 2016; Kovacevic et al., 2016, Palhazi et al., 2015).
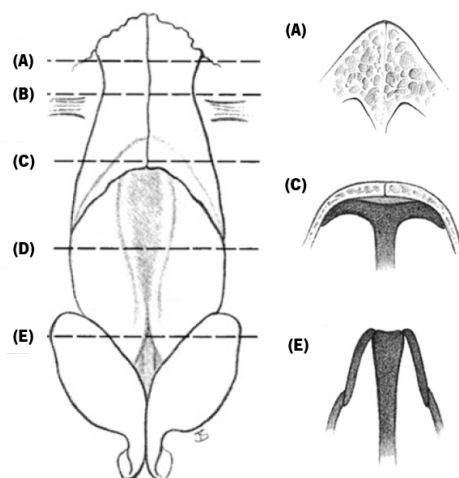
Figure 4: Cross-sectional views of the nasal skeleton. Image (C) represents the overlap of the nasal bones over the ULC cephalic edge and the T-configuration of the nasal septum with the paired ULC (adapted from Oneal et al., 2010).

The nose also comprises a set of soft tissues neighbouring the bony-cartilaginous pyramid including skin, muscles, nerves, and vascular tissues (Kutubidze, 2015; Stevens and Emam, 2012). The skin envelope in the inferior part of the external nose is composed by fibrovascular membranous layers that are divided into epidermis, dermis, superficial fascia, fibromuscular layer, periosteum and perichondrium. The thin and dynamic musculoaponeurotic layer is a crucial structure for retaining nasal function and appearance, and that is why special care must be taken to preserve this layer during surgical procedures (Kutubidze, 2015; Letourneau et al., 1988).

The dorsal aesthetic lines (DAL) are presented in Figure 5, defining the appearance of the dorsum on frontal view. These lines are extensions from the supraorbital ridges and consist in two diverging concave lines, usually beginning its divergence at the K-area until reaching the tip-defining points, being composed approximately by an equilateral quadrangle (Kutubidze, 2015).
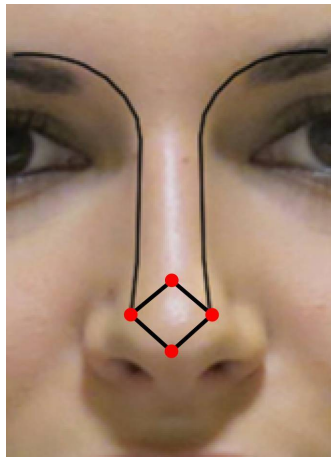
Figure 5: Illustration of the DAL from supraorbital ridges to tip-defining points (adapted from Kutubidze, 2015).

On the frontal view of any given patient, DAL can have different configurations that some authors refer as particular details of each one's shape (Stevens and Emam, 2012). DAL may be asymmetric, excessively wide, excessively narrow or poorly defined. Ideally, the width of the DAL should be the width of tip-defining points (Rohrich et al., 2004). On the lateral view, some attention must be given to the nasofrontal angle formed in the nasion (N) (Figure 6), which is the intersection between the line drawn parallel to the infrabrow glabella (G) and the line drawn as a superior extension of the nasal dorsum (D). The normal angle varies with gender and ethnicity, for example, but it is usually larger in women (around 134º) than in men (around 130º). This angle is very important for the perceived length and projection of the entire nose. For instance, if the nasofrontal angle is positioned more anteriorly and superiorly, the nose will appear more elongated and the tip reduced. On the other hand, if the nasofrontal angle is positioned more posteriorly and inferiorly, the nose will appear shorter and the tip longer. Finally, still from the lateral view, the entire dorsum must be equal to a soft line drawn from the

radix to tip-defining points of both genders, which means that little humps are already considered as small deformities (Rohrich et al., 2004).
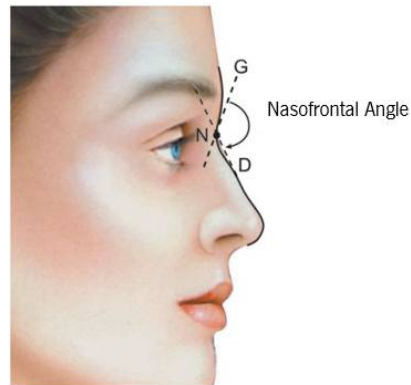
Figure 6: Schematic representation of the correct position of the nasofrontal angle (adapted from Rohrich et al., 2004).

There are other three aesthetically important angles: the anterior, intermediate, and posterior septal angles (Figure 7) (Oneal et al., 2010).
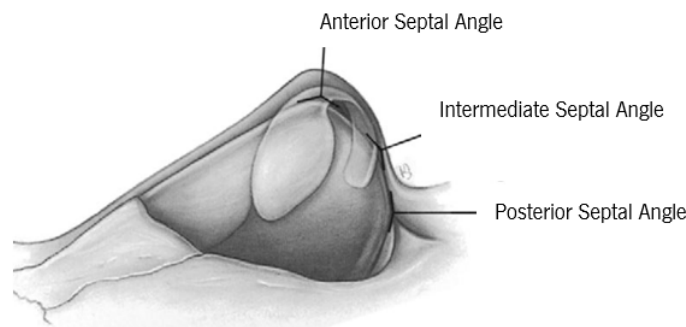
Figure 7: The three most important angles of the caudal nasal septum (adapted from Oneal et al., 2010).

The middle third is a naturally weak region and once it loses its own support any deformity can immediately occur (Ferreira et al., 2016; Kutubidze, 2015; Palhazi et al., 2015). The overlapped portion of the QLC in the K-area is covered by muco-periosteum and muco-perichondrium, both extended to the entire nasal cavity. Therefore, it is difficult to detach ULC from nasal bones with a cephalo-caudal force. However, the connection QLC-nasal bones is relatively weak to dorso-ventral forces that turns it vulnerable to trauma. Sometimes those forces can be applied during rhinoplasty surgeries (humpectomies or osteotomies), which makes this area easily damaged if the surgeons do not manage it carefully (Kim et al., 2008).

EXTERNAL NOSE

The frontal, lateral, and basal views (Figure 8) are all required to adequately assess nasal structures and its normal topographic features (Stevens and Emam, 2012; Oneal et al., 2010).
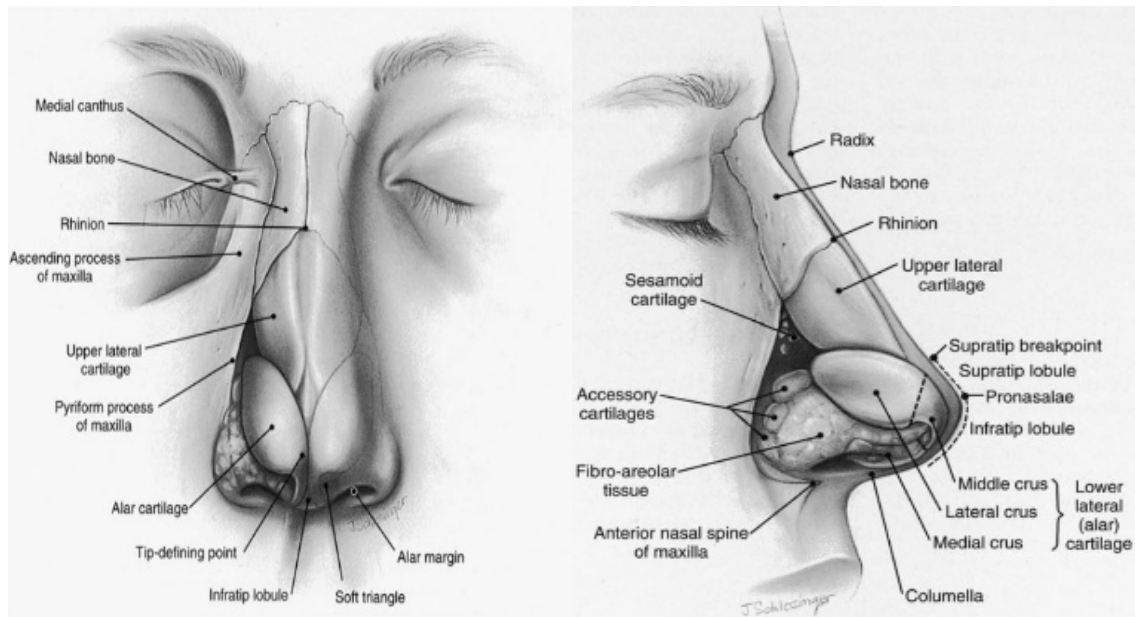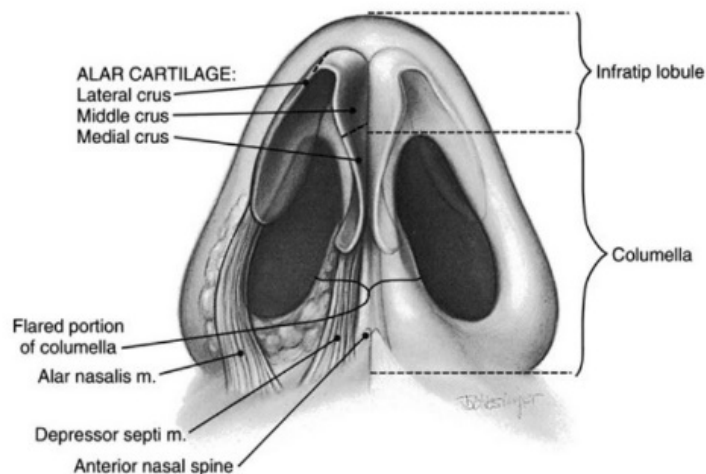
Figure 8: (a) Frontal view; **(b)** Right lateral view; **(c)** Basal view of the human nose (Oneal et al., 2010).

As it is perceptible, the paired nasal bones are the most important components of the upper third. Their length varies greatly both inter- and intra-gender, attaining around 25 mm, and becoming thinner as they extend caudally toward the rhinion. The nasal bones are attached to the frontal bone superiorly, which defines the radix (or root) of the nose. Ideally, the width of the bony vault base should not be higher than 80% of the alar base width (Stevens and Emam, 2012; Oneal et al., 2010; Rohrich et al., 2004).

The paired ULC are fused against each other superiorly (as well as with cartilaginous septum, also called quadrangular septal cartilage). Their shape becomes more rectangular as they extend laterally (Ferreira et al., 2016; Stevens and Emam, 2012). The ULC have demonstrated fundamental

roles not only on preserving the dorsum's height and width, and thus, in definition of the DAL, but also on preserving the internal nasal valves patency and normal airways (Ashrafi, 2014).

The lower third or lobule can be further subdivided into tip (pronasalae), supratip, and infratip lobules. These regions may present different configurations due to size, shapes, and angles of the LLC, each one subdivided into medial, middle, and lateral crura (Stevens and Emam, 2012; Oneal et al., 2010; Natvig et al., 1971) (Figure 9a). The crural complexes have their structure defined by their size, shape, relative angular position, and fibrous attachments, which also vary greatly among ethnicities (Stevens and Emam, 2012).
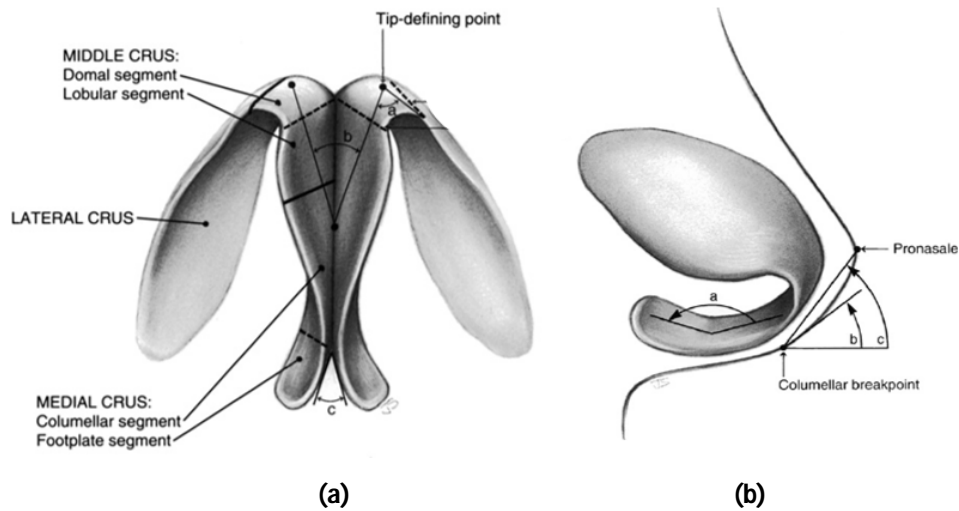
Figure 9: (a) Paired LLC (alar cartilages): a, angle of domal definition; b, angle of domal divergence; c, angle of footplate divergence. **(b)** Right lateral view of angles of rotation: a, angle of cephalic rotation; b, columellar-lobular angle; c, angle of tip rotation (adapted from Oneal et al., 2010).

The lateral crus is the largest and strongest component of the LLC. They play an important role in primary internal support of the lobule and in cosmetic outcomes, especially nasal tip reshaping and nostril asymmetries correction (Stevens and Emam, 2012; Hafezi et al., 2010).

The middle (or intermediate) crus is further subdivided into domal and lobular segments. The domal segment is often the most thin, delicate, and narrow portion of the LLC arches. It is usually short and differently shaped varying a lot its convexity and producing different tip configurations. The lobular segment also varies in shape as well as in length and angles, having great influence on the infratip lobule's form, and it is covered by a thicker soft tissue envelope. Both domal portions of the middle crura are tightly united by the interdomal ligament.

Finally, the medial crus consists on the columellar and footplate segments that are responsible for the entire nose projection. Moreover, the entire nasal base, especially the base of columella, is influenced not only by the shape and angulation of these segments, but also by their integration in the caudal edge of the cartilaginous septum and soft neighbouring tissues (Stevens and Emam, 2012;

Oneal et al., 2010). The most important angles to assess here are the angle of footplate divergence on basal view (Figure 9a) and the angle of cephalic rotation on lateral view (Figure 9b) (Stevens and Emam, 2012).

On lateral view, the tip is the apex of the lobule and, ideally, the most defined element on the profile. The supratip is located cephalically to the pronasalae before the supratip breakpoint; The infratip is located between the tip and nostrils base (Stevens and Emam, 2012; Oneal et al., 2010).

The basal view allows us to assess infratip lobule and columella that are influenced by medial and middle crura configurations. Therefore, asymmetries or prominences are externally easily visible. Some deformities of the septal caudal edge may also be observed from this view as well as the nostril floors and nasal vestibules (Stevens and Emam, 2012).

INTERNAL NOSE

Here, some attention must be given to the nasal cavities, turbinates, and mucous membranes (Stevens and Emam, 2012).
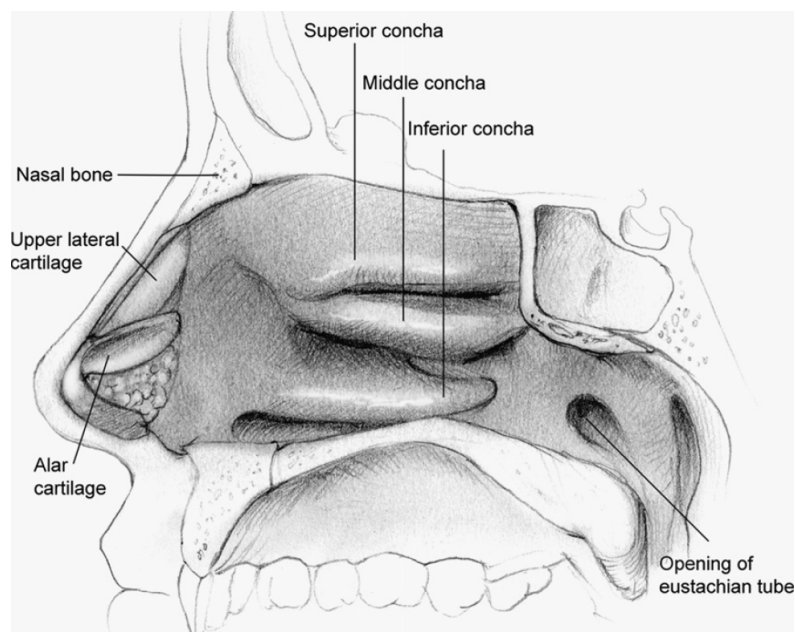
Figure 10: Representation of the internal nose structure (the most important regions are nasal vestibule, nasal cavity and inferior, middle, and superior turbinates (adapted from Stevens and Emam, 2012).

The nasal vestibule (Figure 10) is a small dilated space inside the nostrils that contains numerous thick stiff vibrissae. The nasal cavity is the largest portion of the internal structures, which is strongly neurovascular supplied and lined by mucous epithelium. Above nasal cavity, it is possible to identify three regions of turbinates (the conchae), which are the superior, middle and inferior turbinates.

The olfactory mucosa is a highly specialized membrane that lines the nasal cavity superiorly and contains the olfactory receptors (Oneal et al., 2010).

The nasal cavity is divided by the nasal septum, which is a composite structure made of a cartilaginous part anteriorly and a bony part posteriorly. The cartilaginous part is made of hyaline cartilage with irregular quadrilateral shapes and different sizes. This structure is responsible for the support of the nasal dorsum from the cartilaginous bony junction (rhinion) to the supratip lobule (Stevens and Emam, 2012; Oneal et al., 2010). The bony part is in contact with four bones, which are the vomer, the perpendicular plate of the ethmoid, and the maxillary and palatine bones (Figure 11) (Stevens and Emam, 2012; Oneal et al., 2010).
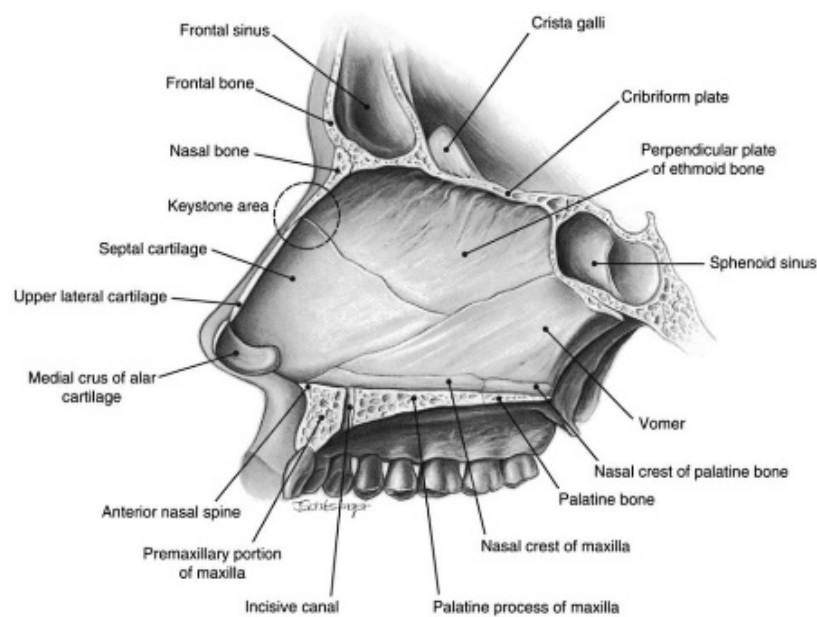
Figure 11: Lateral view of the left side of the nasal septum (Oneal et al., 2010).

As shown in Figure 11, the inferior contact between ethmoid and vomer is dependent on how much septal cartilage is extended in the middle of them. In the K-area, the junction between ethmoid and septal cartilage depends on the amount of nasal bone over the ULC, which means that it can occur up to 10 mm cephalically to the caudal edge of the nasal bone. The bony groove that supports the septal cartilage also varies as observed in the lateral view, being more prominent in premaxilla and becoming more flattened toward the posterior part of the vomer (Oneal et al., 2010).

EXTERNAL NASAL VALVE

The external nasal valve is below the internal nasal valve. It is an area (usually described as the opening) delimited by the lateral alar sidewalls and columella. Weakness of the LLC or scarring can reduce airflow through the external nasal valve causing obstruction (Sajjadian and Guyuron, 2010).

INTERNAL NASAL VALVE

The internal nasal valve is an angle at the junction between ULC, LLC, and septum (Figure 12). This angle commonly varies in a range of 10-15º, being the shape and size of this region mainly governed by each one's ethnicity (Stevens and Emam, 2012; Byrd et al., 2007).

This anatomical region is commonly affected by small changes that severely block the normal airflow. If these modifications affect normal valve's cross-sectional area directly, the airflow resistance will increase drastically, so the nasal cavity function will be compromised (Stevens and Emam, 2012).
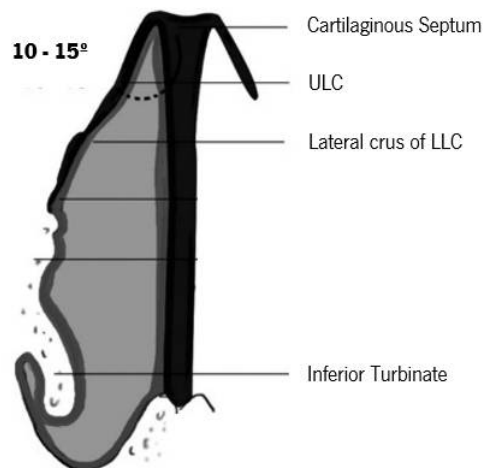
Figure 12: Anatomy of the internal nasal valve (Oneal et al., 2010).

SUBCUTANEOUS TISSUE

Soft tissue thicknesses are also very different along dorsum. Besides muscular fascia, fibro-fatty connective tissue, perichondrium, and periosteum, the skin is one of the most important components to deal with in rhinoplastic preoperative plans (Stevens and Emam, 2012; Oneal et al., 2010). The skin tends to be thinner cephalically and thicker toward the tip and has lots of influence in the external appearance (Oneal et al., 2010; Rohrich et al., 2004). In general, the radix is the thickest point of the nose, combining skin and soft underlying tissues, with 1.25 mm thickness and the rhinion is the thinner point with 0.6 mm thickness (Lessard et al., 1985). The skin is also very thin in columella and along both alar cartilages, especially over domal segments (Sajjadian and Guyuron, 2010).

The underlying bony and cartilaginous tissues decrease in thickness as they pass over the rhinion and become thicker in the supratip region (Oneal et al., 2010; Sajjadian and Guyuron, 2010). The lower half of the nose presents various thicknesses of fibro-fatty connective tissue, which sometimes masks the definition of lobular features (Stevens and Emam, 2012). This area is also susceptible to

oiliness due to the presence of more exocrine glands on dermis, i.e., sebaceous and sweat glands (Stevens and Emam, 2012; Oneal et al., 2010; Letourneau et al., 1988).

The study of soft tissue mobility is also crucial to analyse facial expression dynamics so as to maintain them after any surgical manipulation. Letourneau et al. (1988) discovered that there are five soft components beneath dermis until the underlying cartilage comes up – a superficial fatty layer (adipose tissue), a fibromuscular layer (procerus muscle), a deep fatty layer, and a longitudinal fibrous sheet that combines periosteum, perichondrium, and fibrous tissue in one single layer (Figure 13).
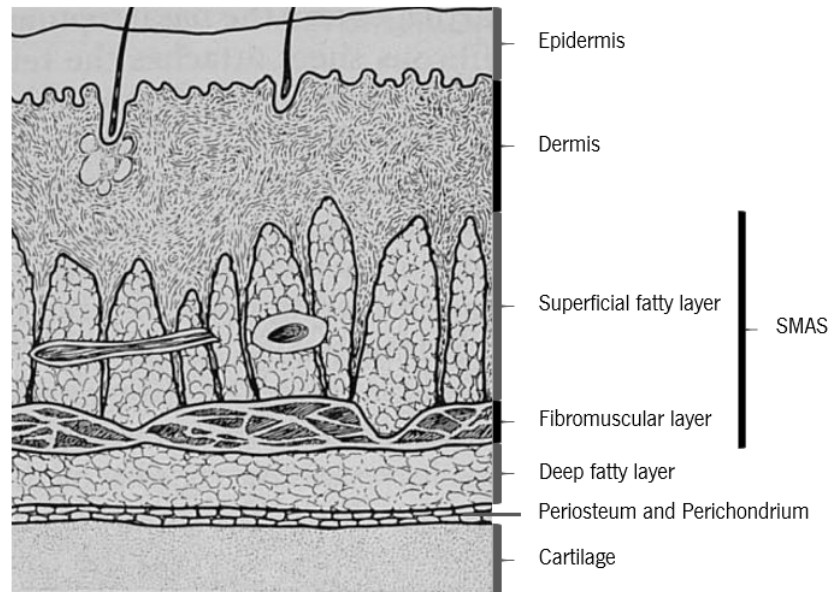
Figure 13: Histology of the soft components described by Letourneau et al. (1988).

The fibromuscular layer, together with superficial fatty layer, is an important component of the nasal Subcutaneous Muscular Aponeurotic System (SMAS) that covers the entire face, interconnecting the facial musculature (Oneal et al., 2010). The deep fatty layer allows the mobility of the overlying muscular aponeurosis (Letourneau et al., 1988).

Beneath deep fatty layer, periosteum and perichondrium are the most important connective tissues. Periosteum covers, among others, the outer face of nasal bones participating in its formation and nutrition. Perichondrium covers the hyaline cartilage of upper lateral, lower lateral and accessory cartilages. This membrane is the nutritive supply of the nasal cartilages (Letourneau et al., 1988).

The skin, epidermis, and dermis are able to move freely along the upper two-thirds of the nose. However, the skin is more firmly attached over the lower one-third and near the tip (Stevens and Emam, 2012). The optimum avascular plane of dissection is below deep fatty layer and above periosteum and perichondrium layer (Oneal et al., 2010).

1.3 Pathologies of the Human Nose

Nasal obstruction is one of the most common chief complains in patients presenting to an otolaryngologist. Mucosal, structural, and sensory problems are the principal causes in the context of functional diseases and aesthetic corrections (Recker and Hamilton, 2016).

Mucosal causes of nasal obstruction will typically lead to fluctuating nasal congestion rather than a fixed obstruction, which means that the problem is not truly structural. There are a variety of mucosal problems, but rhinitis (allergic and non-allergic) and rhinosinusitis are the most popular provoking a dusty and boggy nasal musoca where the inferior turbinate become hypertrophied. This inflammation can result in a potential cause of obstruction, even more if the patient has some degree of septal deviation (Recker and Hamilton, 2016; Becker et al., 2010).

Another important component in the evaluation of nasal obstruction is the sensation of airflow through the nasal cavity. Occasionally, patients might feel that their nasal breathing is inadequate even though their nasal airway is widely patent. This phenomenon of paradoxical nasal obstruction results from patients with empty nose syndrome (Sozansky and Houser, 2015).

There are numerous structural causes of nasal obstruction. Internal nasal valve pinching or external nasal valve narrowing and/or collapse are the most frequent in the middle vault. The obstruction is due to internal angle reduction below 15º. Both inspection and palpation are enough to assess narrowing in this region (DeRosa, 2016; Recker and Hamilton, 2016).

Perhaps the most common cause of nasal obstruction is the septum deviation affecting approximately 80% of the worldwide population. A non-deviated septum appears to be more of the exception than the rule, as it is only present in anywhere from 7.5% to 23% (Becker et al., 2010; Gray, 1978). However, many of these patients may be asymptomatic or not overly bothered by the septal deviation (Recker and Hamilton, 2016). One of the cases is the isolated caudal septal deviation in which it is expected the collapse of the ipsilateral sidewall during inspiration. It can be caused by trauma or as a result of overgrowth of the quadrangular cartilage (DeRosa, 2016). Another case is the quadrangular cartilage deviation. When the caudal septum is centred, but the central region of the quadrangular cartilage is deviated (dorsal septal deviation), the nostril on the contra-lateral side will be prone to collapse. This problem is typically resolved with the septal abnormality correction (DeRosa, 2016; Recker and Hamilton, 2016). In general, anterior septal deviations, often in the nasal valve region, may be more likely to cause the patient significant symptoms of nasal obstruction, whereas posterior deflections typically need to be larger to cause any problem. From those, deviations of the

anterior part of the quadrangular cartilage into mid-to-low nasal cavity are more common (Becker et al., 2010).

Regarding the lower vault, a reference is made to the characteristic abnormalities of the lateral crura that compromise nasal functions and result in poor aesthetics (DeRosa, 2016). When both lateral crus are mal-positioned, either cephalically or sagittally, or simply too weak, they are also predisposed to collapse (Hamilton, 2016). Moreover, it is also important to recognize not only the orientation but also the shape of the lateral crura. Concavities or convexities of the LLC can lead to nasal obstruction as well as an undesirable appearance of the tip. A relatively common situation is the convex lateral crura resulting in supra-alar pinching and internal curvature (Hamilton, 2016; Recker and Hamilton, 2016). Short medial crura can also contribute to nasal obstruction because it may result in a widening of the nasal base and subsequent narrowing of the nostrils (Recker and Hamilton, 2016). Stabilizing nasal base is therefore crucial for a well-functioning nose. Providing nasal tip support is very important to avoid external nasal valve collapse and tip support weakening (DeRosa, 2016).

To conclude this topic, nasal bones abnormalities must be addressed. If the nasal bones are deviated, then they must be repositioned and aligned with the dorsum (osteotomy). Sometimes when bony vault is deviated, the middle and lower thirds are also deviated, which compromises the internal nasal valve and the respiratory function (DeRosa, 2016).

From an aesthetic point of view, the most common reasons for a rhinoplastic intervention are dorsal hump, crooked nose, wide, long or flat nose, aging and/or rounded tip. A dorsal hump does not typically result in a functional issue. However, there are instances in which dorsal hump requires reduction through a humpectomy. Sometimes, a lateral osteotomy alone may be sufficient (Recker and Hamilton, 2016).

1.4 Rhinoplasty: Techniques, Spreader-grafts and Autospreader flaps

In this subsection, a review of various techniques to correct functional obstructions and aesthetic lines is performed. In fact, the relationship between these procedures is tightly linked (DeRosa, 2016).

Endonasal (closed) and external (open) techniques are the two main surgical procedures in both primary and secondary rhinoplasties. Closed rhinoplasty is reserved for isolated deformities in dorsum and nasal tip regions. On the other hand, the open technique employs marginal and transcolumellar incisions, which allows a complete exposure and visualization of the osseocartilaginous skeleton. This clear visualization permits an accurate correction of nasal framework deformities as well as precise

manipulation of the underlying tissues, being the preferred approach either for primary or secondary rhinoplasties (Kutubidze, 2015). However, the open approach has some disadvantages: more time to be successfully complete, external scarring, and prolonged tip edema (Sajjadian and Guyuron, 2010).

Since the beginning of rhinoplastic procedures, the middle third has been probably the most difficult segment to deal with regarding its stability, functionality, and the brow-tip line preservation. Based on the objective to maintain the ULC integrity (and the T-shaped cross-section), two different procedures must be described: destructive/reconstructive techniques, with some degree of destruction of the T-shaped segment, and conservative techniques, where the ULC are completely preserved (Ferreira et al., 2016; Ashrafi, 2014). The destructive/reconstructive techniques consist in splitting the ULC between them and between the septum, i.e., the T-shaped segment is completely separated in three different parts. The conservative techniques allow the preservation of the middle/upper nasal pyramid, because of the upper *en bloc* movement and repositioning. Through the new Spare Roof Technique (SRT) described by Ferreira et al. (2016), the surgeon isolates the entire roof of the middle third, separating the quadrangular cartilage from the ULC without splitting the ULC among them. This procedure is very innovative among the otolaryngologist's community. Actually, the most performed surgical techniques in the field of aesthetic surgery are the septoplasty for correction of the septal deviation, osteotomy for the alignment of the nasal bones, and humpectomy for dorsal hump reduction or removal (Gruber et al., 2011; Gruber and Perkins, 2010). Following hump removal, potential complications may occur due to loss of stability of the middle vault. Functional insufficiency of the internal nasal valve is very likely to occur, together with "inverted V" deformity, disruption of the DAL or dorsum narrowing caused by the ULC collapse after over-resection (Kovacevic and Wurm, 2015; Ashrafi, 2014). Reconstruction of the nasal tip projection might also be needed, which is not always easy because of its mobility (Daniel, 2009; Guyuron et al., 2000). Indeed, the polly beak deformity, characterized by a rounded downward tip and a fullness of the supra-tip region, is very common (Kutubidze, 2015).

Sheen's spreader grafts are the gold standard for restoring structural stability and contours of the middle vault after hump reduction or removal (Sheen, 1984). Traditionally, spreader grafts can be obtained from septal cartilage (Gruber et al., 2011), auricular (conchal) cartilage (Friedman and Coblens, 2016; Quatela et al., 2004), and costal cartilage from ribs (Fedok, 2016). Patients with high, narrow dorsum, weak middle vault, short nasal bones, and thin nasal skin are very susceptible to develop middle vault collapse and further nasal obstruction (Kovacevic et al., 2016; Kovacevic and Wurm, 2015; Byrd et al., 2007). Recently, the use of autospreader flaps have become a reliable

alternative to undergo the treatment of some cases after primary rhinoplasty. Instead of trimming the ULC to match the newly dorsal profile, the excess vertical height is used to create bilateral inwardly folded cartilage flaps that are sutured to the upper aspect of the septum strengthening and stabilizing the weakened middle vault. The application of autospreader flaps (unilaterally or bilaterally) can also be done together with traditional spreader grafts (Kutubidze, 2015; Gruber et al., 2007). This benefit is almost entirely derived by the spring-like effect of the partially folded ULC that mimic the natural anatomic configuration of a well-functioning ULC-septal junction. However, only patients with adequate ULC length and reasonably firm cartilage are suited candidates for spreader flaps employment (Kovacevic and Wurm, 2015; Kutubidze, 2015). It is easier to execute autospreader flaps during open techniques than in closed approaches, where the visualization for scoring and suturing is reduced (Gruber et al., 2007).

The ideal patient for the use of autospreader flaps requires at least 3 mm or more of dorsal hump reduction (types III or IV of cartilaginous hump) to fold the dissected ends of the ULC as local flaps at their interface with the septum. There are several different types of spreader flaps including basic spreader flaps, flaring spreader flaps, support spreader flaps, and interrupted spreader flaps (Ashrafi, 2014; Wurm and Kovacevic, 2013). Figure 14 shows the most common and easier situation that is placing basic spreader flaps with internal anchoring suture.

(a)   (b)
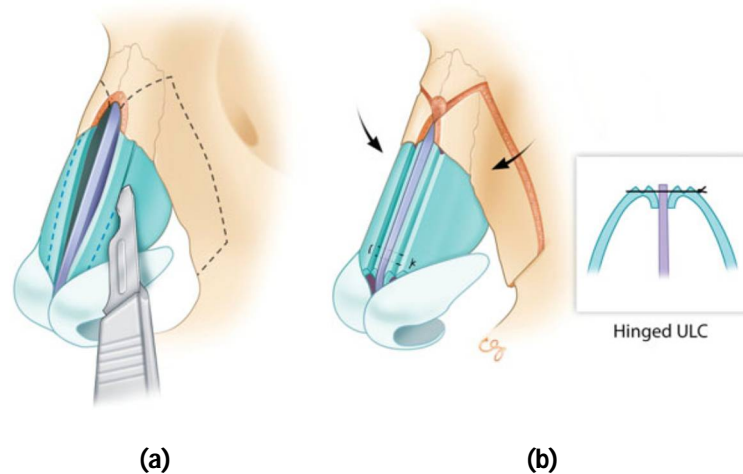
Figure 14: Basic autospreader flaps with internal anchoring suture. **(a)** ULC scoring; **(b)** Osteotomy for the nasal bones repositioning. After ULC in-folding, a single absorbable suture is placed caudally (Moubayed and Most, 2016).

The scoring of the ULC does not need to be performed along the entire length. Some authors have suggested that scoring is not always necessary or should be limited to the caudal end of the flaps (Moubayed and Most, 2016; Wurm and Kovacevic, 2013). Besides, the preservation of the muco-perichondrium as much as possible also helps the autospreader flaps to stabilize (Byrd et al., 2007).

In clinical practice, the correction of the internal nasal valve narrowing, septal deviation or middle vault asymmetries are typically achieved by placing spreader grafts, especially if the spreader flaps cannot provide sufficient nasal dorsum width or cannot be in-folded due to reduced amount of remaining ULC (Ashrafi, 2014). Spreader grafts are long and 1-2 mm wide, rectangular strips of autologous cartilage that are placed on one or both sides of the nasal dorsum (DeRosa, 2016; Kim and Papel, 2016; Becker et al., 2010) (Figure 15).
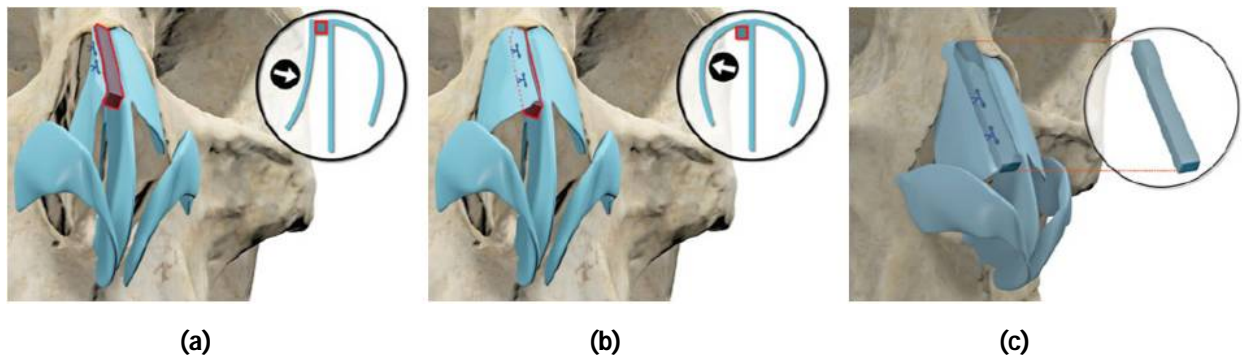
Figure 15: Schematic illustration of middle vault restoration using **(a)** structural spreader grafts, **(b)** straight pedestal spreader grafts, and **(c)** tailored pedestal spreader grafts (adapted from Kovacevic et al., 2016).

Structural spreader grafts are positioned between septal plane and remaining ULC. Pedestal spreader grafts are also positioned in the same relative place, but fixed approximately 0.5 to 1.5 mm below the septal edge depending on the ULC thickness. The edges of the ULC are then placed at the top of the spreader grafts covering them completely and secured with horizontal mattress sutures (Kovacevic et al., 2016). Besides the correction of internal nasal valve obstruction, these solutions also provide the correction of dorsal septal deviation and nasal asymmetries by placing asymmetric spreader grafts with the additional width placed on the contralateral side of the septal deviation (DeRosa, 2016). Alternative solutions are briefly described by Becker et al. (2010).

Spreader grafts are also used in LLC and tip stabilization, which affects the external nasal valve. External nasal valve collapse treatment is trickier because of the nostril mobility and the strength/ weakness of the lateral nasal wall. Even when faced with an obviously narrowed or floppy nostril, one must account for the dynamic actions of the nasalis muscle during inspiration (Recker and Hamilton, 2016).

Alar batten grafts are the most common treatment for external nasal valve collapse (Figure 16). These grafts aim at providing the augmentation and strengthen of the weakened lateral crus after over resection or instead to replace its curvature, since side-to-side contour asymmetries exist between crura in more than 50% of the cases and most of them act to weaken the lateral crus (Quatela et al., 2004). The alar batten graft is usually fashioned from auricular conchal cartilage and secured with absorbable

sutures (Friedman and Coblens, 2016; Becker et al., 2010). Alternative solutions are briefly described by Becker et al. (2010).
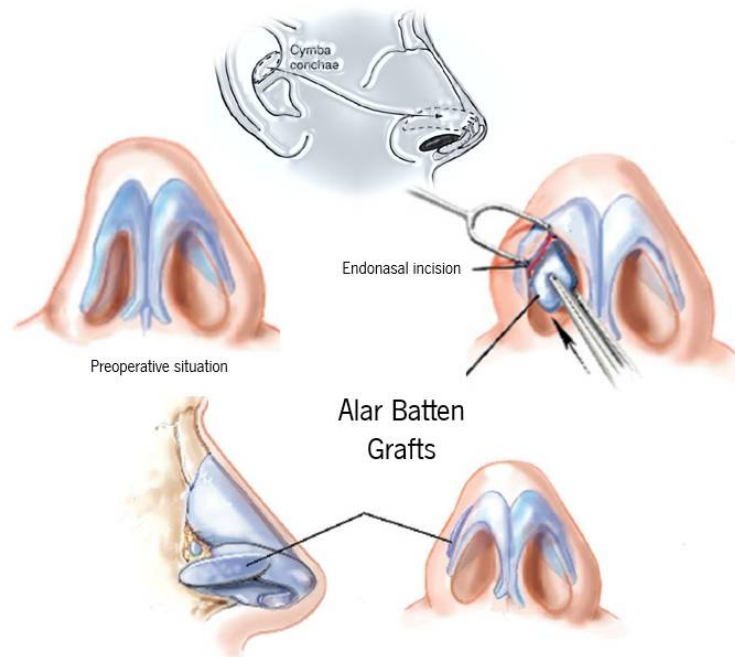
Figure 16: The placement of alar batten grafts for treatment of the external nasal valve collapse (adapted from Becker et al., 2010; Quatela et al., 2004).

Lateral crura corrections are firmly related to nasal tip projection and stabilization, since the curvature of each lateral crus may influence the tip projection (Sands and Adamson, 2015). Thus, spreader grafts are needed for this region too. The caudal strut graft (or columellar strut) is used to strengthen medial crura and maintain (or increase) tip projection, rotation, and support (Figure 17). This is a rectangular autologous cartilage graft with approximately 8-12 mm long, 3-4 mm wide, and 1-2 mm thickness, that is horizontally sutured between medial crura after either open or closed approaches (Ansari et al., 2008). Further information on this topic is described by Ansari et al. (2008) and alternative solutions are briefly described by Daniel (2009).
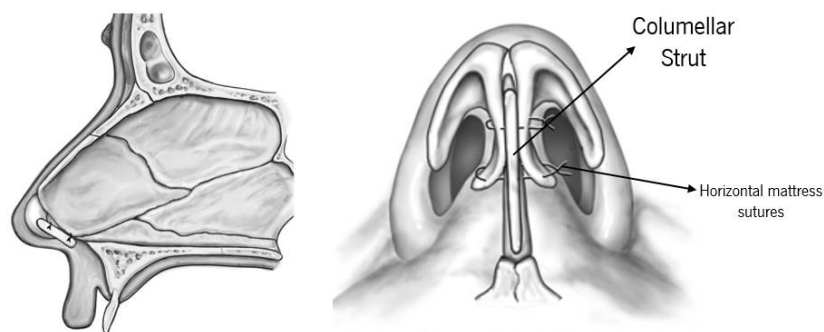
Figure 17: The placement of columellar struts for maintenance of tip projection, rotation, and support (adapted from Ansari et al., 2008).

1.5 Nasal Cartilages: Characterization of the Ground Matrix

Soft tissues are among the most relevant structures of whole biological components with highly important mechanical functions. Tendons and ligaments, articular cartilage, skin, blood vessels, aortic valves and intervertebral discs are widely described in the literature (Zhu et al., 2016; Avanzini et al., 2014; Annaidh et al., 2012; Anssari-Benam et al., 2011b; Marchesseau et al., 2010).

Cartilage is a chondrocyte made, resilient, and viscoelastic tissue that covers and protects the edges of bones at the joints (articular cartilage). It is also found in nose, ears, intervertebral discs, larynx, trachea, thorax, and pubic symphysis (Fung, 1993). It can be subdivided into three main categories: hyaline (from *hyalos*, meaning glass), *yellow* elastic (much more elastin), and *white* fibrocartilage (the only group that contains type I collagen in addition to the common type II) (DiSilvestro and Suh, 2002; Fung, 1993). Due to their heterogeneity, presenting depth-dependent composition and structure, cartilage behaves differently in tension and compression (Poole, 1997; Poole et al., 1987).

Nasal cartilages (septum, ULC, and LLC) belong to the hyaline cartilages group (Nimeskern et al., 2015; Immerman et al., 2011), which are mostly made up of type II collagen. Hyaline cartilages are covered externally by perichondrium that is responsible for their nutrition by diffusion. Immerman et al. (2011) reported the use of costal and auricular cartilage grafts to repair nasal defects after subcutaneous tissue resections or tumour removal with satisfactory aesthetic and functional pleasant long-term results. Because of that, some authors have suggested that they all have the same components throughout the same layers. During years of clinical practice, rhinoplastic surgeons have been suspecting that both hyaline and elastic cartilages have the same histological structure, and thus, nasal cartilages (with emphasis on LLC) reveal shape memory effects due to elastin content, just like what happens in outer ear regions, particularly the external ear flaps (Immerman et al., 2011; Poole, 1997).

NASAL CARTILAGES

Nasal cartilages are aneural, avascular, and almost acellular tissues that are morphologically characterized by a small number of chondrocytes (approximately 4% by wet weight). Chondrocytes are responsible for production, organization, and maintenance of the extracellular matrix (ECM) (Choi et al., 2011; Cohen et al., 1998; Poole, 1997). The main components of the ECM are water, type II collagen (15-30%), and proteoglycans (PGs) (3-10%), composed themselves by proteins and polysaccharides (Nimeskern et al., 2015; Cohen et al., 1998).

Although water is the most abundant component, only a small portion is bound to the matrix. A portion of water is primarily associated to the presence of PGs. The others are considered either freely exchangeable or trapped within the collagen interfibrillar spaces (Choi et al., 2011; Borthakur et al., 2006). The cartilage's affinity for water arises primarily from the presence of PGs, whose negative charges attract free-floating positive ions, such as Na_+, increasing the osmotic pressure (Borthakur et al., 2006; Wilson et al., 2005a). However, nothing is specific about PGs ability to trap or bind water within the tissue's matrix. The reason for not concluding the water as always freely exchangeable is that nobody knows whether it is true in all conformational states (Torzilli, 1985; Jaffe et al., 1974). Besides, interstitial water is also present in intrafibrillar spaces of collagen fibrils and fibres (Figure 18) (Fung, 1993; Katz and Li, 1973).

As a composite (Torzilli, 1985), the balance between water content (hydration), PGs-generated swelling pressure, and the tensile resistance imposed by the collagen network ultimately provides the osmo-viscoelastic mechanical properties of cartilage (Choi et al., 2011).
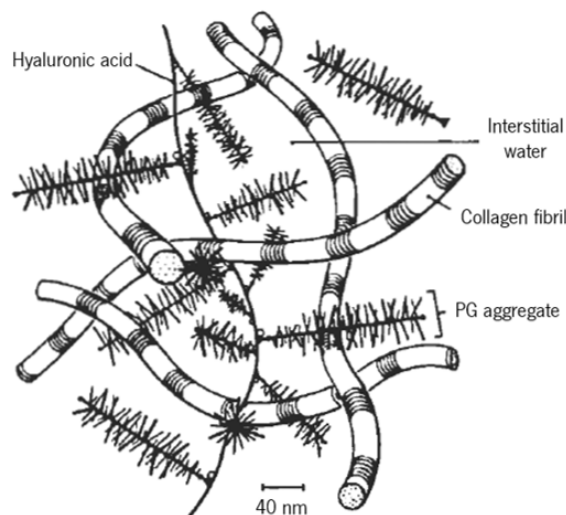
Figure 18: Generic distribution of the ECM components in cartilage. Bundles of fibrils form fibres (adapted from Cohen et al., 1998).

Rotter et al. (2002) found that, in general, the biochemical composition of nasoseptal cartilages is qualitatively similar to that of articular cartilage. However, material properties, such as the average permeability and collagen content, are slightly different (PGs content remains similar). In fact, despite both are classified as hyaline, they have different architectures (no Benninghoff arcades in nasal cartilage) and functions (articular cartilage provides lubrication and load distribution, while nasal cartilage provides mechanical support), which may justify the noticed differences in mechanical properties. On the other hand, LLC are much more biochemically and mechanically comparable to

auricular cartilages, since both contain large amounts of elastin and lower strength, stiffness, and GAGs content (Nimeskern et al., 2015).

COLLAGEN FIBRES ALIGNMENT

Collagen is a triple-helical protein that primarily supports the ECM (Fung, 1993). About 50-60% of the total mass of the proteins in cartilage is from type II collagen, which is organized into a cross-linked fibrillar network (Quinn and Morel, 2007). Its major function is to exert an opposite force against the PGs tendency to expand, since it does not offer large resistance in compression (in result of the high length/diameter ratio) (Borthakur et al., 2006; Cohen et al., 1998).

The orientation of the collagen fibres varies continuously from cartilage's top surface to the base (Xia et al., 2001) and it is very important structurally. In nasoseptal cartilage, at the most superficial zone, collagen is densely packed and distributed horizontally. The remaining zones (in depth) have been shown to have an undefined orientation, tending to rearrange under a specific loading (Xia et al., 2001; Jeffery et al., 1991).

Therefore, one can assume that nasoseptal cartilage collagen fibres have two major fibril directions in loading – the one that follows the respective loading direction and another that remains crimped (Poole, 1997; Clark, 1985). Regarding ULC and LLC, collagen fibres have the direction of their curvature, which can vary a lot according to each one's anatomy (Figure 19).
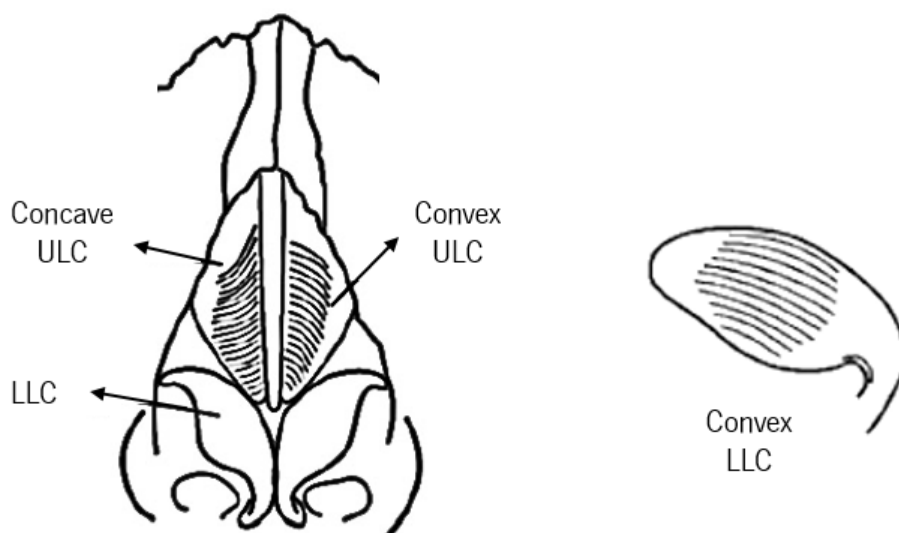
Figure 19: Schematic representation of the concave and convex ULC fibre alignments (left) and the normal convex LLC fibre alignment (right) (adapted from Ansari et al., 2008; Quatela et al., 2004).

OTHER SOLID MATRIX COMPONENTS

The ECM contains a variety of densely packed glycosaminoglycans (GAGs) in approximately 6% by wet weight attached to PGs (Cohen et al., 1998; Maroudas, 1976). Those include chondroitin sulphate, which is the predominant GAG in cartilage, and keratin sulphate (Borthakur et al., 2006). A large number of carboxyl and sulphate molecules of GAGs side chains are ionized in physiological conditions, justifying the characteristic cartilage's negative charge density (Richard et al., 2013; Choi et al., 2011; Borthakur et al., 2006). These negative charges provide a strong electrostatic repulsive force among PGs and attract positive ions and water molecules (Choi et al., 2011). The balance between the osmotic and electrostatic forces are responsible for the free-swelling pressure of cartilage (Borthakur et al., 2006).

Besides, one must take into account that biochemical composition and mechanical properties are age-dependent especially regarding GAGs and collagen contents (Nimeskern et al., 2015; Rotter et al., 2002).

1.6 Material Laws for Soft Tissues

The mechanical response of a soft tissue can be determined both for static and time-dependent conditions. In the first case, its behaviour is reduced to an instantaneous response. In the second, a time-dependent response is obtained in the form of general creep and relaxation curves (Freutel et al., 2014; Choi et al., 2011; Marchesseau et al., 2010).

The mechanical response is highly dependent on the material phases. Thus, material models can be classified into monophasic, biphasic, triphasic, and quadriphasic. Monophasic models are described by viscoelastic constitutive equations that can be used either to represent a global time-dependent response of a biological material independently on the presence of an interstitial fluid, or to simply describe the time-dependent behaviour of a single solid phase on a biphasic model; Biphasic models study a solid phase combined with an interincisal fluid in which exudation during creep and imbibition during swelling/recovery are taken into account; Besides, if the physiological local pore pressures are of interest, a triphasic model must be conducted to address for tissue's osmotic potential; Quadriphasic models are those in which both anions (Cl) and cations (Na+) together with solid and fluid phases are distinctly modelled (Freutel et al., 2014; van Loon et al., 2003).

It is generally accepted that, for a correct description of the mechanical behaviour of cartilage, an anisotropic, visco-poroelastic model should be used (Anssari-Benam et al., 2015; Richard et al., 2013).

Viscoelasticity results from a conformational change of some macromolecules (fluid flow-independent); Poroelasticity results from the migration of other small molecules (fluid flow-dependent) depending on matrix permeability (Richard et al., 2013).

1.6.1 Viscoelasticity

Viscoelastic materials exhibit both properties of elasticity (i.e., the structure is able to return to its original unloaded configuration), which is a spring-like behaviour, and viscosity (i.e., the stress and strain depend on time), which is a dashpot-like behaviour (Freutel et al., 2014; Banks et al., 2011; Lakes, 2009). The viscous part arises from the interactions between both solid and fluid phases, as well as both anions and cations diffusion, from the inherent viscoelasticity of the solid matrix, and from the interstitial fluid flow (Mak, 1986).

When a viscoelastic material (like cartilage) is strained, and the strain is held constant, the corresponding stress decreases with time. This phenomenon is called stress-relaxation or just relaxation (for short). If the same material (again cartilage) is stressed, and the stress is held constant, it continues to deform with time. This phenomenon is called creep (Lakes, 2009; Fung, 1993). The features of creep and relaxation are found in many materials and these are features of viscoelasticity.

When testing a viscoelastic material, it is preferable to apply a step strain or stress rather than a ramp (constant rate), because the effect of time is isolated from any other non-linearity (Fung, 1993).

CREEP-RECOVERY BEHAVIOUR

Figure 20 shows an ideal representation of a creep-recovery curve.
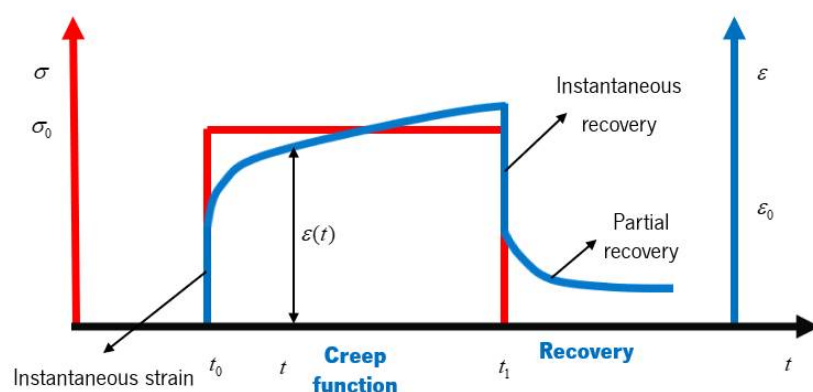
Figure 20: Representation of an ideal creep-recovery curve. Stress σ and strain ε versus time t.

Three different moments can be described here (Figure 20):

- At $t = t_0$, the application of an instantaneous stress σ_0 produces an instantaneous strain ε_0;

- During $t_0 < t < t_1$, the maintenance of a constant stress σ_0 leads to a *strain function* $\varepsilon(t)$ that evolves along time $\varepsilon(t) > \varepsilon_0$;

- At $t = t_1$, the stress σ_0 absence leads to an instantaneous recovery. Depending on stress level and sample hydration condition, the strain recovery $\varepsilon_r(t - t_1)$ can be total or partial. Strain in recovery may or may not approach to zero.

Under constant stress σ_0, the strain $\varepsilon(t)$ is a function of t and σ_0 (Equation 1.1), such that (Lakes, 2009):

$$\varepsilon(t) = J(t) \cdot \sigma_0 \tag{1.1}$$

where $J(t)$ is the *creep function* or *compliance* (Fung, 1993). Moreover, the creep function (Equation 1.2) is defined as (Fung, 1993):

$$J(t - t_0) = \frac{\varepsilon(t - t_0)}{\sigma_0} \tag{1.2}$$

where t_0 is the time of application of an instantaneous stress σ_0.

In general, at the time t, the viscoelastic material response depends on the history of the mechanical loading. If one is dealing with a linear viscoelastic material, based on Boltzmann's superposition principle, it can be said that an increment of the strain $d\varepsilon$, which depends on complete history up to time t, is related to the increment of stress $d\sigma$ at the specific time increment τ to t, through the creep function at the time $t - \tau$, as follows,

$$d\varepsilon(t) = J(t - \tau) \cdot \frac{d\sigma(\tau)}{d\tau} d\tau \tag{1.3}$$

where τ is a time variable of integration, ranging from t_0 to t. The complete strain at the time t (Equation 1.4) is obtained by integration of all strain increments (Boltzmann's superposition integral) (Lakes, 2009; Fung, 1993):

$$\varepsilon(t) = \int_{t_0}^{t} J(t - \tau) \cdot \frac{d\sigma(\tau)}{d\tau} d\tau \qquad (1.4)$$

One can easily understand that the instantaneous deformation ε_0 is given by $\varepsilon_0 = J_0.\sigma_0$, in which J_0 is the *material instantaneous elastic compliance* (Lakes, 2009; Fung, 1993).

STRESS-RELAXATION BEHAVIOUR

Figure 21 shows an ideal representation of a stress-relaxation curve.
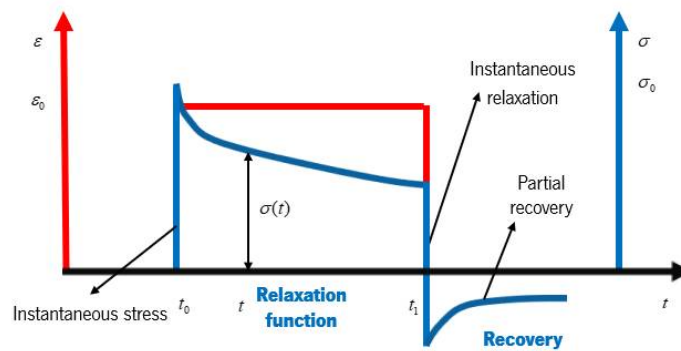
Figure 21: Representation of an ideal stress-relaxation curve. Stress σ and strain ε versus time t.

In stress-relaxation and recovery, the relation between stress and strain can also be described in three steps (Figure 21):

- At $t = t_0$, the application of a constant strain ε_0 produces an instantaneous stress σ_0;

- During $t_0 < t < t_1$, the maintenance of a constant strain ε_0 leads to a *stress function* $\sigma(t)$ that evolves along time $\sigma(t) < \sigma_0$;

- At $t = t_1$, the deformation ε_0 vanishes and an instantaneous relaxation/recovery step starts. The stress-recovery $\sigma_r(t - t_1)$ can be total or partial. If the recovery approaches to zero, then the material's behaviour is purely viscoelastic.

Under constant strain ε_0, and from previous explanation, the stress $\sigma(t)$ (Equation 1.5) is given by (Lakes, 2009):

$$\sigma(t) = R(t) \cdot \varepsilon_0 \qquad (1.5)$$

where $R(t)$ is the *relaxation function* given by Equation 1.6 (Fung, 1993):

$$R(t - t_0) = \frac{\sigma(t - t_0)}{\varepsilon_0}$$

(1.6)

where t_0 is the time of application of an instantons strain ε_0.

Based on Boltzmann's superposition integral, the complete stress at the time t (Equation 1.7) can also be determined by integration of all stress increments (Lakes, 2009; Fung, 1993):

$$\sigma(t) = \int_{t_0}^{t} R(t - \tau) \cdot \frac{d\varepsilon(\tau)}{d\tau} d\tau$$

(1.7)

1.6.2   Rheological Models

Some previous studies have suggested that creep and stress-relaxation might be described through discrete element models (DEM) as an alternative to the most widely used continuous quasi-linear viscoelastic theory (Anssari-Benam et al., 2014).

Rheological models have been traditionally the most popular choice to characterize viscoelasticity of soft biological tissues. Those are mathematical expressions that can be physically represented by configurations of a finite number of springs and dashpots associated in series or in parallel (Anssari-Benam et al., 2015).

Viscoelastic DEM may undoubtedly simplify the analysis (Anssari-Benam et al., 2014). However, they have shown good agreements with experimental data, especially characterizing regimes of creep and stress-relaxation. By altering the number of springs and dashpots or the model configuration, one can find a multiple array of solutions to describe the same behaviour, with corresponding differences on the reported viscoelastic parametric values (Anssari-Benam et al., 2015). Stress-relaxation and creep moduli, characteristic times, and rate effects can be estimated this way.

Previous studies have stablished that two characteristic time scales, referred to as "fast" and "slow" times or "short-" and "long-" term memory effects, are enough to characterize time-dependence behaviour of many tissues (Banks et al., 2011; Fung, 1993). "Fast" implies that a short time is required for the tissue to return to its equilibrium state, while "slow" reflects a long time-scale for that to

happen (Anssari-Benam et al., 2015). Both can coexist if one is dealing with a double branch modelling.

Soft tissues have both short and long characteristic times, presenting a fast-instantaneous response followed by a much slower equilibrium kinematics. In DEM, these two "times" are achieved by placing two dashpots with two springs (Fung, 1993). The most applied rheological models with two characteristic times, i.e., four-element models, are the generalized Kelvin-Voigt's for creep-recovery and the generalized Maxwell's for stress-relaxation behaviours.

KELVIN-VOIGT MODEL

A generalized Kelvin-Voigt model (Figure 22) consists on Kelvin-Voigt's (unitary) cells arranged in series, in combination with a spring K_0. The ith Kelvin-Voigt's cell is composed by a purely viscous damper η_i and a purely elastic spring K_i associated in parallel. The elastic spring K_0 allows for mimicking the instantaneous elastic response.
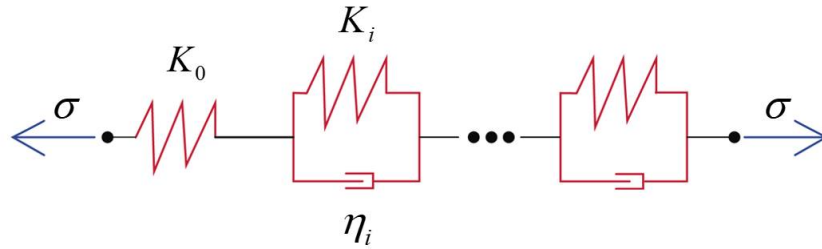
Figure 22: Representation of the generalized Kelvin-Voigt model.

Based on the Kelvin-Voigt model (with N branches), the strain $\varepsilon(t)$ and the creep function $J(t)$ are expressed, respectively, by Equations 1.8 and 1.9, as follows (Freutel et al., 2014; Anssari-Benam et al., 2011a; Gu and Li, 2011; Seifzadeh et al., 2011; Lakes, 2009; Li et al., 2005; Fung, 1993):

$$\varepsilon(t) = \int_{t_0}^{t} J(t,\tau) \cdot \frac{d\sigma}{d\tau} d\tau \qquad (1.8)$$

$$J(t) = \frac{1}{K_0} + \sum_{i=1}^{N} \left[\frac{1}{K_i} \left(1 - \exp\left(-\frac{t}{\tau_i} \right) \right) \right] \qquad (1.9)$$

Such a sum is called a Prony series (Lakes, 2009), with τ_i expressed as follows,

$$\tau_i = \frac{\eta_i}{K_i} \tag{1.10}$$

For a material that behaves according to the Kelvin-Voigt model, a sudden application of a force will not produce an immediate deflection, because the dashpot, arranged in parallel with the spring, will not move instantaneously. Instead, as shown in Figure 20, a deformation will be gradually built up, while the spring takes a greater share of the load.

The dashpot will then relax exponentially. Hence, the ratio t/τ_i, with dimensions of time, is called the *retardation time* and characterizes the dashpot's relaxation rate (Menard, 2008; Fung, 1993).

MAXWELL MODEL

A generalized Maxwell model (Figure 23) is composed by a series of Maxwell's cells arranged in parallel with a spring K_0. The ith Maxwell cell is formed by a purely viscous damper η_i and a purely elastic spring K_i associated in series. The elastic spring K_0 represents the instantaneous rigidity.
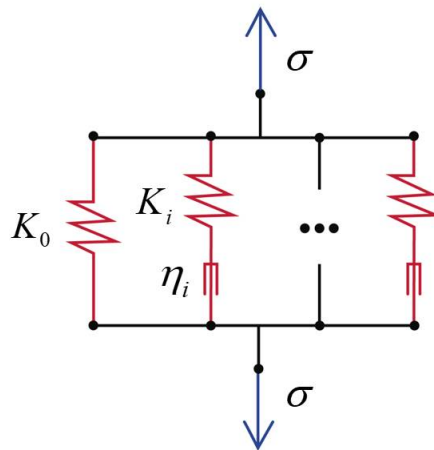
Figure 23: Representation of the generalized Maxwell model.

Based on the Maxwell model (with N branches), the stress $\sigma(t)$ and the relaxation function $R(t)$ are expressed, respectively, by Equations 1.11 and 1.12, as follows (Freutel et al., 2014; Screen

et al., 2013; Anssari-Benam et al., 2011a; Gu and Li, 2011; Seifzadeh et al., 2011; Lakes, 2009; Li et al., 2005; Fung, 1993):

$$\sigma(t) = \int_{t_0}^{t} R(t,\tau) \cdot \frac{d\varepsilon}{d\tau} d\tau \qquad (1.11)$$

$$R(t) = K_0 + \sum_{i=1}^{N} \left[K_i \exp\left(-\frac{t}{\tau_i}\right) \right] \qquad (1.12)$$

with τ_i expressed according to,

$$\tau_i = \frac{\eta_i}{K_i} \qquad (1.13)$$

For a material that behaves according to the Maxwell model, a sudden deformation induces an immediate spring's reaction, which is followed by a relaxation period, as shown in Figure 21. The ratio t/τ_i, with dimensions of time, is called the *relaxation time* and characterizes the force's decay rate (Menard, 2008; Fung, 1993).

Most soft tissues exhibit both creep and stress-relaxation behaviours when subjected to specific loading conditions. However, Kelvin-based models can only accurately characterize creep-recovery, while Maxwell-based models can only accurately describe stress-relaxation. Previous studies of Anssari-Benam et al. (2011b) and Thornton et al. (2001) have supported the application of one model to describe creep and a separate model to describe stress-relaxation, even for the same tissue.

1.7 State-of-the-art

During the past few decades, simulations using Finite Element Models (FEM) contributed for some of the most important advances in Biomechanics, for instance, on knee, hip, and spine. Their benefits are mostly related to the possibility of adjusting all the parameters of a given simulation, i.e., number of elements, material properties and laws, and boundary conditions (Marchesseau et al., 2010). In addition, some biological structures are not easy to study *in vivo*. So, the prediction of their

behaviour throughout computational models are rather important for some clinical applications, from evaluation and diagnosis to treatment planning and assistance (Freutel et al., 2014).

For those achievements, it is fundamental to obtain realistic geometric configurations of the biological structures. Hence, medical image modalities, such as magnetic resonance imaging (MRI), computational tomography (CT), and echography have been used to accurately describe the anatomical configuration of many soft tissues and bones (Marchesseau et al., 2010; Hawkes et al., 2004).

Since 1984 (Sauren et al., 1984), several research groups around the world have applied Finite Element Analysis (FEA) to study cartilage. Samples were mostly harvested from menisci, subchondral bones, elbow, and intervertebral discs of animal cadaveric models. So far, there are no studies on characterization of the mechanical response of human nasal cartilages. Although a significant effort has been made to improve surgical techniques to prevent known problems that arise from a primary rhinoplasty, much less solutions come up from an engineering point of view.

The objective of almost all reviewed works is the combination of FEM with experimental data to obtain the best agreement, as shown by Weiss et al. (2005). Indeed, one of the most challenging aspects in numerical simulations is the extrapolation of experimental data to a set of constitutive parameters to feed the simulations. Usually, model constants are obtained by curve-fitting (inverse methods), which constitutes an easy and simple method. Some researches pointed out numerical models to describe tissue's macroscopic behaviour without considering its hierarchical organization (Fallah et al., 2016). However, neglecting the internal microstructure may lead to simplifications that cause significant errors in numerical results. By bearing this aspect in mind, some researchers have considered the material hierarchical structure and organization, which implicates considering much more complex constitutive equations with parameters of viscosity, porosity, and osmotic pressure to describe both macro and microscale behaviours.

FEM are not new in the mechanical characterization of soft tissues. Knowledge has evolved from pioneer 2D to more realistic 3D simulations, with the fast evolution and capacity of computational technology. On the one hand, one of the first FE simulations were proposed for menisci (Sauren et al., 1984) and was highly geometrically simplified using a linear elastic, isotropic, and axisymmetric model. On the other hand, the most up-to-date studies applied complex and accurate models of skin (Boyer et al., 2013), periodontal ligaments (Natali et al., 2011), intervertebral discs (Schmidt et al., 2010), spine (Zanjani-Pour et al., 2016), and articular cartilage (Seifzadeh et al., 2012; 2011). Those include the effect of several boundary conditions, the application of various constitutive equations to describe the

same phenomena (through static or time-dependent conditions), rate-sensitivity, and solid/fluid behaviours separately (Fallah et al., 2016; Sayed et al., 2008).

The study of articular cartilage (AC) began in 1743 (Mow et al., 1980) and has intensified in the early 1920s (Kwan et al., 1990). As so, this section intends to review some of the most significant advances in the simulation of cartilaginous structures that allowed accurate evaluations in diverse clinical fields. Also, it demonstrates how FEM have evolved during the past few years and how it helps understanding meniscus, AC, and other soft connective tissues, since few knowledge is available on mechanical characterization and FE simulations of human/animal nasal cartilages.

After Sauren et al. (1984), who proposed a simple axisymmetric FE model of the femorotibial joint, more detailed analysis appeared with better segmented geometries loaded within variable physiological parameters. Sauren et al. (1984) and Schreppers et al. (1990) recognized that one of the most important functions of menisci is the load carrying capacity, which contributes for load transmission at the joints, and thus, reduces the stress in femorotibial contact areas. Also, it was shown, throughout the same model, that the non-linear meniscal radial displacement occurs under an axial load. The meniscus was first assumed as an isotropic linear elastic model (Sauren et al., 1984) and then as a transversely isotropic model (Schreppers et al., 1990). This also included soft layers of AC both at the ends of femoral and tibial bones, modelled as isotropic and linear elastic materials, but none have included friction contact conditions (Sauren et al., 1984; Schreppers et al., 1990).

Later, in 1992, Spilker et al. proposed an axisymmetric geometric FE model of the meniscus based on a biphasic/poroelastic model. He recognized the interaction between solid and fluid components, in contrast with previous studies, in which menisci and AC were assumed to be single-phase, homogeneous solid materials (Kempson et al., 1971; Hoch et al., 1983).

The biphasic or linear KLM (i.e., Kuei, Lai and Mow) theory, already described by Holmes et al. (1985) and Mow et al. (1989), pointed out that the responsible mechanism for the AC viscoelasticity is the diffusive interaction between solid and fluid phases. Holmes' objective was to demonstrate the importance of this interaction through uniaxial stress-relaxation tests (when a ramp displacement is imposed) depending on the permeability of the cartilage. Though Holmes' work has been developed in 1985, the approach was quite advanced, and the outcomes have inspired other researchers to consider the role of interstadial fluid within the solid matrix in indentation creep and stress-relaxation simulations. The first evidence of such inspiration has come from a mathematical approach developed by Mak et al. (1987), who performed contact modelling without friction. Then, with a numerical algorithm of a time-dependent biphasic creep-recovery experiment by Mow et al. (1989), also with frictionless contacts

between a porous-permeable indenter and the top surface of the cartilage. In the perspective of Mow and co-workers, three intrinsic material properties are enough to describe time-dependent behaviour of AC *in situ*: Young's modulus, Poisson's ratio, and permeability. However, their drawbacks were the frictionless contacts and the assumption of the material isotropy, homogeneity, and constant permeability.

Spilker and co-workers (1992) studied the time-dependent viscoelastic behaviour of the meniscus through a FE model, where the solid phase was modelled as a fibre-reinforced, transversely isotropic material filled with interstitial fluid based on Mow et al. (1989; 1980) accounting for the highly fibrous nature of those tissues. The results showed that the fluid phase carry a significant part of the applied load, and thus, the definition of permeability parameters is crucial to study the changes on time-dependent responses. In addition, other fields of interest were registered such as stress, pressure, and strain distributions as a function of time, which could lead to meniscal failure. One of the most important conclusions was that the whole tissue behaved as a compressible structure, due to fluid exudation (Mak et al., 1987), even though each one of the components was assumed to be intrinsically incompressible, following Spilker and Suh, 1990.

In the same year (1992), Spilker, Suh and Mow presented a FEA on the indentation of cartilage using the same KLM biphasic model. Some interesting issues were investigated, such as the specimen thickness effect, indenter porosity, and indenter-tissue interface contacts. Results were compared in cases of the indenter impermeability, perfect adhesive interface between tissue and indenter, and that of a porous and free-draining indenter with a frictionless tissue-indenter interface. These authors found that adhesion at the indenter-cartilage interface plays an influence both at time-dependent and equilibrium responses. However, the indenter porosity only significantly changed the time-dependent response (not the equilibrium response). These effects also varied significantly with the specimen thickness.

As the interest in femorotibial joint increased, later studies were carried out using linear elastic isotropic models that are highly simplified and easier to compute (Peña et al., 2005a; Périé and Hobatho, 1998). Périé and Hobatho (1998) described a simplified three-dimensional FE model of the femorotibial joint from MRI (Magnetic Resonance Imaging) of a healthy human adult to quantify *in vivo* contact areas and hydrostatic pressure. Later, Haut Donahue et al. (2003) reported that the contact pressure distribution on the knee is better described with a direction-dependent constitutive law than through an isotropic law, due to the predominant collagen fibres arrangement in menisci and AC. This conclusion was based on an ABAQUS® FE model validated with experimental data from a complete

healthy human cadaveric knee. The geometry used by these authors was previously described by Haut Donahue et al. (2002), in which an accurate three-dimensional model of the knee was constructed. The bones were assumed as rigid, meniscus was considered transversely isotropic (same properties in two orthogonal directions), and both femoral and tibial AC were regarded as linear elastic and isotropic materials, with an elastic modulus of 15 MPa and Poisson's ratio equal to 0.475. The contacts between surfaces were frictionless (Haut Donahue et al., 2002).

It is essential to note that cartilage is highly hydrated, with water content rising up to 80% by weight (DiSilvestro and Suh, 2002), presenting non-negligible non-linearities that can influence both experimental and numerical results. Beillas et al. (2007; 2004) proposed generic FEM from MRI scans to study the knee response during a strenuous activity and a one-legged hop, respectively. Both joint kinematics and cartilage deformations were computed. In these models, bones were modelled through an isotropic elastic material law with different Young's moduli ranging from cancellous, cortical, and subchondral bones (75-450 MPa, 16-17.5 GPa, and 5 GPa, respectively). Instead of using viscoelastic laws, both cartilage and menisci were approximated through an isotropic elastic law (Beillas et al., 2007). According to this study, Beillas et al. (2007) have shown that cartilage properties are highly rate-sensitive, supporting the importance of considering anisotropic formulations. However, for short loading duration, AC could be considered nearly elastic as the water (synovial fluid) has no time to flow through the porous solid matrix.

Peña and co-workers presented an important set of publications in the field of numerical characterization of AC. They registered an evolution from 2005 to 2008, in which FEM were successively more complex and extended not only for meniscus and AC, but also for tendons and ligaments.

Two years before Beillas' investigation, Peña et al. (2005a; 2005b) developed a human knee joint model (user-subroutine) in ABAQUS®, in which soft tissues were modelled as isotropic, homogeneous and either linear elastic (AC and menisci) or non-linear hyperelastic (anterior cruciate ligament). Femur and tibia were considered as rigid due to their much higher stiffness comparing to other tissues. In these studies, solid models of tibia, femur, menisci, and cartilage were created from MRI and then meshed in ABAQUS® CAE. AC was modelled with an elastic modulus of 5 MPa and Poisson's ratio of 0.46. Once again, the loading time corresponded to that of a single leg stance, so this simplified model was just accurate enough to predict short-term cartilage response (Peña et al., 2006; 2005b). The studies of Peña constituted an interesting contribution within the orthopaedic field, since

they allowed to prove that, due to meniscectomy, contact stress increases, which likely accelerates early cartilage degeneration.

Similar conclusions came out one year later, in 2006. Vadher at al. (2006) pointed out that medial meniscectomy (greater than 20%) drastically increases contact stress in the knee joint. For that purpose, the authors developed more sophisticated FEM to understand the effects of partial meniscectomies on stress distribution. The meniscus was characterized with a transversely isotropic elastic formulation. However, the major contributions of this study were that AC was modelled through three distinct layers: a poroelastic transversely isotropic superficial layer, and poroelastic isotropic middle and deep layers, including a calcified thin layer near the subchondral region (Vadher et al., 2006). The poroelasticity of the model supports better the assumption of an ideal biphasic behaviour. However, they assumed an ideal geometry (an axisymmetric model), which may not be sufficiently accurate as to replicate the geometry of a realistic structure. Six years later, Mononen et al. (2012) investigated the effect of superficial collagen fibril patterns (split-lines) and collagen fibrillation on the stress and strain distributions in the human knee throughout a FEA in ABAQUS®. The cartilaginous components were modelled as fibril-reinforced viscoelastic materials with depth-dependent collagen orientations, in which the matrix was further subdivided into a poro-hyperelastic, non-fibrillar part and a viscoelastic, fibrillar part. In this study, the authors did not consider the existence of any fluid flow across cartilage surfaces. Stress, strain, contact, and pore pressures were simulated during impact loading.

More recently, further investigations were performed with similar FEM (using ABAQUS®) for bones, AC, and soft connective tissues, with emphasis on the anterior cruciate ligament (Peña et al., 2007a; 2006; Ramaniraka et al., 2007).

The consideration of viscoelastic effects became more frequent among the researcher community in the last decade. The simplest and mostly used viscoelastic models to describe global time-dependent response of biological materials (short- and long-term response) are the discrete Kelvin-Voigt (creep) and the discrete Maxwell (stress-relaxation) models (Freutel et al., 2014). However, many other viscoelastic constitutive models were proposed in the past. Fung (1993) proposed a theory known as "*theory of quasi-linear viscoelasticity*" (QLV), which was widely used in the literature to characterize soft biological tissues subjected to dynamic and repetitive long-term loading *in vivo*, such as ligaments, tendons, cardiac muscles, and aortic valves (Anssari-Benam et al., 2014). QLV provides a powerful mathematical tool (non-linear superposition integral) for estimating time-dependent parameters, in

which the relaxation function depends on both time and strain (history dependence) and the compliance depends on both time and stress (Lakes, 2009; Rajagopal and Wineman, 2008).

For linearly viscoelastic materials, stress and strain depend on time only (Lakes, 2009). As an example, a linear viscoelastic theory based on a Kelvin-Voigt model was used by Peña et al. (2007b), while a Maxwell-type was presented by Holzapfel et al. (2002). However, these models do not account for creep and stress-relaxation simultaneously (Fung, 1993).

Peña et al. (2007b) described a fully three-dimensional anisotropic visco-hyperelastic Kelvin-Voight-based model for ligaments and tendons undergoing finite strains. Such model has successfully demonstrated relaxation curves along time. The news here were the assumption of distinct viscoelastic behaviours for the matrix and different families of fibres, in contrast with Limbert and Middleton (2004), who proposed a general transversely isotropic visco-hyperelastic constitutive formulation for ligaments without separating viscous effects of the ground substance and fibres. Creep and stress-relaxation studies have also been extended to characterize menisci and AC, including not a constant, but a strain-dependent permeability (Seitz et al., 2013; Seifzadeh et al., 2012; 2011).

Peña's concern on non-linear mechanical behaviour of human ligaments proceeded one year later, in 2008, to predict creep rate dependence on the applied stress and relaxation rate dependence on the applied strain. Further, Peña et al. (2008) maintains the dependency on time and the assumption of different viscoelastic parameters for the matrix and fibres. It must be highlighted that the non-linear viscoelastic behaviour of ligaments was already described in previous studies. Hingorani et al. (2004) and Bonifasi-Lista et al. (2005) found that creep rate depends on the applied stress and relaxation rate depends on the applied stretch. The hypothesis of Hingorani et al. (2004) was corroborated with their experimental data. Results showed that the rate of relaxation decreases with the increase of the initial strain that is applied to the soft tissue, while the rate of creep reduces with higher applied stresses. The displacement or force, respectively, was applied for a period of 100 s, followed by 1000 s of recovery, while remaining hydrated (Hingorani et al., 2004). The minimum relaxation period presented by Bonifasi-Lista et al. (2005) was also 1000 s in both strain- and direction-dependent experiments.

Creep and stress-relaxation studies have also been extended to characterize menisci and AC, including not a constant, but a strain-dependent permeability (Seitz et al., 2013; Seifzadeh et al., 2012; 2011). Seifzadeh et al. (2012; 2011) described a fibre-reinforced biphasic poro-hyper-viscoelatic model of AC that accounted for the fibre reorientation and dispersion, as well as the intrinsic viscoelasticity, of the non-fibrillar matrix. In both studies, the authors combined an optimization algorithm with an

ABAQUS® FEA to determine material parameters (i.e., an inverse method). The strain-dependent permeability took the form described by Lai et al. (1981).

Regarding auricular and nasal structures, some studies came up much more recently, with less complex formulations. Ramprasad and Frank-Ito (2016) used a computational fluid dynamic modelling package to characterize the effects of different nasal vestibule phenotypes, classified as standard, notched, and elongated, on nasal airway patency. The accurate three-dimensional (3D) sino-nasal geometry was constructed using common CT-scans through the software Avizo™ 8.1 and meshed in ANSYS®. Only nostrils and nasal cavities of the internal nose were modelled. Results suggested that at localized regions of the nasal cavity, average resistance was significantly different among nasal vestibule phenotypes, except from nostril to choana (Figure 10). De Greef and co-workers (2017; 2015) studied the effect of model definitions, especially the isolated effect of the geometry of temporal bones, on human middle ear mechanisms of sound transmission. Those were segmented from high-resolution CT scans and meshed using Comsol® Multiphysics 5.2. However, the importance of the cartilaginous structures was almost neglected.

To sum up, the state-of-the-art of cartilage modelling reflects that its global behaviour is very complex with poro-hyper-viscoelatic material parameters together with high strain- and direction-dependency (Guo et al., 2015; Taffetani et al., 2014). The most complete models use all these features, even if some studies still neglect the impact of the strain-dependent permeability or fibre reorientation. Nonetheless, when these features are considered, the osmotic swelling is either neglected or the implementation of corresponding boundary conditions lead to a drastic increase in complexity of the analysed models (Lai et al., 1991). As so, each model and corresponding boundary conditions must be suitable for the aim of each study.

From the presented literature review, it is also clear that the evaluation of some parameters through experimental protocols is fundamental to perform reliable numerical simulations. Keeping this in mind was paramount to stablish the protocols of the next Chapter.

CHAPTER 2

Materials and Methods

This chapter is divided in two foremost sections, in which experimental details and numerical methods are presented and justified. The frequency-dependent viscoelastic properties (storage and loss moduli) of porcine auricular cartilages and human nasal cartilages are determined using Dynamic Mechanical Analysis (DMA) up to 20 Hz. Besides, general thermal features are also thoroughly characterized using Thermogravimetry (TGA) and Differential Scanning Calorimetry (DSC). Data fitting of the time-dependent curves to discrete viscoelastic models (Kelvin-Voigt and Maxwell) is useful for estimating both instantaneous responses and damper characteristic times of creep and stress-relaxation. Regarding mechanical modelling subchapters, a hyper-viscoelasticity theory is presented and applied to a home-made FE solver to simulate the experimental creep and stress-relaxation rheological conditions.

2. Materials and Methods

This chapter is divided in two main sections, in which the experimental details and numerical methods are presented. Experimental protocols are further applied to porcine auricular and human nasal cartilages.

2.1 Die-cutting Tools

The mechanical characterization of soft tissues requires the preparation of specimens with established geometries (shapes) and dimensions that have to be easily replicated. This task involved the production of: (a) cylinder-shaped specimens to undergo compressive tests; And (b) *dog-bone*-shaped specimens to conduct tensile tests. The former were used to execute multi-frequency compressive tests in porcine auricular and human nasal cartilages, with approximately flat and regular surfaces, being obtained with a standard hollow-punch (Figure 24) of 7 mm (inner diameter).

Figure 24: Standard hollow-punch for cylinder-shaped samples.

The later was employed both in tensile creep and relaxation tests, as well as in quasi-static loading (in porcine auricular and human nasal cartilages). The shape of the die-cutting tool (Figure 25a) was inspired in the ASTM D412 standard tensile test method for vulcanized rubber materials (Sugavaneswaran and Arumaikkannu, 2014; Annaidh et al., 2012), applying a scale factor of 4/25 to fit with the grips of the DMA equipment used in the experiments. The die-cutter was fabricated by electro-erosion technique in a high resistant steel, presenting a continuous blade 8 mm above the quadrangular base (cutting angle of 25º). Smaller *dog-bone* shapes are better placed in soft biological tissues since they are also excised from small biological structures, where the availability of flat surfaces and regular thicknesses are even more reduced. This strategy required the use of a (polymeric) hammer to produce the impact between the blade and the biological samples against a PVC slab. Nominal dimensions of the *dog-bone*-shaped die-cutter are shown in Figure 25b.
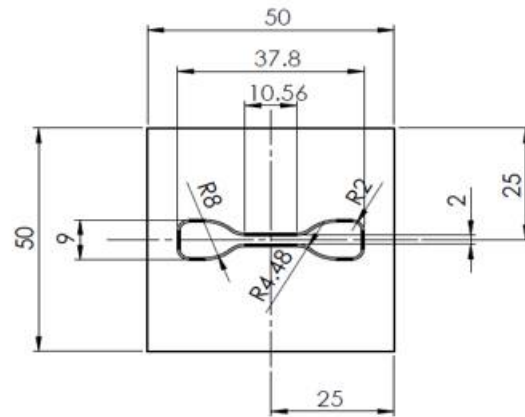
| (a) | (b) |

Figure 25: (a) ASTM D412 inspired die-cutter and **(b)** corresponding nominal dimensions (in mm).

2.2 Experimental Details

Similar experimental procedures were applied to prepare both porcine and human samples. Porcine samples were used to establish the experimental protocols to be employed in human tissues.

2.2.1 Preparation of Porcine Samples

Several ears from adult porcine cadavers were obtained from a local butchery (Guimarães, Portugal). No information was required about the age of the animals, as long as their freshness was guaranteed. Upon arrival in the laboratory, samples were dissected into flat and approximately regular thickness pieces, which were in fact small composites of cartilage and traces of subcutaneous/fatty tissue. Following Arroyave et al. (2015), samples were carefully buffered with phosphate saline solution (PBS) or distilled water to avoid dehydration during dissection and loss of tone of the tissues. Therefore, the surfaces were not allowed to become dry.

The second step consisted in removing the overlying soft tissue. This was firstly executed with a scalpel to cut the excessive amount of subcutaneous tissue and then with a razor blade scraping along the cartilage surface. Scraping always began in the same region (not considered for testing) and along the same direction to prevent damage on the testing area. It was always possible to identify a region of interest for testing. In some cases, however, this meant testing near a lesion site. Regions showing clearly pre-existing surface lesions were not considered. The final configuration of the samples depended on which matrix had been used to cut (section 2.1).

Following samples preparation, the specimens were stored in two different ways. Firstly, they were bathed in physiological saline solution (8 g/L NaCl) to match the conditions of those of the human

body. Secondly, they were stored directly after dissection to maintain their natural turgidity (Hayes and Bodine, 1978). These two procedures allowed to understand the effect of tissue hydration on frequency-dependent viscoelastic properties comparing the results with samples tested in natural and turgid conditions (Pearson and Espino, 2013).

Afterwards, samples were sealed in a plastic container and stored in a freezer at -40 ºC, until required for testing. Such freeze-thaw treatment has been previously shown not to change the dynamic mechanical properties of cartilages (Espino et al., 2014; Pearson and Espino, 2013; Fulcher et al., 2009). The defrost process consisted in thawing the samples naturally until room temperature (Ronken et al., 2012). The whole procedure for specimen preparation is shown in Figure 26.

As referred above, these experiments allowed to validate the testing protocols for the next set of specimens (section 2.2.2), which are much more sensitive and less available.

Figure 26: A procedure for porcine auricular cartilage samples preparation.

Nasal cartilages were harvested from human cadavers by a facial plastic surgeon in Egas Moniz Institute, Caparica, according to the established ethical guidelines of the Portuguese Health Authorities. Samples were harvested from two Caucasian male donors of approximately same age (> 70 years), preserved by cryoprecipitated plasma. Periosteum and perichondrium layers were manually removed from nasoseptal cartilages (NS), ULC, and LLC (Figure 27). Remaining loose connective tissue was also carefully removed using a simple scissor to prevent slippage within the grips during testing (Kim et al., 2012). Discs, *dog-bone*-shaped samples, and strips were cut according to previous description. They were kept directly after dissection to maintain their natural turgidity, sealed in a plastic container, and stored in a freezer at -40 ºC. Once again, this has been previously shown not to change the dynamic mechanical properties of cartilages (Espino et al., 2014; Pearson and Espino, 2013; Fulcher et al., 2009). Prior to mechanical testing, specimens were submitted to individual defrosting processes, which consisted in thawing the samples naturally at room temperature.
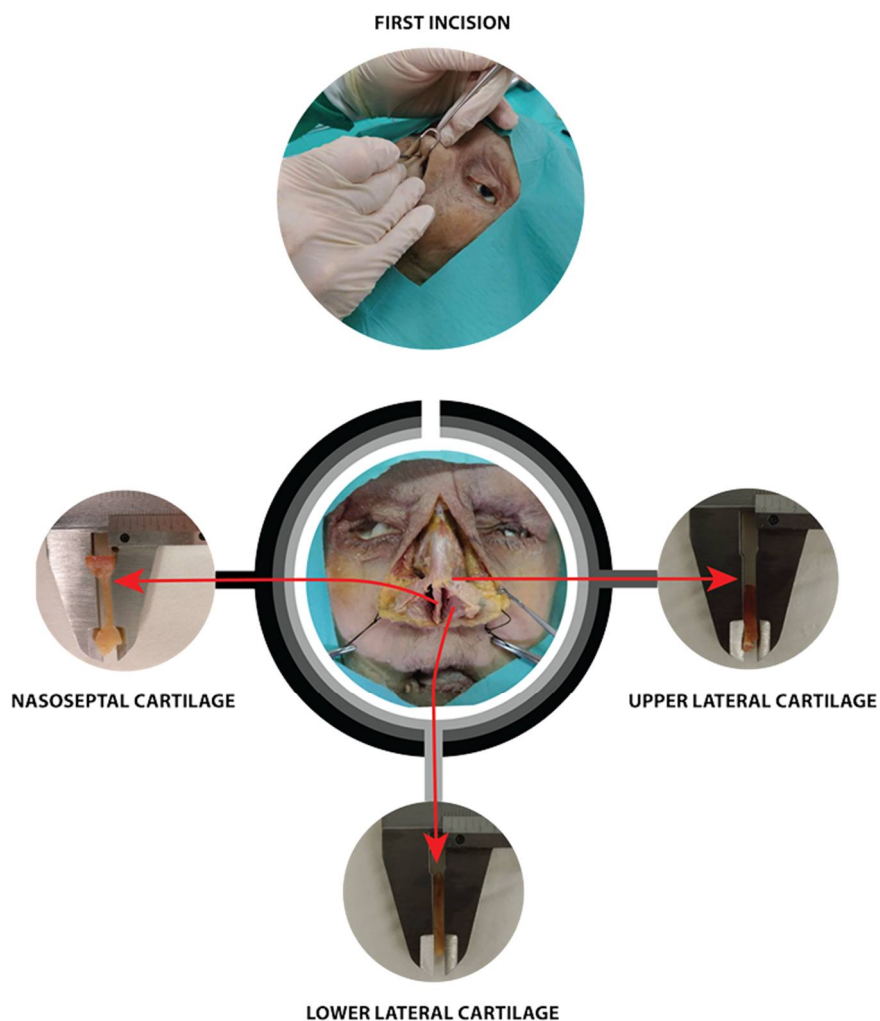
Figure 27: Harvesting of nasoseptal cartilages (*dog-bone*-shaped), ULC (strips), and LLC (strips) from the human nose.

2.2.3 Thickness and Width Measurements

Thickness and width were both accurately measured using ImageJ/Fiji to Java® 8 (https://imagej.net/Fiji/), which is an open-source image processing program with many general functionalities.

Each sample was previously identified with a specific code: (a) test identification; (b) type of cartilage; (c) donor; And (d) position. Ten different measurements of composites (cartilage and subcutaneous tissue) and "pure" cartilage were obtained along the specimen length and width by capturing a photography of each specimen close to a vernier caliper (Kraftwerk 2970, Bischoffsheim, France) (resolution: 0.05 mm) at the same field depth (Figure 28). Measuring stacks were automatically registered by setting a scale (pixels/mm) from the obtained images. Thicknesses and widths were then used to determine the cross-sectional area of each sample.
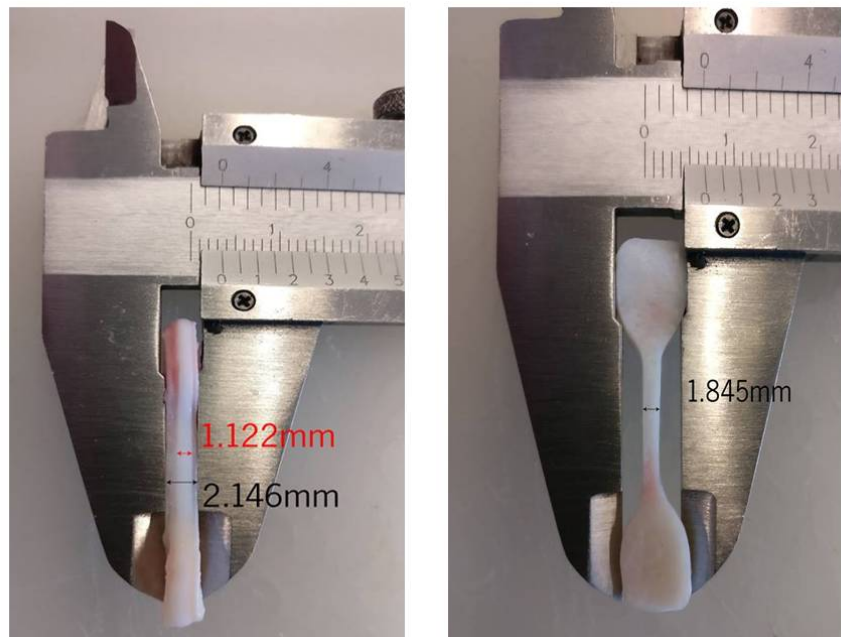
Figure 28: Method for determination of the average thickness and width. Sample name: *3S1E* (third sample of the porcine ear #1). Scale: 50.0044 pixels/mm.

2.3 Experimental Tests

The frequency-dependent viscoelastic properties of porcine auricular cartilages and human nasal cartilages were determined in tensile and compressive testing modes up to 20 Hz using Dynamic Mechanical Analysis (DMA). Time-dependent creep and stress-relaxation behaviours were also studied and fitted to discrete viscoelastic models (Kelvin-Voigt and Maxwell). Besides DMA, general thermal features were also thoroughly characterized using Thermogravimetry (TGA) and Differential Scanning

Calorimetry (DSC), in which weight loss (WL) and glass transitions (T_g) were determined. Moreover, the study of cartilage in quasi-static conditions is justified by the fact that the loading intensity to undergo dynamic mechanical analysis had to be evaluated in advance. In addition, quasi-static conditions are adequate to characterize the nasal cartilages, as they are frequently loaded statically in physiological conditions. Uniaxial tensile tests at small displacement rates were also performed.

2.3.1   Uniaxial Tensile Tests

This study aims at investigating quasi-static properties of cartilage at small displacement rates. For this purpose, 5 *dog-bone*-shaped porcine specimens (in quasi-dehydrated conditions) were subjected to tensile loading at a constant displacement rate and room temperature (21 °C).

According to Avanzini et al. (2014), when testing this type of material, special care is needed both to prevent damage initiation in cartilage samples during clamping and slippage within the grips. Therefore, specimens were clamped using small pieces of sandpaper to counteract their tendency to slip. The grip-to-grip distance (gauge length) was set to 23 mm. Prior to testing, a low tare load was applied to establish a consistent zero position. The adjusted distance between grips was then used as the initial length (Anssari-Benam et al., 2011a).

Load-displacement curves were obtained using a Hounsfield Universal Testing Machine (Hounsfield UTM) with a 250 N load cell and a cross-head velocity set to 0.3 mm/min. Stress-strain curves were plotted to determine the Young's modulus (MPa), the Ultimate Tensile Stress (UTS) (MPa), and the failure strain of the specimens. Table 1 shows the average dimensions and relative composition of each specimen.

Table 1: General information of the porcine auricular cartilage (PAC) specimens.

Specimen name #Test no.	Average dimensions (mm)		Relative composition (%)	
	Thickness	Width	Cartilage	Subcutaneous
PAC #1	2.148	1.796	65.7	34.3
PAC #2	2.026	1.827	65.5	34.5
PAC #3	3.590	1.845	42.0	58.0
PAC #4	3.743	1.930	41.2	58.8
PAC #5	3.267	1.968	51.5	48.5

DMA is a highly accurate technique used to study dynamic properties of a variety of materials, from polymers (Koupai et al., 2017) to soft biological tissues (Zhang et al., 2017; Marchesseau et al., 2010; Nicolle et al., 2010).

The equipment measures the stiffness and damping as function of time, temperature, and/or frequency. It consists fundamentally on the application of a low-amplitude sinusoidal stress or strain to a viscous solid material. The response within the material viscoelastic regime is a sinusoidal oscillation with similar frequency but out of phase by an angle δ (Figure 29). Based on the specimen geometry, the loading intensity or applied displacement, the apparatus is able to control, respectively, the deformation or applied stress (creep and relaxation), loading rate (stress or displacement) and loading time, as well as the applied loading frequency and temperature (Zhang et al., 2017; Menard, 2008).
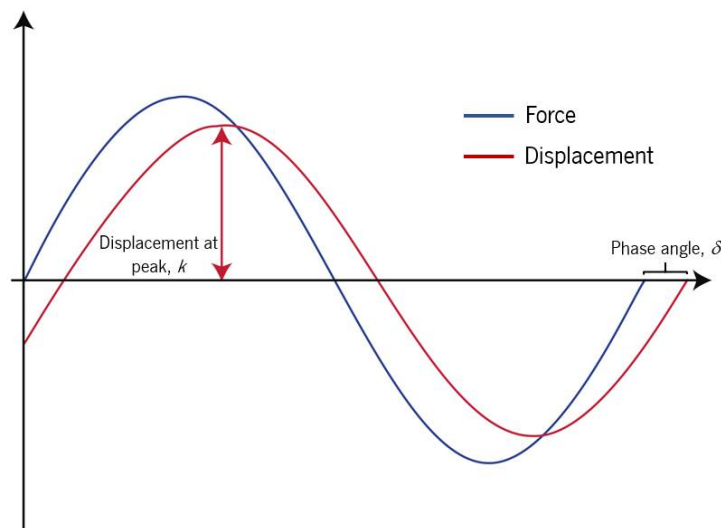
Figure 29: DMA applies a sinusoidal stress that generates a sinusoidal strain. By measuring the amplitude of the deformation at the peak of the sine wave and the phase angle, storage and loss moduli and damping can be determined.

The viscoelastic properties directly obtained from the apparatus are the storage modulus (pure elastic response, E'), the loss modulus (pure viscous response, E''), and the loss factor, $\tan\delta$ (also known as loss tangent or damping) that is calculated from the loss angle δ. The storage modulus of a material characterizes the ability of such material to store mechanical energy, which is available for elastic recoil once the stress is removed. As its name suggests, the loss modulus quantifies the ability of a material to dissipate mechanical energy. The damping quantifies the efficiency to lose energy as heat in molecular rearrangements and internal friction (Menard, 2008).

The storage modulus is, however, not the same property as the Young's modulus, obtained from the slope of the stress-strain curves in the linear elastic regime. The storage modulus is calculated

within every discrete time interval. Besides, in tensile stress-strain tests the material is constantly stretched, whereas in dynamic tests the material is continuously oscillated (Brostow et al., 2010; Menard, 2008; Fortis et al., 2004). A complex or dynamic modulus $E*$ depending on elastic and loss components, is represented in Figure 30 (Menard, 2008).
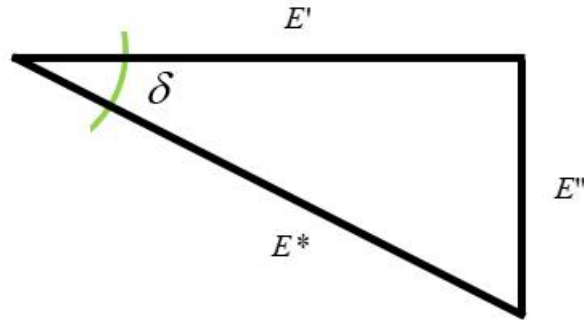
Figure 30: The complex modulus depends on both the elastic (real) and loss (imaginary) components.

Equation 2.1 gives the value of the dynamic modulus $E*$ (Temple et al., 2016; Espino et al., 2014; Fulcher et al., 2009; Menard, 2008):

$$\left|E*\right| = \left|E' + iE''\right| = \sqrt{E'^2 + E''^2}$$ (2.1)

The phase angle δ is given by Equation 2.2 (Temple et al., 2016; Fulcher et al., 2009):

$$\delta = \tan^{-1}\frac{E''}{E'}$$ (2.2)

Thus, Equation 2.3 represents the value of tanδ as a function of the storage and loss moduli, or stored and loss energy (Menard, 2008):

$$\tan\delta = \frac{E''}{E'} = \frac{\eta'}{\eta''}$$ (2.3)

where η' is a measure of the energy loss and η'' is the stored energy (Menard, 2008). Hence, a phase angle of 0º indicates that a material has purely elastic behaviour, while a phase angle of 90º indicates a purely viscous response (Fulcher et al., 2009; Mark, 2007; Tanaka et al., 2006).

DMA is very sensitive in identifying small transitions, especially of second-order, that are sometimes undetectable using DSC. Actually, it is 10 to 100 times more sensitive to changes at the glass transition T_g and melting T_m temperatures, which are the most relevant first-order transitions (Menard, 2008). The criteria to determine the T_g depends only on the operator background. The peak of the $\tan\delta$, the onset of the E' drop, and the onset or peak of the E'' curve could be used. For instance, if a material is heated so that it passes through its glass transition and changes from glassy to rubbery, the storage modulus will often drop several decades, which is accompanied by a rise in $\tan\delta$. The assessed values can differ up to 25 °C from one another and still be accepted. Moreover, frequency-dependent behaviour of materials also gives some insight on molecular structures.

The DMA has already been used to study frequency-dependent viscoelastic properties of porcine, bovine, and human cartilages in a wide range of temperatures, since cartilage behaves mechanically as a viscoelastic solid material (Temple et al., 2016; Sadeghi et al., 2015; Espino et al., 2014; Pearson et al., 2013; Ronken et al., 2012; Fulcher et al., 2009; Stolz et al., 2004). However, its exactly behaviour under the full range of physiological loading frequencies is still unknown (Fulcher et al., 2009). Articular cartilage viscoelastic properties have been studied from a standard walking pace (1 Hz), to healthy gait heel-strike relevant frequencies (3-5 Hz) and up to traumatic heel-strike frequencies (90 Hz) (Sadeghi et al., 2015; Pearson et al., 2013). The rise time t_{rise} of the force is given by the time from the trough to the peak of the sine wave, according to Equation 2.4 (Fulcher et al., 2009):

$$t_{rise} = \frac{1}{2\,fr} \qquad\qquad (2.4)$$

where fr is the frequency of the sine wave.

The standard walking pace corresponds to a rise time of 500 ms (Fulcher et al., 2009). Frequencies up to 90 Hz represent fast heel-strike rise times, which are likely implicated in impulsive/traumatic loading situations usually associated with an impact (Sadeghi et al., 2015).

Although some researchers have proposed methods that use frequencies less than 1 Hz (0.1 Hz by Ronken et al., 2012; 0.5 Hz by Fortis et al., 2004; 0.01 Hz by Tanaka et al., 2006), common testing machines have some limitations to determine viscoelastic properties below 1 Hz, and thus, to assess heel-strike rise times of short duration (Sadeghi et al., 2015; Fulcher et al., 2009).

DMA experiments were performed using a DMA 7100, Hitachi®, Japan. The distance between grips was adjusted for each sample.

TENSION AND COMPRESSION

DMA was performed both in tension and compression according to internal methods (procedures) previously programmed in the operating software. In tension, specimens were loaded axially relatively to the straight region. In compression, a 10 mm diameter circular accessory was attached to the actuator of the testing machine.

The described moduli were determined over a range of frequencies from 1 to 20 Hz in synthetic oscillation (the first frequency was set to 1 Hz, the others were automatically displayed at 2, 4, 10, and 20 Hz). Porcine auricular cartilages and human nasal cartilages were all tested in quasi-dehydrated conditions. Temperature-dependent storage modulus, loss modulus, and tanδ were directly calculated by the equipment operating software. Testing conditions are specified in Table 2. The analysis was carried out under nitrogen purge (200 mL/min) to guarantee an inert environment.

Table 2: DMA testing conditions for porcine auricular cartilages (PAC) and human nasoseptal cartilages (NS).

Testing conditions	Tension	Compression
Number of samples	PAC (4); NS (3)	PAC (4); NS (3)
Frequency sweep (Hz)	1, 2, 4, 10, 20	
Temperature range (°C)	30-250	
Temperature rate (°C/min)	3	
Sampling acquisition (Hz)	3	
Specimen dimensions/diameter (mm)	ASTM D412 (adapt. Figure 25b)	7
Observations	Quasi-dehydrated conditions	

CREEP AND STRESS-RELAXATION

In creep, a constant stress of around 0.7 MPa was applied during at least 25 min, after 3 min holding to stabilize the temperature at 23±1 ºC. The use of that loading stress has been made following quasi-static tensile tests (ASTM D412 adapt. Figure 25b), in quasi-dehydrated conditions, corresponding to loading stresses that did not lead to damage (within the linear elastic regime, Figure 36c). Porcine auricular ($n = 5$) and human nasoseptal ($n = 2$) cartilages were subjected to tensile creep under quasi-dehydrated conditions. The applied force was previously calculated to replicate the applied stress magnitude in each sample. A loading ramp of 100 N/min was chosen to simulate the instantaneous loading step.

In stress-relaxation, porcine auricular ($n = 5$) and human nasoseptal ($n = 2$) cartilages in quasi-dehydrated conditions were subjected to tensile stress-relaxation at 23±1 ºC. Samples were loaded up to 0.8 mm (25% of the applied tension within the linear elastic regime, Figure 36c) during 15 min until the equilibrium (a plateau) has been reached. A holding time of 3 min was taken to stabilize the temperature. A loading ramp of 100 mm/min was applied to simulate the instantaneous displacement step. In both creep and stress-relaxation experiments, the distance between grips was adjusted for each sample.

CURVE-FITTING

Experimental data was fitted to viscoelastic models to estimate both the moduli and time-dependent parameters. The application of such models permits to establish indirectly a relationship between parametric values and the microstructure of the cartilage (Baumgaertel and Winter, 1992). Kelvin-Voigt and Maxwell DEM were fitted to estimate K_0, K_1, K_2, τ_1, and τ_2 (Equations 1.9, 1.10, 1.12, and 1.13). The data fitting was carried out using a 2D plotting tool (xmGrace v5.1.25).

2.3.3 Differential Scanning Calorimetry

DSC measurements were performed in a Mettler Toledo DSC 822e apparatus. The analysis was carried out in nitrogen atmosphere (200 mL/min) to guarantee an inert environment. DSC measures the amount of energy per unit of time or temperature absorbed or released by a testing sample (and a reference sample) when heated or cooled, providing quantitative and qualitative data on endothermic (heat absorption) and exothermic (heat release) processes. It is possible to assess first-order transitions (endothermic or exothermic peaks), to quantify peak areas directly under the curves, which are proportional to the enthalpy, ΔH (J/g) involved in the process, and some second-order transitions, which are characterized by variations in sample's heat capacity without changing the enthalpy (no peaks).

Usually, samples are firstly heat-treated to eliminate any thermal history (Asran et al., 2010) specially the water thermal history (Majda et al., 2017). Samples are then cooled for complete matrix crystallization (Asran et al., 2010). And finally, they are re-heated with the same rate to cover all endothermic peaks. However, a pre-test has shown that main transitions are verified immediately during first heating, and thus, nothing is observed when samples are heated in a second time.

In this work, each biological sample was left to defrost (from -40 ºC) at room temperature and placed into an aluminium pan. The initial mass was then measured with a digital fully automatic Mettler

Toledo calibration balance (AB 204-S/FACT Classic Plus). DSC experiments were carried out by submitting the biological samples to only one heating step from 30 to 300 ºC, at a rate of 10 ºC/min. DSC curves were plotted with heat flow versus temperature to determine the main thermal events (i.e., the melting temperature peaks and the enthalpies) (Asran et al., 2010).

2.3.4 Thermogravimetric Analysis

TGA measurements were carried out in a STA 7200 equipment, from Hitachi®, Japan. TGA is a method in which thermogravimetry (TG) and differential thermal analysis (DTA) are shown simultaneously. TG measures the mass change of a substance against time or temperature, in a defined and controlled environment, with respect to heating rate. DTA is the temperature difference between the sample and a reference material against time or temperature (Tóth et al., 2010). Thus, TGA results can be displayed as: TG curve, in which weight loss (WL) is recorded as a function of time or temperature; DTG curve, which is the first derivative of TG plotted against time or temperature. TGA gives no direct chemical information (Tóth et al., 2010).

In this work, TGA plots were obtained in a range of 30-500 ºC under nitrogen atmosphere (200 mL/min) and at 3 ºC/min. Specimens were left to defrost at room temperature and placed into an aluminium pan. The initial mass was measured with a digital fully automatic Mettler Toledo calibration balance (AB 204-S/FACT Classic Plus). Data was plotted as WL (in percentage) versus temperature (as well as DTG versus temperature), and the mass of dried residues were calculated for each case.

2.4 Mechanical Modelling

This section is dedicated to the description of the developed numerical model. It includes the mathematical formulation used to simulate the mechanics of soft tissues, its constitutive equations, and the generation of the FE mesh obtained from CT image segmentation.

2.4.1 Constitutive Laws

Constitutive equations describe the stress-strain (or stress-strain-time) relationships of a material under a general, three-dimensional stress field. There is no single constitutive equation for each type of mechanical response, especially due to difficulties in testing and measuring biological features and, more significantly, in reducing the experimental data to a general mathematical expression (Tong and

Fung, 1976). The state-of-the-art in this type of numerical formulations reveals an increasing complexity on the mechanical characterization that can be subdivided into three main directions: (a) a *purely phenomenological approach*, which consists in fitting mathematical expressions to the stress-strain curves obtained under specific (ideal) deformation rates; (b) A *continuum approach*, in which general theories are approximated to experimental data to describe hyperelasticity and viscoelasticity aspects; And (c) a *structural approach*, which intends to develop constitutive equations based on the structure of the tissue and its components (Doblaré and García-Aznar, 2010).

In this sub-chapter, the continuum formulation suited for the FE implementation and simulation of a poro-hyper-viscoelastic cartilage model is described. Since constitutive equations describe physical properties of a material, it must be independent of a set of reference coordinates. Therefore, tensors are used to formulate them.

The fundamental continuum mechanics is presented, along with derivations of the second Piola-Kirchhoff stress tensor and their FE implementation.

As stated before, cartilage is daily subjected to finite deformations. Its mechanical behaviour is highly anisotropic (Lakes, 2009), with almost incompressible components in physiological state (Spilker and Suh, 1990), and influenced by its highly poro-elasticity and water content (Richard et al., 2013).

BASIC KINEMATICS

Let Ω_0 be the configuration of an arbitrary body of interest and $\aleph: \Omega_0 \to \Omega$, $\aleph: \mathbf{X} \to \mathbf{x}$ a non-linear deformation (i.e., $\mathbf{X}$, with spatial coordinates X_1, X_2, X_3, represents the position of a particle in the reference (stress-free state) configuration, while $\mathbf{x}$, with spatial coordinates x_1, x_2, x_3, represents the particle in the deformed (current) configuration. According to this notation, Ω_0 represents a continuum body with (fixed) reference configuration at the reference time $t = 0$. Then, an assumed deformation $\left\{ \chi : \Omega_0 \to \mathfrak{R}^3 \right\}$ maps the reference configuration to a current configuration Ω at the time t (one-to-one mapping). Hence, a typical material point $\mathbf{X} \in \Omega_0$ transforms to a place $\mathbf{x} = \chi(\mathbf{X})$ $\in \Omega$ (Alastrué et al., 2007; Feng et al., 2006; Holzapfel and Gasser, 2001; Holzapfel et al., 2000).

Based on the Lagrangian description, it is appropriate to introduce a strain measure in terms of material coordinates. As so, the symmetric and positive right Cauchy-Green strain tensor $\mathbf{C}$ (Equation 2.5) can be defined as follows (Feng et al., 2006):

$$C = F^T F \tag{2.5}$$

where the deformation gradient $\mathbf{F}$ is characterized through,

$$F = \frac{\partial \mathbf{x}}{\partial \mathbf{X}} \tag{2.6}$$

Let $\mathbf{I}$ be the second-order identity tensor (Holzapfel and Gasser, 2001). $\mathbf{F}$ is a linear transformation that maps the infinitesimal small vector $\partial \mathbf{X}$ of the reference configuration into the infinitesimal small vector $\partial \mathbf{x}$ of the current configuration (Feng et al., 2006). The deformation gradient $\mathbf{F}$ can also be written as,

$$F = I + \frac{\partial \mathbf{u}}{\partial \mathbf{X}} \tag{2.7}$$

with $\mathbf{u}$ being the displacement field, $\mathbf{u}(\mathbf{X}) = \mathbf{x} - \mathbf{X}$ (Feng et al., 2006; Spencer, 1970). Furthermore, let the local volume ratio J (Holzapfel et al., 2000) be defined as,

$$J = \left[\det(C) \right]^{\frac{1}{2}} = \det(F) > 0 \tag{2.8}$$

Physically, the Jacobian of the deformation J is interpreted as the ratio of the undeformed volume over the deformed volume for a homogeneous deformation at a certain material point (Weiss and Gardiner, 2001). Following Holzapfel and Gasser (2001), a multiplicative decomposition of $\mathbf{F}$ into volume-changing (dilatational) and volume-preserving (isochoric) components, i.e., into volumetric ($J^{\frac{1}{3}}$ $\mathbf{I}$) and isochoric ($J^{-\frac{1}{3}} \mathbf{F}$) components (Holzapfel and Gasser, 2001; Holzapfel et al., 2000) must be performed to account for the almost incompressible nature of soft tissues (Castro et al., 2014; Safadi and Rubin, 2014). The deformation gradient (Equation 2.9) can be rewritten as (Peña et al., 2007b; Holzapfel and Gasser, 2001):

$$F = \left(J^{\frac{1}{3}} I \right) \cdot \left(J^{-\frac{1}{3}} F \right) = J^{\frac{1}{3}} \overline{F} \tag{2.9}$$

The isochoric deformation gradient $\overline{\mathbf{F}}$, such that $\det(\overline{\mathbf{F}}) = 1$, represents the purely distortional part of the deformation (Federico, 2010) defined as,

$$\overline{\mathbf{F}} = J^{-\frac{1}{3}} \cdot \mathbf{F} \tag{2.10}$$

The same multiplicative decomposition can be applied in $\mathbf{C}$ to obtain strain measures of the isochoric deformation according to the following equation (Peña et al., 2007b; Holzapfel and Gasser, 2001):

$$\mathbf{C} = \left(J^{\frac{2}{3}} \mathbf{I} \right) \cdot \left(J^{-\frac{2}{3}} \mathbf{C} \right) = J^{\frac{2}{3}} \overline{\mathbf{C}} \tag{2.11}$$

Thus, the modified right Cauchy-Green strain tensor (or deviatoric deformation tensor), which by definition does not contain any volumetric dilation (Marchesseau et al., 2010), is given by

$$\overline{\mathbf{C}} = \overline{\mathbf{F}}^T \overline{\mathbf{F}} = J^{-\frac{2}{3}} \mathbf{C} \tag{2.12}$$

with $\det(\overline{\mathbf{C}}) = 1$.

Following this procedure, the modified deformation gradient and the modified right Cauchy-Green strain tensor can be defined.

$J = 1$ is the condition for an isochoric motion (Holzapfel and Gasser, 2001), which means that the material is taken to be incompressible (Safadi and Rubin, 2014; Weiss and Gardiner, 2001).

CONSTITUTIVE MODELLING

The stress at any point of an elastic material can be defined barely as a function of the deformation gradient $\mathbf{F}$ at that point. As a consequence, a change in the stress barely occurs as a response to a modification of configuration, independently of the manner as it arises in space and time (Weiss and Gardiner, 2001). In hyperelastic materials, the above referred definition is valid, arising, in addition, a scalar function from which the stress can be calculated at each point $\mathbf{X}$. This function is the strain energy density function (SEDF), also called strain energy potential function, which is defined per unit of reference volume and denoted by W (Fallah et al., 2016; Schmidt et al., 2014; Holzapfel and

Gasser, 2001), that describes the amount of energy necessary to deform a material (Marchesseau et al., 2010; Spencer, 1970). This scalar function is defined as a function of the deformation gradient,

$$W = \tilde{W}(\mathbf{F}) \qquad (2.13)$$

The SEDF must obey two principles: (a) the *concept of material symmetry* and (b) the *principle of material frame indifference*, to ensure that the rigid body motions will not change its value (Schröder and Neff, 2003; Weiss and Gardiner, 2001). Consequently, W may be also expressed in the form,

$$W = \tilde{W}(\mathbf{C}) \qquad (2.14)$$

The second Piola-Kirchhoff stress tensor $\mathbf{\Pi}$, which is a totally material symmetric tensor, expresses the stress in relation to the reference configuration (Bonet and Wood, 1997; Sussman and Bathe, 1987) directly from the strain energy function $\tilde{W}(\mathbf{C})$ (Fallah et al., 2016; Weiss and Gardiner, 2001) in the form,

$$\mathbf{\Pi} = 2\frac{\partial W(\mathbf{C})}{\partial \mathbf{C}} \qquad (2.15)$$

Hyperelasticity provides an adequate framework to the formulation of constitutive equations for biological soft tissues because it accounts for large deformations and the anisotropy of the continuum domain (Weiss and Gardiner, 2001). Therefore, it may also be extended to other material behaviours, such as viscoelasticity (Puso and Weiss, 1998) and poroelasticity (Simon, 1992; Kwan et al., 1990).

Material symmetries will restrict the way in which the strain energy depends on $\mathbf{C}$, i.e., any orthogonal transformation that belongs to the material symmetry group will maintain the same SEDF. For isotropic hyperelastic materials, W depends on $\mathbf{C}$ (Equation 2.16) solely through three invariants (Weiss and Gardiner, 2001):

$$W = \tilde{W}(\mathbf{C}) = \tilde{W}(I_1, I_2, I_3) \qquad (2.16)$$

where I_1, I_2, I_3 are the principal invariants of $\mathbf{C}$ (Fallah et al., 2016; Weiss and Gardiner, 2001; Spencer, 1970), defined through the following equations (Feng et al., 2006):

$$I_1 = \mathbf{C} : \mathbf{1} = \text{tr}(\mathbf{C}) \tag{2.17}$$

$$I_2 = \frac{1}{2}\left(I_1^2 - \mathbf{C} : \mathbf{C}\right) = \frac{1}{2}\left[(\text{tr}\,\mathbf{C})^2 - \text{tr}(\mathbf{C}^2)\right] \tag{2.18}$$

$$I_3 = J^2 = \det(\mathbf{C}) \tag{2.19}$$

Yet, a hyperelastic material can show an anisotropic behaviour instead of an isotropic one. In that case, the SEDF depends both on $\mathbf{C}$ (i.e., the right Cauchy-Green strain tensor) and on the matrix fibres directions (Fallah et al., 2016). Tissue's behaviour is usually characterized by two families of fibres (Peña et al., 2007b) associated with two-unit vectors $\mathbf{a}_1$, $\mathbf{a}_2$ in the reference configuration (i.e., in $\mathbf{X}$), describing the local fibre directions in each point $\mathbf{X} \in \Omega_0$ (Holzapfel and Gasser, 2001). In the specific case of cartilage, $\mathbf{a}_1$ and $\mathbf{a}_2$ could characterize the orientations of two families of collagen fibres in the undeformed reference configuration (Holzapfel, 2000a). As so, W must be rewritten as a function of the invariants of $\mathbf{C}$ and two-unit vectors (Equation 2.20) in the form (Fallah et al., 2016):

$$W = \widetilde{W}(\mathbf{C}, \mathbf{a}_1, \mathbf{a}_2) \tag{2.20}$$

Therefore, following Equations 2.16 and 2.20, and according to the theorem of the invariants of $\mathbf{C}$ (Lai et al., 2009), anisotropic hyperelastic materials reinforced with two families of fibres (Peña et al., 2008; 2007b) are expressed by nine invariants $I_1, I_2, I_3, ..., I_9$ of the right Cauchy-Green strain tensor $\mathbf{C}$ (Kida and Adachi, 2015). Thus, the SEDF can be rewritten through,

$$W = \widetilde{W}(I_1, I_2, I_3, ..., I_9) \tag{2.21}$$

Following Holzapfel (2000b), the second Piola-Kirchhoff can now be obtained as follows,

$$\mathbf{\Pi} = 2\frac{\partial W(\mathbf{C})}{\partial \mathbf{C}} = 2\sum_{i=1}^{8}\frac{\partial W(\mathbf{C})}{\partial I_i}\frac{\partial I_i}{\partial \mathbf{C}} \tag{2.22}$$

The first three invariants of the right Cauchy-Green strain tensor $\mathbf{C}$ (i.e., I_1, I_2, I_3) are due to the material isotropic behaviour. The following scalars (*pseudo*-invariants $I_4,...,I_9$) arise directly from the anisotropy generated by the two families of fibres (Holzapfel, 2000b). They describe the properties of the fibre family and its interaction with the other material constituents. Usually, a transversely isotropic material reinforced by one family of fibres has a single preferred direction $\mathbf{a}_1$ at each material point, motivating the appearance of the *pseudo*-invariants I_4 and I_5 (Holzapfel, 2000b).

On the other hand, a completely anisotropic material, which is assumed to be reinforced by two families of fibres, has two main directions motivating the appearance of the invariants $I_1, I_2, I_3,...,I_9$ (Fallah et al., 2016). The invariant I_9 does not depend on the deformation, and thus, it is no longer considered in the calculation of the second Piola-Kirchhoff stress tensor $\mathbf{\Pi}$ (Equation 2.22). As referred by Holzapfel and Gasser (2001), all remaining invariants of $\mathbf{C}$ are represented below (Equations 2.23 to 2.28):

$$I_4 = \mathbf{a}_1 \cdot \mathbf{C} \cdot \mathbf{a}_1 \equiv \lambda_1^2 \tag{2.23}$$

$$I_5 = \mathbf{a}_1 \cdot \mathbf{C}^2 \cdot \mathbf{a}_1 \tag{2.24}$$

$$I_6 = \mathbf{a}_2 \cdot \mathbf{C} \cdot \mathbf{a}_2 \equiv \lambda_2^2 \tag{2.25}$$

$$I_7 = \mathbf{a}_2 \cdot \mathbf{C}^2 \cdot \mathbf{a}_2 \tag{2.26}$$

$$I_8 = \mathbf{a}_1 \cdot \mathbf{C} \cdot \mathbf{a}_2 \tag{2.27}$$

$$I_9 = (\mathbf{a}_1 \cdot \mathbf{a}_2)^2 \tag{2.28}$$

In fact, I_1 and I_2 are the main isotropic invariants of $\mathbf{C}$, because $I_3 = J^2 = 1$, regarding incompressibility condition, does not affect the free energy. The invariants I_4 and I_6 are the squares of

fibres stretches λ_i^2 (with $i = 1,2$) in the referential directions $\mathbf{a}_1$ and $\mathbf{a}_2$, respectively. (Fallah et al., 2016; Latorre et al., 2016; Holzapfel and Gasser, 2001; Holzapfel, 2000a).

Assuming the nearly incompressible condition, attention must be given to the description of isochoric deformations characterized by the energy function $\overline{W}$ (Holzapfel, 2000a; Simo and Taylor, 1991).

DECOUPLED REPRESENTATION OF THE FREE ENERGY $\overline{W}(\mathbf{C})$

It is well-known that soft tissues deformation response is almost isochoric in nature. For this reason, the strain energy density function (SEDF) for slightly compressible anisotropic materials reinforced with two families of fibres takes a decoupled representation (Equation 2.29), which describes separately the volumetric ("*vol*") and isochoric ("*isoc*") contributions (Kida and Adachi, 2015; Holzapfel and Gasser, 2001):

$$W\left(\mathbf{C},\mathbf{a}_1,\mathbf{a}_2\right) = W_{vol}\left(J\right) + W_{isoc}\left(\bar{I}_1,...,\bar{I}_9\right) \qquad (2.29)$$

where $\bar{I}_1,...,\bar{I}_9$ are the isochoric contribution of the invariants $I_1,...,I_9$, i.e., the invariants of $\overline{\mathbf{C}}$ (Equation 2.12). For later use, let $W_{vol}\left(J\right)$ and $W_{isoc}\left(\bar{I}_1,...,\bar{I}_9\right)$ be hereafter rewritten as $\overline{W}_H\left(J\right)$ and $\overline{W}\left(\overline{\mathbf{C}},\mathbf{a}_1,\mathbf{a}_2\right)$, respectively. Hence, the volumetric component will be better explained afterwards.

The SEDF adopted in this work will be represented by

$$W\left(\mathbf{C},\mathbf{a}_1,\mathbf{a}_2\right) = \overline{W}_H\left(J\right) + \overline{W}\left(\overline{\mathbf{C}},\mathbf{a}_1,\mathbf{a}_2\right) \qquad (2.30)$$

Besides, according to Holzapfel et al. (2000), the total isochoric strain energy function can be further decoupled into an isotropic and anisotropic parts. Taken from Kida and Adachi (2015), the two terms of $\overline{W}\left(\overline{\mathbf{C}},\mathbf{a}_1,\mathbf{a}_2\right)$ are given by

$$\overline{W}\left(\overline{\mathbf{C}},\mathbf{a}_1,\mathbf{a}_2\right) = \overline{W}_{iso}\left(\overline{\mathbf{C}}\right) + \overline{W}_{aniso}\left(\overline{\mathbf{C}},\mathbf{a}_1,\mathbf{a}_2\right) \qquad (2.31)$$

Concerning cartilage modelling, the most used isotropic hyperelastic constitutive model is the incompressible (i.e., $I_3 = \det(\mathbf{C}) = 1$, Fallah et al., 2016) Mooney-Rivlin given by Equation 2.32, according to Weiss and Gardiner (2001) and Mooney (1940):

$$\overline{W}_{MR}(\overline{\mathbf{C}}) = \sum_{i+j=1}^{N} C_{ij}^{MR} (\bar{I}_1 - 3)^i (\bar{I}_2 - 3)^j \qquad (2.32)$$

If $N = 1$, there are only two constitutive parameters C_{10}^{MR}, C_{01}^{MR} (both in MPa) and Equation 2.32 turns

$$\overline{W}_{MR}(\overline{\mathbf{C}}) = C_{10}^{MR} (\bar{I}_1 - 3) + C_{01}^{MR} (\bar{I}_2 - 3) \qquad (2.33)$$

When highly loaded, collagen fibres become straighter increasing the resistance to stretch (i.e., the tissue becomes stiffer). Hence, the energy stored is then governed by the Holzapfel law (Equation 2.34), which is applied for the anisotropic contribution of the collagenous family fibres, according to Latorre et al. (2016), Kim et al. (2012), and Seifzadeh et al. (2011):

$$\overline{W}_{aniso} = \frac{k_1}{2k_2} \sum_{i=4,6} \left[e^{k_2 (\bar{I}_i - 1)^2} - 1 \right] \qquad (2.34)$$

In a general Holzapfel model, N is the number of families of fibres (usually $N \leq 3$) (Seifzadeh et al., 2011). Moreover, $k_1 > 0$ is a stress-like material parameter (in MPa) and $k_2 > 0$ a dimensionless material parameter (Kim et al., 2012; Vena et al., 2005). It must be highlighted that these invariants depend on the directions of the collagen fibres, as suggested by Equations 2.23 and 2.25. The contribution of the remaining scalar *pseudo*-invariants has been considered negligible (Latorre et al., 2016).

MIXED DISPLACEMENT-PRESSURE FORMULATION

The process of defining constitutive equations in the field of nearly incompressible hyperelasticity is simplified by including a volumetric energy component $U(J)$. We shall recall the Equation 2.30, in

which $\overline{W}_H(J)$ is the *stored energy function* (Equation 2.35) that contains the volumetric part $U(J)$ (Brink and Stein, 1996):

$$\overline{W}_H(J) = kU(J) \tag{2.35}$$

In Equation 2.35, k is a penalty parameter playing the role of material's bulk modulus, which is independent of deformation (Brink and Stein, 1996) and it must be several orders of magnitude higher than the shear modulus (Alves et al., 2010; Sussman and Bathe, 1987). One should notice that when $k \rightarrow +\infty$ any volumetric change is strongly penalized, and the formulation approaches the total incompressibility condition (Kida and Adachi, 2015; Alves et al., 2010). According to Brink and Stein (1996), $U(J)$ must be equal to one of the following Equations (2.36 to 2.38):

$$U(J) = \frac{1}{2}(J-1)^2 \tag{2.36}$$

$$U(J) = \frac{1}{2}(\ln J)^2 \tag{2.37}$$

$$U(J) = \frac{1}{4}(J^2-1) - \frac{1}{2}(\ln J) \tag{2.38}$$

Safadi and Rubin (2014) pointed out that U is a strictly convex function and has a minimum at $J = 1$. U must be specified following the restrictions (Equations 2.39 to 2.41):

$$U(1) = 0 \tag{2.39}$$

$$\frac{\partial U(J)}{\partial J}(1) = 0 \tag{2.40}$$

$$\frac{\partial^2 U(J)}{\partial J^2}(1) = 1 \tag{2.41}$$

Therefore, the volumetric function $U(J)$ is most often represented as shown in Equation 2.36, e.g., for arterial walls (Gasser et al., 2006), intervertebral discs (Castro et al., 2014), and general rubber-like materials (Chang et al., 1991; van den Bogert et al., 1991). Thus, $\overline{W}_H(J)$ turns into,

$$\overline{W}_H(J) = \frac{k}{2}(J-1)^2 \tag{2.42}$$

The mathematical contribution of k to the second Piola-Kirchhoff stress tensor can be easily explained starting from the derivative of the volumetric strain energy function $\overline{W}_H(J)$ through,

$$\frac{\partial \overline{W}_H(J)}{\partial \mathbf{C}} = \frac{\partial \overline{W}_H(J)}{\partial J} \frac{\partial J}{\partial \mathbf{C}} \tag{2.43}$$

We shall also require the following standard results (Equations 2.44 to 2.45) to assess the value of the previous expression (Equation 2.43) (Kida and Adachi, 2015; Gasser et al., 2006; Brink and Stein, 1996):

$$\frac{\partial \overline{W}_H(J)}{\partial J} = \frac{\partial k U(J)}{\partial J} = k(J-1) \tag{2.44}$$

$$\frac{\partial J}{\partial \mathbf{C}} = \frac{1}{2} J \, \mathbf{C}^{-1} \tag{2.45}$$

The quantity $\overline{p}$ expressed through Equation 2.46 denotes the hydrostatic pressure of the Cauchy stress tensor that is simply the negative of the hydrostatic stress expressed in Equation 2.44 (Federico, 2010). So, according to Lukeš and Rohan (2010) and Sussman and Bathe (1987), we have

$$\overline{p} = -\frac{\partial \overline{W}_H(J)}{\partial J} = -k(J-1) \tag{2.46}$$

Further, the second Piola-Kirchhoff stress tensor $\mathbf{\Pi}$ can be rewritten as a sum of purely volumetric $\mathbf{\Pi}^{s,vol}$ and purely isochoric $\mathbf{\Pi}^{s,isoc}$ (solid) parts (Kida and Adachi, 2015; Peña, 2014; Holzapfel and Gasser, 2001; Brink and Stein, 1996) as follows,

$$\mathbf{\Pi} = \mathbf{\Pi}^{s,vol} + \mathbf{\Pi}^{s,isoc} = 2\frac{\partial \overline{W}_H(J)}{\partial \mathbf{C}} + 2\frac{\overline{W}(\mathbf{C})}{\partial \mathbf{C}} \tag{2.47}$$

Combining Equations 2.43 to 2.47, the second Piola-Kirchhoff stress tensor $\mathbf{\Pi}$ is fully defined as,

$$\mathbf{\Pi} = 2\frac{\partial \overline{W}(\mathbf{C})}{\partial \mathbf{C}} + k\,J\,(J-1)\,\mathbf{C}^{-1} = 2\frac{\partial \overline{W}(\mathbf{C})}{\partial \mathbf{C}} - \overline{p}\,J\,\mathbf{C}^{-1} \tag{2.48}$$

BIPHASIC DESCRIPTION

Cartilage present an incompressible porous-permeable solid matrix hydrated with an incompressible interstitial fluid (water) (Spilker and Suh, 1990; Mow et al., 1980). Consequently, biphasic formulations intend to include non-linearities associated with an eventual strain-dependent permeability. The pores are considered sufficiently small to study the material as continuous and homogeneous (Thibbotuwawa et al., 2015).

At a macroscopic point of view, biphasic soft tissues are easily characterized by their initial solid s and fluid f volume fractions n_α, with $\alpha = \{s, f\}$ and $n_s + n_f = 1$ (Castro et al., 2014; Spilker and Suh, 1990). The water moves freely throughout the whole matrix depending on the applied deformation and internal friction, which in turn depends on tissue permeability (Thibbotuwawa et al., 2015; Guo et al., 2014; Maas et al., 2011).

A permeability function, as the Darcy's law, is one of the most straightforward way of modelling the fluid transient response (Castro et al., 2014; Marchesseau et al., 2010; Wilson et al., 2005b; Huyghe et al., 1991). Therefore, the total Cauchy stress tensor $\mathbf{\sigma}^{total}$ results from the contribution of both solid $\mathbf{\sigma}^s$ and fluid $\mathbf{\sigma}^f$ parts (Huyghe et al., 1991), as given by

$$\mathbf{\sigma}^{total} = \mathbf{\sigma}^s + \mathbf{\sigma}^f \tag{2.49}$$

Considering that p^f is the fluid (or pore) pressure, in a standard biphasic theory the total Cauchy stress can be rewritten as follows (Huyghe et al., 1991):

$$\mathbf{\sigma}^{total} = \mathbf{\sigma}^s - p^f \mathbf{I} \tag{2.50}$$

where $\boldsymbol{\sigma}^s$ is the *effective* solid stress tensor (Wilson et al., 2005b; Huyghe et al., 1991). The second Piola-Kirchhoff stress tensor $\boldsymbol{\Pi}$ must be, once again, rewritten as follows,

$$\boldsymbol{\Pi}^{total} = \boldsymbol{\Pi}^s + \boldsymbol{\Pi}^f \tag{2.51}$$

in which $\boldsymbol{\Pi}^f$ is given by

$$\boldsymbol{\Pi}^f = -p^f J \, \mathbf{C}^{-1} \tag{2.52}$$

In a biphasic swelling formulation, previous equations account for Donnan osmotic effect that causes tissue swelling (Wilson et al., 2005b). In this case, the osmotic pressure must be included in Equation 2.50 and the total Cauchy stress is expressed as follows (Castro et al., 2014; Wilson et al., 2005b):

$$\boldsymbol{\sigma}^{total} = \boldsymbol{\sigma}^s - \left(\mu^f + \Delta\pi\right)\mathbf{I} \tag{2.53}$$

in which $p^f = \mu^f + \Delta\pi$ (μ^f is the water chemical potential and $\Delta\pi$ is the osmotic pressure gradient) (Wilson et al., 2005b).

However, in this work, only a standard biphasic formulation will be implemented, otherwise a triphasic (Lai et al., 1991) or quadriphasic (van Loon et al., 2003; Frijns et al., 1997) law would have to be impregnated. In a standard biphasic formulation, the physiological fluid exudation and imbibition are not the focus of the investigation. When the system reaches the equilibrium (and it does very fast), ion flux is much higher than the fluid flow and the osmotic pressure gradient vanishes:

$$\begin{aligned}\boldsymbol{\sigma}^{total} &= \boldsymbol{\sigma}^s - \left(\mu^f + \Delta\pi\right)\mathbf{I} = \\ &= \boldsymbol{\sigma}^s - \mu^f \, \mathbf{I} - \Delta\pi \, \mathbf{I} = \\ &= \boldsymbol{\sigma}^s - \mu^f \, \mathbf{I} \end{aligned} \tag{2.54}$$

Hence, the pore pressure p^f is replaced by the electrochemical potential μ^f, which is a water constant (Wilson et al., 2005b).

DEFORMATION-DEPENDENT PERMEABILITY

In a standard biphasic model, a strain-dependent permeability law could help describing more accurately the visco-hyperelastic behaviour of the cartilage.

Darcy's law (Equation 2.55) pointed out that the flux of the fluid $\mathbf{w}$ is proportional to local pressure gradient (Castro et al., 2014; Maas et al., 2011; Noailly et al., 2008):

$$\mathbf{w} = -\mathbf{K} \cdot \nabla p^f \tag{2.55}$$

where $\mathbf{K}$ is the hydraulic permeability tensor (Quinn et al., 2001), usually defined as $\mathbf{K} = k(J)\mathbf{I}$, i.e., as a function of the deformation, and ∇p^f is the fluid (or pore) pressure gradient. The term $k(J)$ (Equation 2.56) depends directly on the initial permeability k_0 (Guo et al., 2015; Castro et al., 2014):

$$k(J) = k_0 J^M \tag{2.56}$$

in which J represent the relation between current and initial void ratios (ratio of volume of pores to volume of solid) (Thibbotuwawa et al., 2015; Weiss and Gardiner, 2001).

LONG-TERM VISCOELASTICITY

The ability to mimic the viscoelastic behaviour is accomplished by adding to the hyperelastic stress tensor some time-dependent stresses based on Prony series (Marchesseau et al., 2010), whose parameters are estimated experimentally. Hence, the second Piola-Kirchhoff stress tensor $\mathbf{\Pi}$ can be written (Maas et al., 2011) as follows,

$$\mathbf{\Pi}(t) = \int_0^t R(t-s)\frac{d\,\mathbf{\Pi}^e}{ds}\,ds \tag{2.57}$$

where $\mathbf{\Pi}^e$ is the elastic stress tensor and $R(t)$ is the relaxation function defined through Equation 1.12. With this expression, the total stress is given by (Maas et al., 2011):

$$\mathbf{\Pi}(t) = \int_0^t \left(K_0 + \sum_{i=1}^N \left[K_i \exp\left(-\frac{t+s}{\tau_i} \right) \right] \frac{d\,\mathbf{\Pi}^e}{ds} \right) ds \qquad (2.58)$$

The introduction of the variable $\mathbf{H}_k$ in Equation 2.58 allows writing the total stress (Maas et al., 2011) as follows,

$$\mathbf{\Pi}(t) = K_0 \mathbf{\Pi}^e(t) + \sum_{i=1}^N \left[K_i \mathbf{H}_k(t) \right] \qquad (2.59)$$

The long-term viscoelastic effects must be revised to each specific behaviour (creep or stress-relaxation). The adjustments of each equation should be made accordingly.

2.4.2 CT Imaging Acquisition

The geometry acquisition of the human nasal structures (namely bones, cartilage, smooth muscles, and other soft tissues) is fundamental to construct a 3D FE model. Usually, medical images are obtained from X-Ray, CT, and MRI (Weiss et al., 2005; Hawkes et al., 2004). Li et al. (1999) and Gardiner and Weiss (2003) have used MRI and CT, respectively, to perform their imaging segmentation. The CT-scans used in this work were obtained from Luz Arrábida Hospital, in Vila Nova de Gaia. The information was yielded in accordance with national legal regulations, ethical concerns, and patient's consent for research purposes.

When compared to MRI, CT has also high spatial resolution and signal-to-noise ratio (Fripp et al., 2010). Furthermore, it provides clear images of soft structures and bones, which are often included in FEM to represent cartilage wrapping. Although soft tissues are detectable in standard CT images, little differences are noticed when those images are segmented (radiodensity signals), which renders difficult to distinguish complex geometrical details or certain boundaries (for instance, between cartilage and subcutaneous tissue layers). Indeed, these tissues have similar densities, which makes 3D reconstruction sometimes user-dependent.

A 21-year-old female volunteer's head was imaged in Head First Supine (HFS), using a CT apparatus (CTAWP 77722, SOMATOM Perspective, Siemens®) in clockwise direction. According to this designation, "Head First" is defined as the patient's head being positioned toward the front of the equipment; "Supine" is defined as the patient's face in an upward direction. The software used in the

acquisition process was the syngo CT VC30, version easyIQ. The following settings were applied: kilovoltage Peak = 110 kV; Distance source-detector = 976.1 mm; Distance source-patient = 535 mm; Slice thickness = 1.5 mm; Acquisition matrix size = 512 mm; Pixel size = 0.5 mm (Huda and Slone, 2003).

2.4.3   Segmentation and 3D Geometry Reconstruction

Prior to model construction, it is necessary to undergo the partitioning of the digital images (of the nose region) into multiple segments (image segmentation) to clearly define the image boundaries. In this work, an open-source software from 3D Slicer® was used to provide the 3D construction from multi-modality imaging (CT-scans).

Nasal bones, cartilages, and general soft tissues were segmented using 3D Slicer v4.6.2 (http://www.slicer.org/). Axial, coronal, and sagittal directions were considered in this process. A manual cropping followed by a semi-automated segmentation assisted by manual thresholding was performed. The most useful software modules were *volume rendering*, *volume cropping*, and *segmentation editor*. The first module required building a prototype model after DICOM images loading has been done. Then, *volume cropping* created a 3D box, in which the prototype was centred, and allowed the adjustment of spatial limits imposed by six plans (L and R, S and I, A and P) until the regions of interest (ROI) had been defined inside the (virtual) box. Cropping was also essential to remove noisy voxels near the borders of the box (Öztürk et al., 2016). Finally, the *segmentation editor* allowed to create a finite number of labels that clearly identified each anatomic structure (e.g., bones, cartilage, etc..), regarding the definition of specific thresholds (Hounsfield units – HU – or radiodensity units). The final volume was created by selecting and merging previous segmented labels.

Each voxel was assigned to only one domain (Fedorov et al., 2012). Each domain was denuded from all the neighbouring regions, by means of a pre-processing tool (CT-Bone or CT-Soft tissue, respectively), increasing the reliableness of the segmentation process (Öztürk et al., 2016). To give an example, bone segmentation was made with a CT-Bone pre-processing step, which means that soft tissues were previously removed (Figure 31).

Afterwards, the bone geometry was segmented using a minimum threshold close to +350 HU, similar to the technique adopted by Willing et al. (2013). Final osseous model was then build up using the *model effect* tool (Figure 31).

(a)   **(b)**   **(c)**
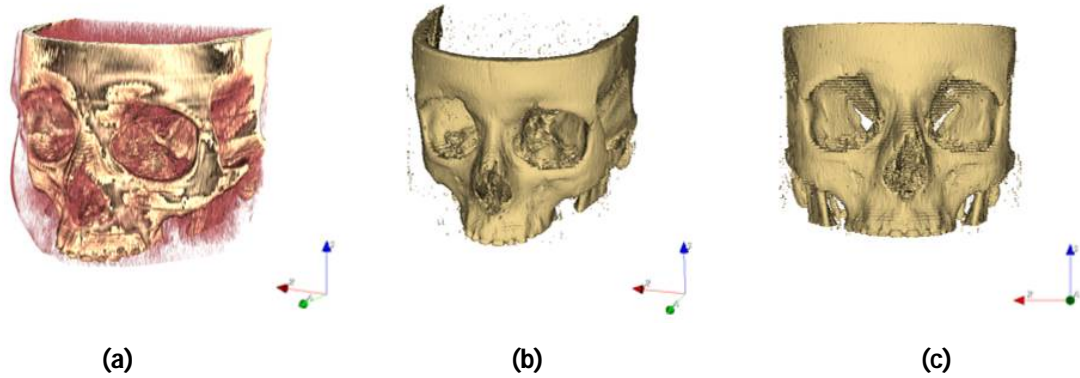
Figure 31: Pre-processing tool CT-Bone: **(a)** Original mapping; **(b)** Removal of soft tissues; **(c)** Semi-automated segmentation with manual thresholding of the osseous (more compact) regions.

The referred procedure has also been executed for cartilage segmentation, with a threshold ranging from approximately -430 to +690 HU (Figure 32).

(a)   **(b)**   **(c)**
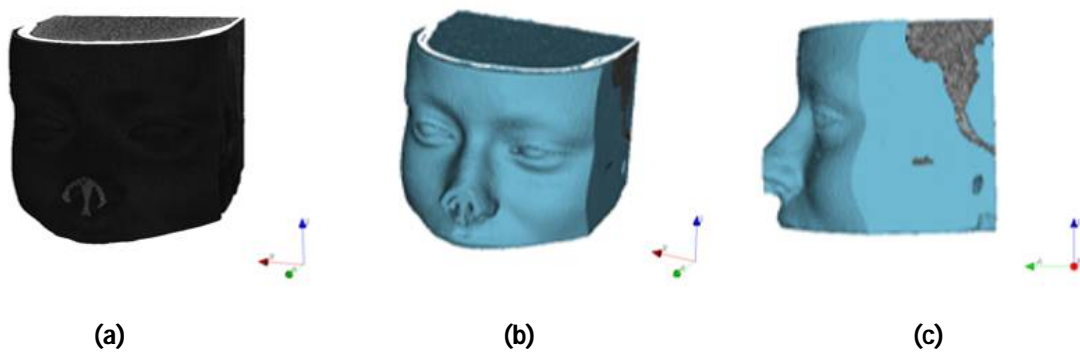
Figure 32: Pre-processing tool CT-Soft tissue: **(a)** Original mapping; **(b)** Removal of osseous components; **(c)** Semi-automated segmentation with manual thresholding of the soft regions.

The geometry of the human nose was obtained by combining both solid models (i.e., bone and cartilage) (Figure 33).

The referred solid modelling strategy has led to a STL format file, which barely enabled obtaining surface entities (triangular) when edited in a solid modelling CAD system platform (like SolidWorks®). A similar outcome has occurred once imported in a CAE software that incorporates a general-purpose FE mesh generator (like ABAQUS® CAE).
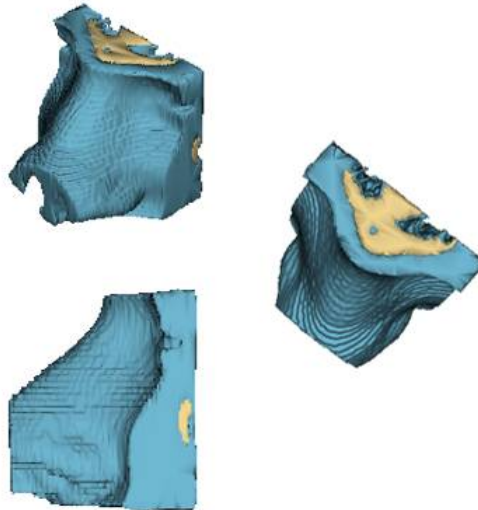
Figure 33: *Merging volumes.* Representation of the final human nose geometry.

2.4.4 FE Mesh Generation

To create a FE mesh from the STL files, a C# converter was developed. The main program was divided into three steps: (a) STL files reader creation; (b) Data conversion; And (c) OBJ files exporting.

The class "STL reader" implements a routine to read the STL format files (input), whose data is registered in binary format. Then, a stream reader ("Binary reader") is initialized to interpret the data (data flux in memory).

The process begins with the identification (ID) of mesh points that belong to the surface of the input data (vertices). During this step, a class lists the points according to their ID avoiding repetitions. Normal vectors of each triangle are then calculated in each vertex. These vectors result from the sum of the normal vectors of the triangles that actually share the same vertex. Thus, a new class builds a list of normal vectors registering their ID.

The class "Triangle" builds individual triangular facets. Each facet is associated with 1 triangle ID, 1 normal vector ID, and 3 vertices ID. The class responsible for listing the triangles is also responsible for counting their number within the mesh and to prevent distortion of the finite elements. The lists of points, normal vectors, and triangles are then associated to ensure the connectivity of each finite element. The mesh is exported in OBJ format, from which the data concerning the vertices (prefix, *v*), normal vectors (prefix, *vn*), and triangles can be accessed (consulted). Figure 34 shows the obtained FE mesh.

(a)   **(b)**
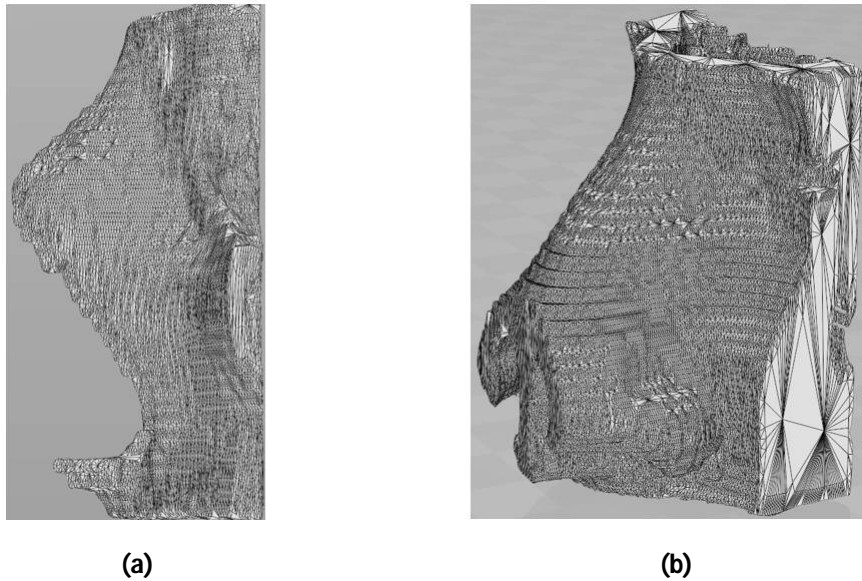
Figure 34: FE mesh of **(a)** nasal bones and **(b)** neighbourhood regions composing of soft tissues.

2.4.5   Model Development

Medical image resolution, which is determined by pixel size and slice thickness, is paramount for 3D geometric reconstruction (Tyndyk et al., 2007; Li and Wang, 2006). Indeed, the resolution is directly proportional to the quality of the FE mesh, i.e., the higher the resolution, the more accurate is the mesh (Kelm et al., 2012). To our knowledge, in high-resolution CT-scans, a narrow slice thickness usually between 1-2 mm is used, the pixel size is minimized, and the spatial resolution (capability to differentiate two structures) is maximized (Yeh et al., 2014; Yin et al., 2010; Li and Wang, 2006). The resolution of CT-scans used in this work was in the range of typical values, so no issues are expected from that.

2.4.6   Numerical Simulations on the Long-term Viscoelasticity

The constitutive laws were briefly described in section 2.4.1. They were chosen from the equations implemented in V-Biomech, a home-made FE solver produced by Alves et al. (2010). V-Biomech is a FEA code dedicated to numerical simulation of incompressible hyper-viscoelastic materials that comprises some of the most relevant biomechanical features, such as general isotropic (Mooney-Rivlin, Ogden) and anisotropic (Holzapfel, Poly-convex) hyperelastic laws, short- and long-term viscoelastic effects (hysteresis, stress rate effects, creep, and stress-relaxation), among others (Alves et al., 2010). V-Biomech has revealed good results in previous simulations in the field of intervertebral discs (Castro et al., 2014). Hence, the purpose is to re-define some features to build a human nasal pyramid constitutive model.

Creep and stress-relaxation tests were modelled on the regular region of the *dog-bone* specimen configuration (with constant cross-section area) shown in Figure 25. Hence, a FE mesh (Figure 35) was generated with the dimensions of that specimen after discretization of the model in second-order hexahedral Lagrangian finite elements, with 27 nodes.
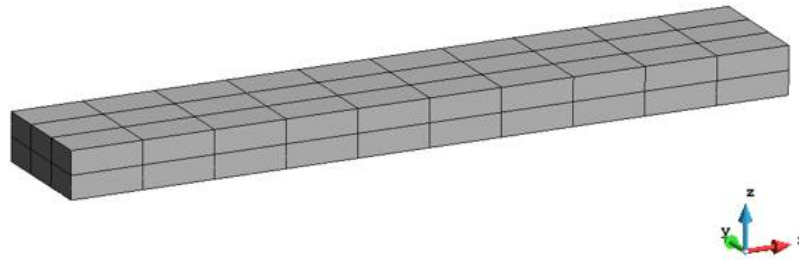
Figure 35: FE mesh of a nasoseptal cartilage sample (10.0x1.738x0.656 mm³). Specimen #1 of human donor #1.

2.4.7 Material Parameters

This section intends to enunciate the reference values of the constitutive parameters presented in section 2.4.1. The solid matrix is considered to be isotropic (Mooney-Rivlin, Equation 2.33) and permeable, taking into account a deformation-dependent permeability equation based on Darcy's law (Equation 2.55). The collagen meshwork, assumed to have two major family fibres, is governed by an anisotropic constitutive law (Holzapfel, Equation 2.34), and the selected viscoelastic models are the Kelvin-Voigt (Equation 1.9) and Maxwell (Equation 1.12) for creep and stress-relaxation, respectively (section 1.6.2).

Concerning those characteristics, material constitutive parameters are presented in Table 3, whose parameters have been subdivided in two groups. Firstly, isotropic, anisotropic, and permeability reference values (Mooney-Rivlin, Holzapfel constitutive values, and positive permeability constants) were based on multiple literature sources; Secondly, time-dependent viscoelastic parameters were determined by fitting Kelvin-Voigt and Maxwell models to the obtained experimental data, isolating the transient responses of human nasoseptal cartilages in creep and stress-relaxation.

Table 3: Material properties of human nasoseptal cartilages. Multiple data sources were assessed as stated on each entry of the table. Time-dependent viscoelastic parameters are not presented.

Constitutive parameters		Reference values	Source (in Obs.)
Isotropy	C_{10}^{MR} [MPa]	1.00	I
	C_{01}^{MR} [MPa]	0.00	I
Anisotropy	k_1 [MPa]	0.47	II
	k_2	1.50	II
Permeability	k_0 [m^4.N^{-1}.s^{-1}]	1.99E-15	III
	M	7.1	IV

Obs.: (I) Mooney-Rivlin material parameters of the cartilaginous endplate of intervertebral discs (Castro et al., 2014): (II) Holzapfel material parameters of the superficial layer of articular cartilage (Cortez et al., 2016); (III) Constant permeability found for human menisci and close to that of the human femoral cartilage (Mononen et al., 2012; Joshi et al., 1995); Positive constant found for bovine patellar cartilage (Wilson et al., 2004).

CHAPTER 3

Results and Discussion

Chapter three is divided in three foremost sections, in which results and discussion of the experimental and numerical contents are presented. In subchapters 3.1 and 3.2, experimental results from uniaxial tensile tests, DMA (multi-frequency tension and compression, creep-recovery, and stress-relaxation), STA (weight loss), and DSC (glass transitions) are shown, explained, and compared with benchmark literature. Rheological viscoelastic models (general Kelvin-Voigt and Maxwell) are fitted to experimental data in order to provide physical springs and dashpots meanings. Subchapter 3.3 includes the results of V-Biomech numerical simulations to determine the intrinsic constitutive parameters of the nasoseptal cartilages both in creep-recovery and stress-relaxation.

3. RESULTS AND DISCUSSION

This chapter is divided in three main sections, in which both porcine and human experimental results are presented and compared with benchmark literature. Then, the parametric values of creep-recovery and stress-relaxation experimental behaviours are assessed through numerical simulations in the case of human cartilaginous septum.

3.1 Porcine Experimental Results

This subchapter includes DSC, TGA, and DMA results of the porcine auricular cartilages (PAC), as well as quasi-static uniaxial tensile tests. The referred tests have been performed in porcine samples (a commonly used animal model for auricular tissue engineering (Griffin et al., 2016)) as to develop a comprehensive testing protocol to be employed in the mechanical characterization of human cartilages. The viscoelastic characterization of nasal cartilages is the main issue of this work.

3.1.1 Uniaxial Tensile Tests

The quasi-static mechanical behaviour of auricular cartilages has shown to be highly anisotropic reflecting the complex collagen fibre kinematics.

Figures 36a and 36b exhibit a porcine outer ear and the sites (and orientation) from which the *dog-bone*-shaped specimens (Figures 25 and 26) have been harvested (inter wrinkles region of the scapha). Prior to specimen cutting (Figure 25), the cartilage of the external ear was unfolded by promoting the removal of skin and large parts of subcutaneous tissue. Following the cutting operation, the specimens' extremities were simply wrapped with sandpaper to prevent slipping in the loading grips.

Figure 36c shows the stress-strain curves (true values) obtained under quasi-static tensile loading (0.3 mm/min) at room temperature (21 ºC), under quasi-dehydrated conditions, i.e., without use of saline solutions, and using a load cell of 250 N.

Table 4 resumes the Young's modulus (E), the UTS (σ^{ul}), and the failure strain (ε^{ul}) for the set of specimens shown in Figure 36b.
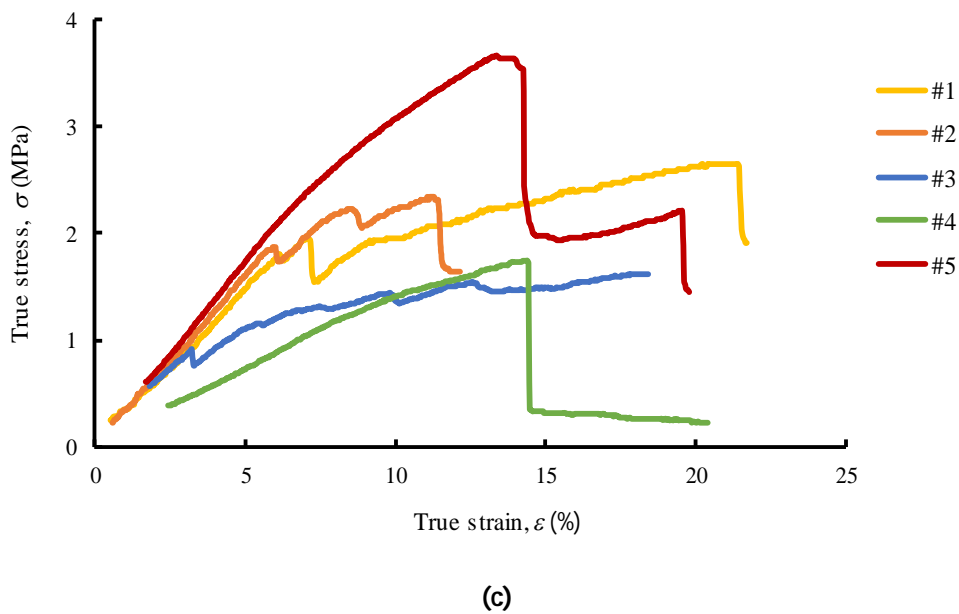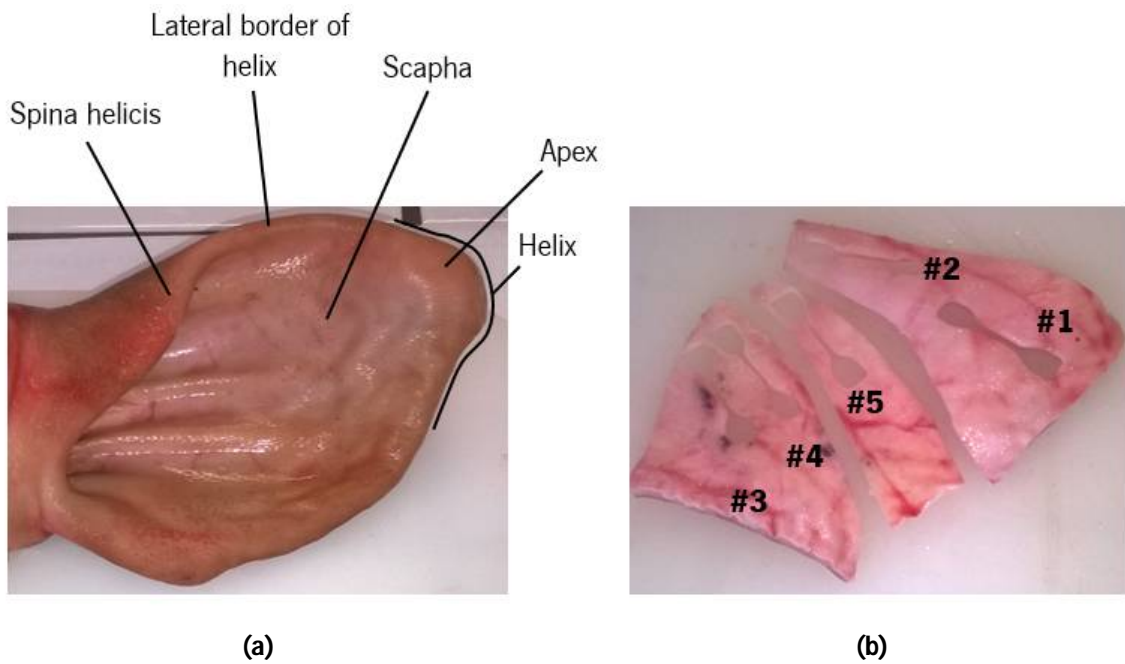
Figure 36: (a) Porcine outer ear; (b) Specimen mapping following the harvesting operation; (c) Stress-strain curves (true values) at room temperature (21 ºC).

As it was mentioned above, Table 4 resumes the values of E, σ^{ut}, and ε^{ut} for each porcine auricular specimen (1 to 5), as well as the values of the Coefficient of Variance (CoV) that was calculated through the ratio of the standard deviation to the mean (in percentage).

Table 4: Young's modulus (E), UTS (σ^{ut}), and failure strain (ε^{ut}) (true values) of porcine auricular cartilages (PAC) obtained under quasi-static loading (cross-head speed: 0.3 mm/min).

Specimen name #Test no.	E (MPa)	σ^{ut} (MPa)	ε^{ut} (%)
PAC #1	0.28	2.61	21.43
PAC #2	0.30	2.25	11.41
PAC #3	0.26	1.62	18.39
PAC #4	0.15	1.74	14.40
PAC #5	0.35	3.63	14.23
Avg. (CoV)	0.27 (28%)	2.37 (34%)	15.97 (25%)

The plotted stress-strain curves (Figure 36c) are the result of different phenomena that occur within the cartilage matrix (Gauvin et al., 2011). These are attributed to gradual recruitment of collagen fibres and their increasing role in the load bearing matrix capability. In the initial region (toe-region), the transmission of tensile forces is mainly assured by the molecules of elastin. Hence, the tissue appears to be fairly compliant in nature and no significant differences are observed in this range. For this reason, those small deformation transition zones are not shown in Figure 36c. With the increasing extension, more collagen fibres become aligned and stretched, and others recruited and reoriented into the loading direction. The consequence of this phenomenon is an increase of soft tissue stiffness until the effective volume fraction of collagen fibres becomes straightened, after which the tissue exhibits its maximum strain (and UTS) (Anssari-Benam et al., 2011a). Figure 36b allows establishing a correlation between the results of Table 4 with the position and orientation of the specimens in the porcine ear (as performed by Novitskaya et al., 2014).

The fact that specimen #5 presents the highest values both for the Young's modulus (0.35 MPa) and UTS (3.63 MPa) might be due to more equilibrated composition of cartilage and subcutaneous tissue in this specimen (i.e., 51.5% versus 48.5%, as shown in Table 1) and the circumstance that it has been harvested from the central region of the ear.

Specimens #3 and #4 are the ones that exhibit smaller values for the Young's modulus (avg. 0.21 MPa) and UTS (avg. 1.68 MPa), which have been harvested from the interior scapha (Figure 36b). Moreover, they were the fattiest specimens with higher contents of subcutaneous tissues (i.e., 58.0% and 58.8%, respectively, as shown in Table 1) that may contribute for the lower resistance to tension and relative higher failure strain.

Specimens #1 and #2 (from the apex) presented consistent results considering the Young's modulus and UTS of 0.29 MPa (avg.) and 2.43 MPa (avg.), respectively. However, specimen #1 was stretched much longer than specimen #2 till failure (21.43%), which may be justified by differences in the microstructure of the ear from the inner to most peripheral regions.

The short decreases in force that occurred earlier than that of the maximum (Figure 36c) could be explained by the different internal specimen's composition (also different subcutaneous percentage and disposition over the surface). In a first analysis, one could expect that those force decays were the result of slippage due to lack of sufficient surface gripping friction. However, in all tests, the decrease repeatedly occurred within the same stress range, implying that it was caused by the effective material behaviour, perhaps due to continuous fibre recruitment and straightening to compensate the occurrence of some micro failures. Indeed, a similar phenomenon has been reported by Teng et al. (2009) when testing some other multi-layered collagenous tissues, such as carotid arteries, in which the sudden decrease in stress has been attributed to failure of the media layer prior to adventia. In this study, two major load bearing layers (cartilage and subcutaneous tissue) can obviously interfered with the results because one of the layers is likely to fail first at lower stresses (Anssari-Benam et al., 2011a).

3.1.2 DSC Measurements

This analysis was performed with samples extracted very close to the ones that have been used in quasi-static tensile tests (section 3.1.1; Table 1). The biological materials were prepared as to enable isolating "pure" cartilage and subcutaneous tissue from the porcine external ear. Additionally, a mixture of the referred biological structures (cartilage and subcutaneous tissue), herewith designated as *composite*, was also prepared from the same samples. The adopted experimental protocol follows the description in section 2.3.3.

DSC curves were obtained plotting heat flow (D) against temperature (T) (Figures 37a-c) for specimen #4 to reveal the detectable energetic transformations that occur within the studied interval of temperatures. According to the issued analysis, two peaks have been systematically detected for cartilage, composite, and subcutaneous tissue samples, and clear differences have been detected in terms of their amplitudes: (a) the first one in the vicinity of 100 ºC and (b) the second one for a temperature higher than 200 ºC (signalized with an arrow in Figures 37a-c). Table 5 resumes the results of each temperature peak and corresponding enthalpy values.
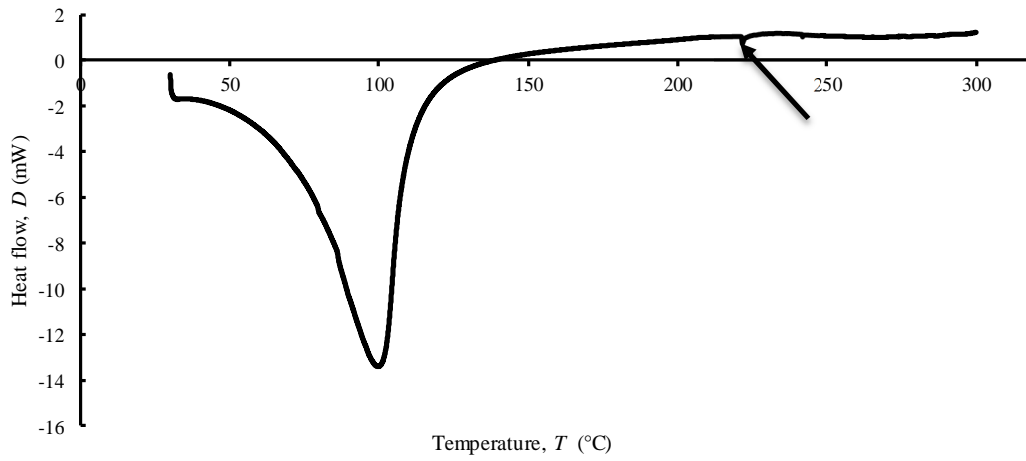
(a)
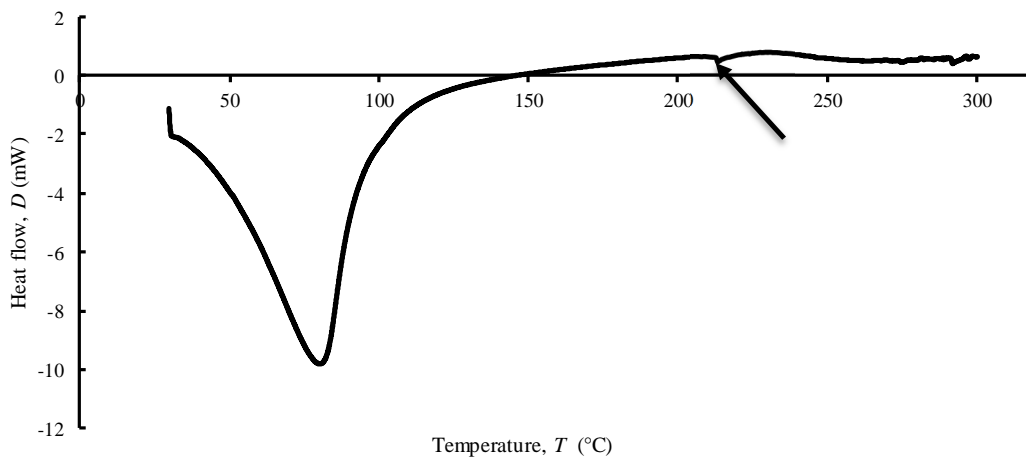
(b)
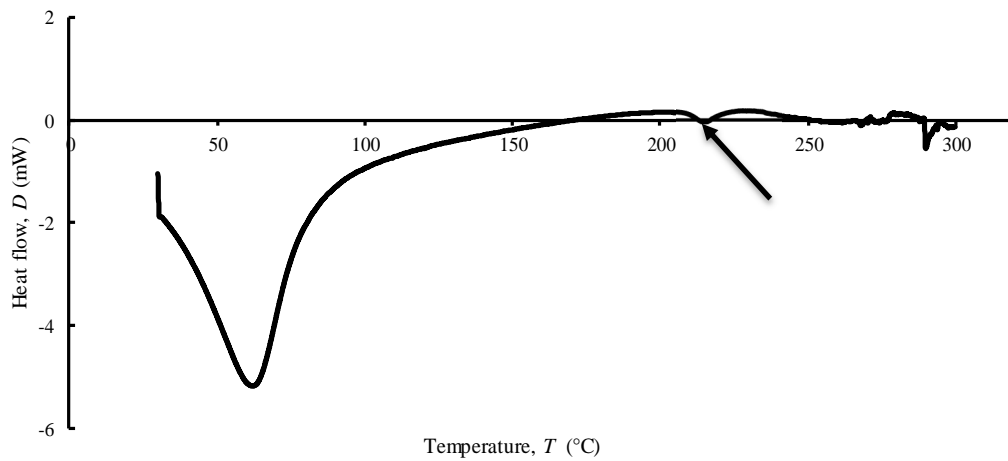
(c)

Figure 37: DSC analyses of the porcine external ear cartilage (specimen #4): **(a)** Cartilage; **(b)** Composite; **(c)** Subcutaneous tissue.

Table 5: Main thermal features (DSC) of the porcine external ear specimens. Values in parentheses represent the coefficient of variance.

Specimen ID and biological structure		1st peak		2nd peak	
		T (ºC)	ΔH (J/g)	T (ºC)	ΔH (J/g)
PAC #1	Cartilage	122.6	1150.7	208.9	0.5
	Composite	117.0	1047.5	209.3	4.1
	Subcutaneous	113.5	1198.5		
PAC #2	Cartilage	111.1	533.4	180.6	1.8
	Composite	120.4	427.8	190.7	2.5
	Subcutaneous	95.6	217.6	221.1	0.6
PAC #3	Cartilage	64.0	290.9	223.6	0.2
	Composite	78.1	500.6		
	Subcutaneous	90.5	871.4		
PAC #4	Cartilage	99.9	1058.6	221.7	0.9
	Composite	80.6	707.2	213.2	1.0
	Subcutaneous	62.0	359.3	215.2	5.8

Avg. (CoV)	Cartilage	99 (26%)	758 (55%)	209 (10%)	0.9 (82%)
	Composite	99 (23%)	671 (41%)	204 (6%)	2.5 (61%)
	Subcutaneous	90 (24%)	662 (69%)	218 (- -)	3.2 (- -)

The first energetic transformation (i.e., at 99 ºC for cartilage and composite, and 90 ºC for subcutaneous tissue, on average) is triggered by the abandon of free water from the referred biological structures. The noticed difference of 9 ºC (on average) that has been measured for cartilage and composite relatively to the subcutaneous tissue is likely related to the fatty nature of the latter structure, which makes the link of water molecules less resistant than in remaining tissues (probably at the periphery of the oily groups). The consequence of this is that the energy required to promote the water outbound in subcutaneous tissue is inferior of that necessary to trigger such phenomenon in the others. This observation is further corroborated by the observation of the measured enthalpies, which were found lower in subcutaneous tissue (662 J/g) than in cartilage (758 J/g) and composite (671 J/g) (on average).

The second energetic transformation reveals glass transition temperatures marginally higher than 200 ºC (i.e., 209 ºC for cartilage, 204 ºC for composite, and 218 ºC for subcutaneous tissue, on

average). This manifestation is probably due to release of water that was strongly linked to the collagen in these tissues (i.e., the analyzed biological structures). Indeed, it is well-known that water in collagen forms a large-scale lubrication layer mediating collagen self-assembly (Ravikumar and Hwang, 2008). The measured enthalpies were very small (i.e., 0.9 J/g for cartilage, 2.5 J/g for composite, and 3.2 J/g for subcutaneous tissue, on average) at those temperatures. The referred values of T_g must be confirmed throughout DMA, as it will be performed in section 3.1.4.

3.1.3 TGA Measurements

Thermogravimetric analysis (TGA) was executed using samples that have been prepared according to the same procedures as for the DSC (i.e., cartilage, composite, and subcutaneous tissue). The experimental methods follow the description in section 2.3.4.

Smooth TGA curves were obtained for each biological structure (Figures 38a-c), showing the evolution of the weight loss (WL) of the analysed samples over the temperature (T) within the interval 30-500 ℃. The registered weight losses occurred three times per biological structure, as represented in Figure 38a through the events WL_1, WL_2, and WL_3, in phase with the plotted peaks given by the first derivative of the TG curve (DTG curve). The DTG curve is useful to determine the inflection points on the TG curve. Onset and endset temperatures (pairs of small squares in Figure 38a) have been used to calculate the weight loss per thermal degradation (T_{pi}, with $i = 1,2,3$).

(a)
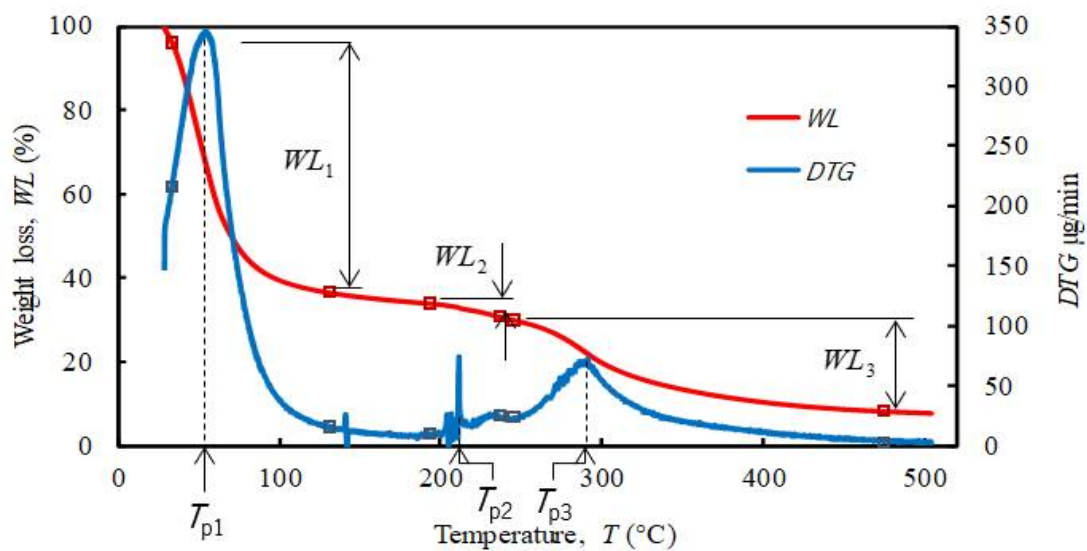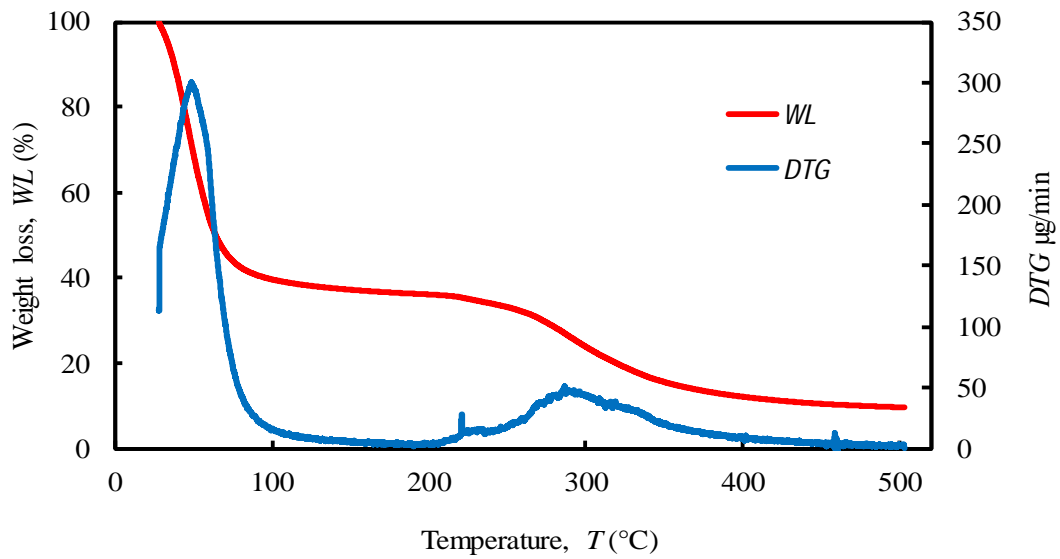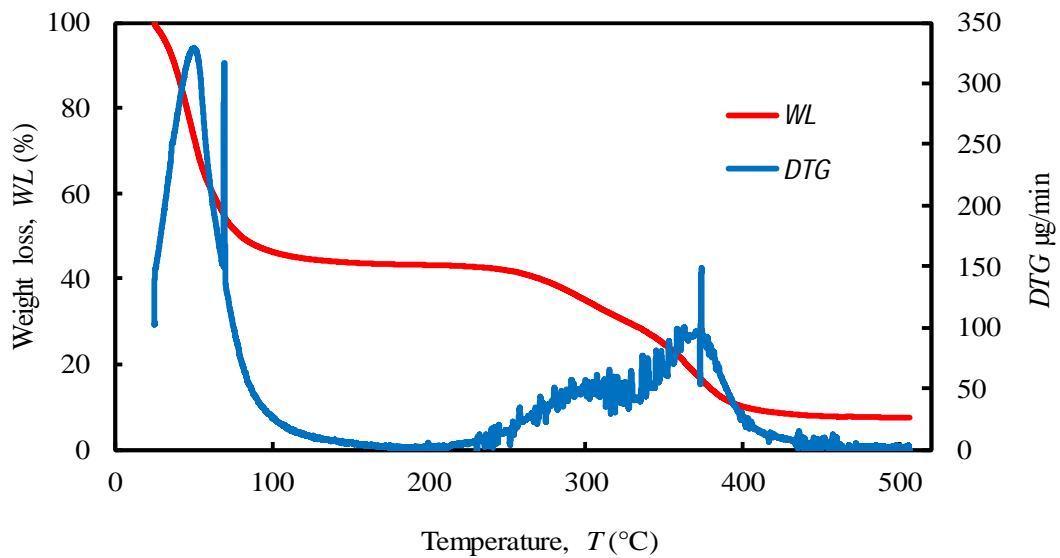
Figure 38: TG analyses of the porcine external ear cartilage (specimen #4): **(a)** Cartilage; **(b)** Composite; **(c)** Subcutaneous tissue.

Table 6 contains the weight loss (in percentage) that occurred in each thermal degradation phase, together with the peak temperatures where the velocity of the degradation (DTG) is maxima. At the bottom of this table, the average values have been resumed for each analysed structure. The mass of dried residues was also measured for each sample test, from which the residual weight has been calculated (Table 6).

The onset and endset temperatures of the registered thermal degradations are shown in Table 7, together with the average values per biological structure (i.e., cartilage, composite, and subcutaneous tissue).

Table 6: Thermal properties determined by TG/DTG analyses of the porcine external ear specimens. Values in parentheses represent the coefficient of variance.

Specimen ID and biological structure		T peaks of 1st derivative, T_{pi} (ºC) [Weight loss, WL_i (%)]	Residual weight (%)
PAC #1	Cartilage	42.2 [64.38]; 213.0 [5.98]; 273.7 [19.85]	9.07
	Composite	47.4 [48.35]; 207.3 [4.09]; 289.7 [31.13]	16.43
	Subcutaneous	37.4 [20.97]; 211.7 [1.94]; 384.2 [50.18]	7.19
PAC #2	Cartilage	52.1 [60.28]; 214.5 [7.03]; 285.1 [17.87]	14.82
	Composite	50.1 [61.44]; 228.6 [5.67]; 286.1 [24.25]	8.64
	Subcutaneous	40.1 [17.64]; 206.7 [0.59]; 305.0 [67.63]	14.14
PAC #3	Cartilage	45.6 [58.43]; 218.3 [6.15]; 289.9 [25.29]	10.13
	Composite	43.1 [48.96]; 217.1 [7.20]; 285.3 [32.61]	11.23
	Subcutaneous	47.7 [61.05]; - - [- -]; 284.2 [17.43]	11.03
PAC #4	Cartilage	49.4 [56.0]; 211.5 [11.06]; 288.1 [25.18]	7.76
	Composite	48.0 [56.86]; 221.5 [7.66]; 288.9 [25.81]	9.67
	Subcutaneous	50.2 [55.3]; 204.6 [2.0]; 303.0 [35.26]	7.44

Avg. (CoV)	Cartilage	47 (9%) [60 (6%)]; 214 (1%) [8 (32%)]; 284 (3%) [22 (17%)]	10 (29%)
	Composite	47 (6%) [54 (12%)]; 219 (4%); [6 (26%)]; 288 (1%) [28 (14%)]	11 (30%)
	Subcutaneous	44 (14%) [39 (58%)]; 208 (2%); [2 (53%]; 319 (14%) [43 (50%)]	10 (33%)

Table 7: Onset and endset temperatures of the thermal degradations. Values in parentheses represent the coefficient of variance.

Specimen ID and biological structure		T_{p1}, onset/endset (ºC)		T_{p2}, onset/endset (ºC)		T_{p3}, onset/endset (ºC)	
PAC #1	Cartilage	23.3	133.5	201.6	232.3	244.9	449.2
	Composite	30.5	129.5	195.5	226.8	241.8	478.0
	Subcutaneous	24.4	145.6	201.5	227.3	247.9	479.1
PAC #2	Cartilage	25.5	114.9	211.1	231.9	259.0	450.0
	Composite	25.3	140.8	218.0	239.0	265.0	451.8
	Subcutaneous	29.0	140.0	191.0	217.0	228.2	483.1
PAC #3	Cartilage	28.6	121.0	213.1	239.3	253.9	452.9
	Composite	29.4	111.5	201.7	227.3	248.5	478.9
	Subcutaneous	25.1	110.7			253.1	481.8

PAC #4	Cartilage	28.8	131.3	197.8	228.9	249.4	479.2
	Composite	28.3	110.6	212.3	238.0	248.2	478.2
	Subcutaneous	25.5	126.8	194.2	215.0	231.2	481.5

Avg. (CoV)	Cartilage	27 (10%)	125 (7%)	206 (4%)	233 (2%)	252 (2%)	458 (3%)
	Composite	28 (8%)	123 (12%)	207 (5%)	233 (3%)	251 (4%)	472 (3%)
	Subcutaneous	26 (8%)	131 (12%)	196 (3%)	220 (3%)	240 (5%)	481 (0%)

Table 6 reveals that most of the weight loss occurs during the first thermal degradation in every single analysed biological structure (60, 54, and 39% for cartilage, composite, and subcutaneous tissue, respectively, on average), which attains its maximum rate below 50 ºC (i.e., 47 ºC for cartilage and composite, and 44 ºC for subcutaneous tissue, on average). This major weight loss is most probably associated to the significant dehydration of the biological structures that ends at 125, 123, and 131 ºC (i.e., the endset temperatures, on average) for cartilage, composite, and subcutaneous tissue, respectively (Table 7). The fact that the subcutaneous tissue reveals less significant weight loss in the first thermal degradation (Table 6) than the cartilage and composite (39% against 60 and 54%, respectively, on average) seems to be in contradiction with the results ensuing by the DSC measurements (section 3.1.2), which revealed that water abandons the subcutaneous tissues more prematurely than in other structures (due to its fatty nature), thus requiring less energy to undergo such phenomenon. However, one should take due note that the referred difference in the weight loss is very much influenced by the results ensuing by specimens #1 and #2 than by the others, which renders the coefficient of variation of this measure to attain 58% (Table 6). Effectively, the values of weight loss in specimen #4 are very similar to each other (ranging from 55.3 to 56.86%), being higher for specimen #3 (61.05% for subcutaneous tissue). It is also worth noting that subcutaneous tissues take longer to undergo the first thermal degradation, on average (Table 7), as revealed by the onset (26 ºC) and endset (131 ºC) temperatures that have been registered. This last observation gives some consistency to the argument that the required energy to expel water from subcutaneous tissues may not be as low as it seemed through the DSC measurements, in comparison to that necessary in cartilage and composite structures.

Following the first thermal degradation, a small weight loss is verified around 200 ºC for every structure with comparative lower losses than in the first degradation (ranging from 2 to 8% on average,

as shown in Table 6). This occurrence renders possible to conclude that there was not any physical transformation worthy of mention, though a reference should be made to the fact that anhydrous (no water) collagen presents a melting point at 210 ºC (Ratner et al., 2004).

The third thermal degradation that has been registered through the TGA is accompanied by a significant weight loss, which occurs on average at 284, 288, and 319 ºC for cartilage, composite, and subcutaneous tissue, respectively (Table 6), giving rise to weight losses of 22, 28, and 43%. The referred values of temperatures (T_g) may be associated to collagen proteins degradation.

3.1.4 DMA: Multi-frequency Tensile and Compressive Loading

Dynamic mechanical analysis (DMA) was performed using samples of porcine external ear cartilage that have been prepared following the experimental procedure described in section 2.2.1 and tested according to the methods presented in section 2.3.2. Following the referred methods, the tensile tests were performed with *dog-bone*-shaped specimens (Figure 25), whereas the compression tests used flat circular specimens of 7 mm (app.) diameter (Figure 24), in quasi-dehydrated conditions.

Figures 39 and 40 show the observed viscoelastic behaviour (damping) of the porcine external ear cartilages when submitted to tensile and compressive loading, respectively, as a function of temperature (30-250 ºC) and frequency (1-20 Hz). As tanδ results from the ratio of the loss to the storage moduli (Equation 2.3), its representation gives some qualitative information on the viscoelastic state of the tissues (through the analysis of the rises and drops of tanδ), and consequently, enables identifying the paramount component (elastic or viscous) at a certain temperature and frequency.
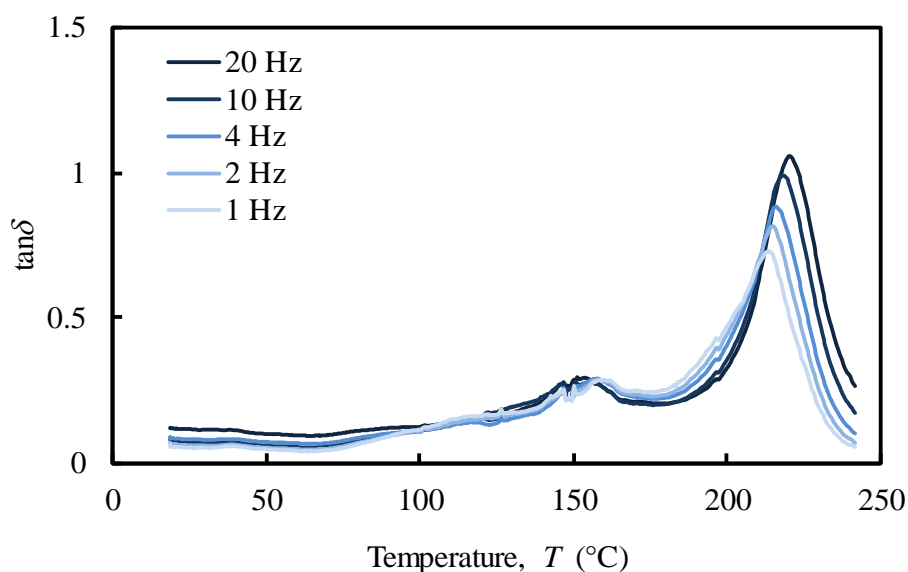
Figure 39: Tensile multi-frequency viscoelastic behaviour (damping) of the porcine external ear cartilage (specimen #1 harvested within the scapha).
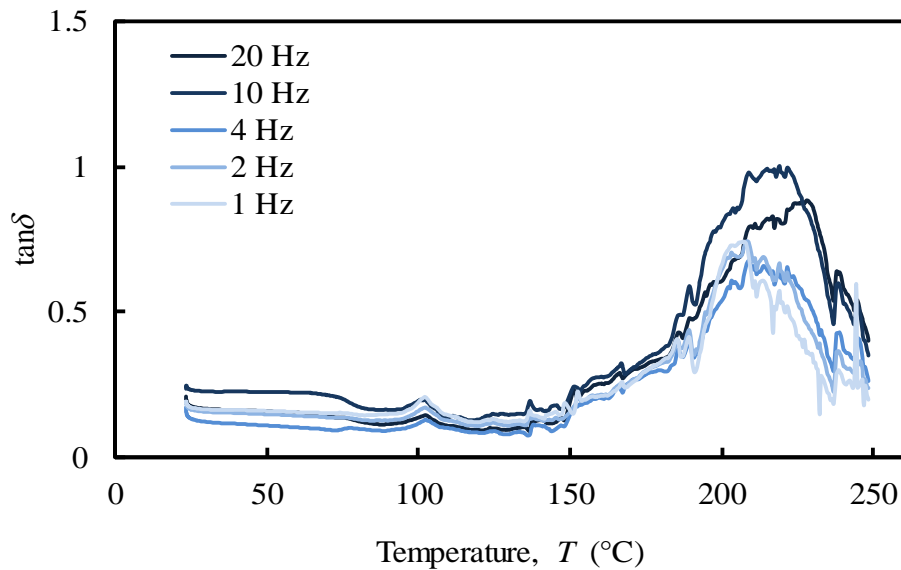
Figure 40: Compressive multi-frequency viscoelastic behaviour (damping) of the porcine external ear cartilage (specimen #1 harvested within the scapha).

Besides the validation of an experimental protocol to be applied to human nasal cartilages, this study in porcine auricular cartilages aims at investigating a possible relationship among temperatures, frequencies, and viscoelastic moduli to deeply understand the material thermo-mechanical behaviour.

Obviously, a higher $\tan\delta$ implies a material with a significant viscous part, while a lower value indicates the presence of a high elastic contribution (Moraes et al., 2017). As presented in Figure 39, the peaks above 200 °C (in tensile mode) showed a clear frequency-dependent behaviour, undoubtedly indicating the presence of a glass transition point (T_g). Moreover, the increase in the $\tan\delta$ peak temperatures (from 215 to 220 °C) with the increasing frequency allows to estimate the apparent activation energy that could provide important information on the cross-linking degree of the protein molecular chains. This will be further discussed afterwards with the principle specimens (human nasal cartilages) characterized in this work. The increase of $\tan\delta$ (from 0.7 to 1.0) is usually associated to material degradation and to an increased mobility of the molecular chains suggesting that the phase transition registered around 200 °C is probably the result of a protein denaturation within the cartilage matrix. Additionally, the secondary frequency-independent relaxation peaks close to 150 °C (after water release in the range of 90-100 °C) seem to be related to the melting of unstable crystalline regions of collagen that melts between 80-180 °C (Okamoto and Saeki, 1964), enabling a new irreversible spatial configuration of collagen within the matrix. Close to the physiological temperature of 37 °C no significant events were recorded, which means that the storage and loss moduli were slightly constant, and the composite has shown to be frequency-independent.

In compressive mode, the behaviour of porcine auricular cartilage specimens was clearly frequency-independent up to 250 ºC. However, three tanδ peaks can be identified in Figure 40 at 100, 180, and 210 ºC (app.). Despite the occurrence of some phase transitions of the amorphous and crystalline zones of collagen, these peaks are also related to the movement of water throughout the porous matrix. Firstly, at 90-100 ºC, in which there are a great amount of water that abandons the tissue (the storage modulus is highest at 90 ºC and drops drastically up to 100 ºC); Then, the strongly bounded water is released at higher temperatures increasing the viscosity of the tissue. Thus, the compressive mode is clearly ruled by the flow-dependent mechanism of the interstitial water throughout the pores (Park et al., 2004).

3.1.5 DMA: Creep-recovery Tests

These tests (also in section 3.1.6) were performed using composite *dog-bone*-shaped specimens (Figure 25) harvested within the scapha, in quasi-dehydrated conditions. The applied load has been fixed to attain a (sudden and constant) tensile stress of approximately 0.7 MPa for an elapsed time of 3600 s. The stress intensity value is visibly lower than the ultimate tensile stress attained by the material under monotonic loading (section 3.1.1), thus assuring a linear response in the course of the loading process (Figure 36c; Table 4).

Figure 41 shows the typical observed creep behaviour of a specimen whose percentage of cartilage throughout the thickness was found equal to 47.2%. The trend revealed by the response (i.e., ascending strain) over time is coherent with a creep test.
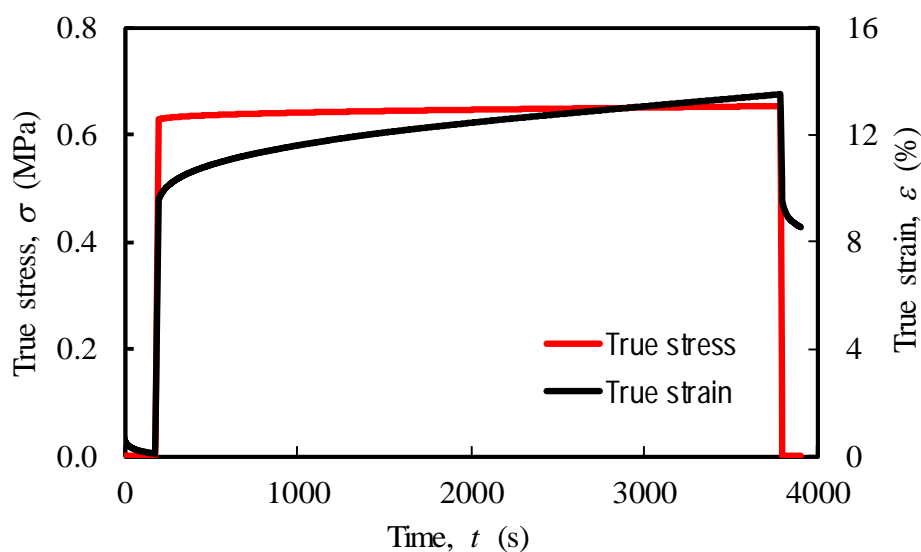
Figure 41: Experimental creep behaviour of the porcine external ear composite (specimen #3 harvested within the scapha).

In these tests the applied displacement value has been fixed to 0.8 mm for an elapsed time of 900 s, as to attain an (sudden) initial stress intensity similar to the one obtained in creep-recovery tests (linear elastic domain of the composite, referred in the previous section). This time duration has been chosen as to avoid severe dehydration of the samples, which induces a spurious stress state in the specimen.

Figure 42 shows the typical observed relaxation behaviour of a porcine external ear composite harvested within the scapha. The percentage of cartilage throughout the thickness of specimen #5 was found equal to 56.1%. The tendency shown by the response (i.e., descending stress) is comprehensible in a relaxation test.
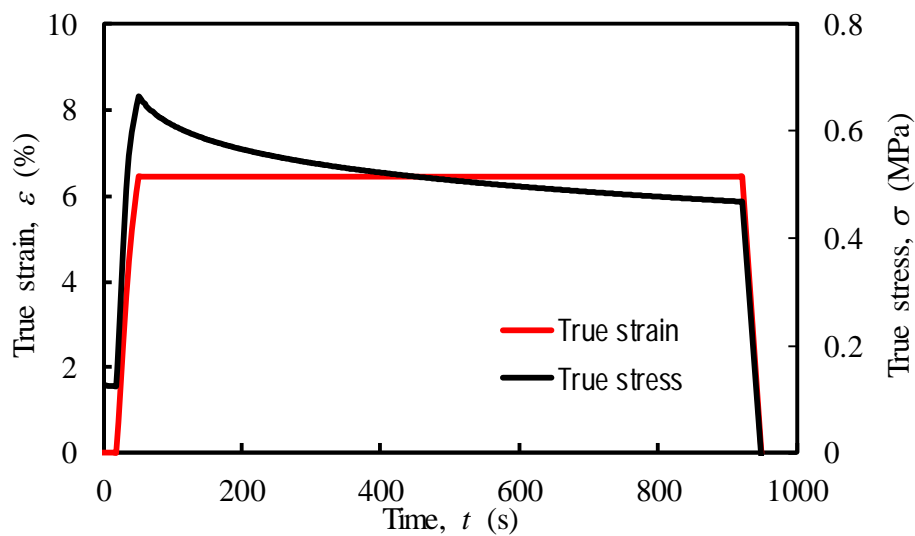
Figure 42: Experimental relaxation behaviour of the porcine external ear composite (specimen #5 harvested within the scapha).

3.2 Human Experimental Results

Following the mechanical characterization of porcine tissues (the animal model) described in the preceding sections, experimental protocols were developed to undergo DSC, TGA, and DMA measurements in human nasal cartilages. Hence, a comprehensive experimental characterization has been made on tissues extracted from the nasal septum (NS), ULC, and LLC of two male donors (section 2.2.2). Discussions are presented at the end of each topic.

3.2.1 DSC Measurements

The results of the DSC are displayed in Figures 43, 44, and 45 for cartilage, composite, and subcutaneous tissue of the NS, ULC, and LLC (using a heating rate of 10 ºC/min). Table 8 resumes the main thermal features of the human nasal cartilage specimens tested within the referred conditions.
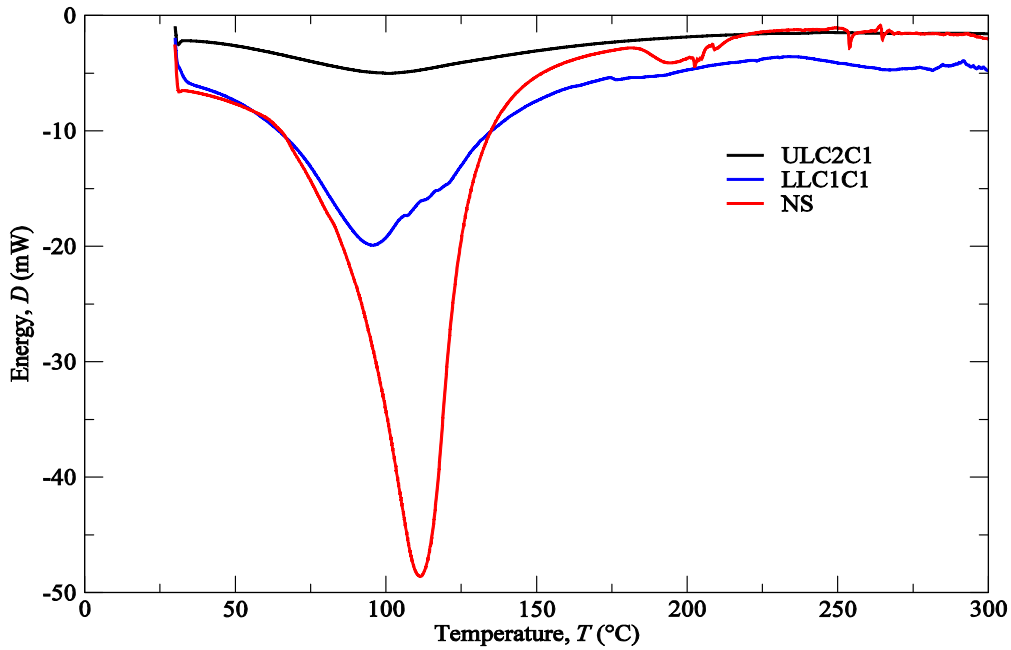
Figure 43: DSC analyses of the cartilage from NS, ULC, and LLC of donor #1.
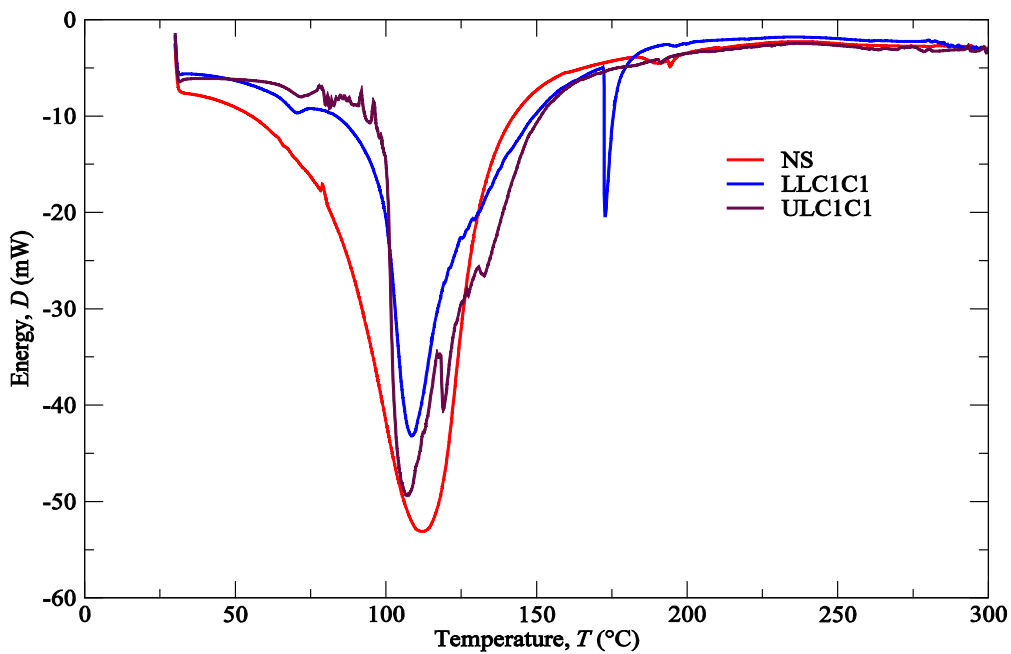
Figure 44: DSC analyses of the composite from NS, ULC, and LLC of donor #1.
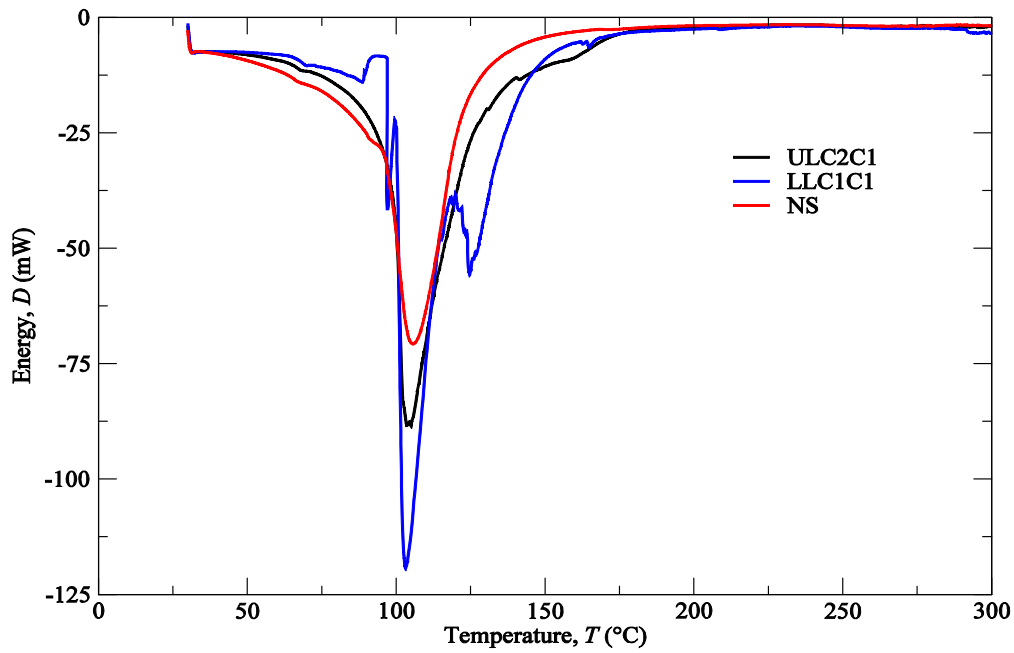
Figure 45: DSC analyses of the subcutaneous tissue from NS, ULC, and LLC of donor #1.

Table 8: Main thermal features of the human nasal cartilages (NS, ULC, and LLC) through DSC analysis.

Specimen ID and biological structure		1st peak		2nd peak		3rd peak	
		T (°C)	ΔH (J/g)	T (°C)	ΔH (J/g)	T (°C)	ΔH (J/g)
LLC #1	Cartilage	95.4	571.8				
	Composite	108.6	650.7	172.8	37.2		
	Subcutaneous	103.2	494.3	124.7	123.2		
LLC #2	Cartilage	107.8	1116.3				
	Composite	127.2	214.7	198.6	6.4		
	Subcutaneous	138.0	41.0				
ULC #1	Cartilage	101.7	208.0				
	Composite	106.9	920.5				
	Subcutaneous	101.1	1453.4				
ULC #2	Cartilage	100.9	234.2				
	Composite	83.3	223.4	117.4	6.3		
	Subcutaneous	104.3	1660.8				
NS #1	Cartilage	121.6	1643.4	181.9	7.1	190.6	5.7
	Composite	102.8	1583.1	204.2	0.6		
	Subcutaneous	133.5	1198.9				
NS #2	Cartilage	111.4	1288.6	202.5	0.4	253.8	1.7
	Composite	112.1	1236.2	194.1	0.6		
	Subcutaneous	105.6	1520.5				

Samples with higher changes in the enthalpy indicate that they require larger amounts of energy for decomposition. A small T_g peak can be observed at 60-80 ºC in the composite and subcutaneous tissue specimens (Figures 44 and 45) due to melting of the unstable crystalline region of collagen matrix. Although a main peak has been attributed to water evaporation between 100 and 130 ºC for the totality of the specimens, no correlation among the different nasal regions has been observed in the measured enthalpies (Table 8) because of their different water content. In general, a higher temperature peak (1st peak) can be depicted in the subcutaneous tissue compared to cartilage (Figure 45) due to their high-water binding capacity (also supported by TGA measurements).

A second peak is also observed at around 200 ºC due to strongly bonded non-interstitial water in cartilage and composite specimens (Figures 43 and 44), but not in the subcutaneous tissues. Another interesting feature is the subcutaneous narrow water temperature peaks. While the cartilage and composite specimens show a wide large peak between 50 and 150 ºC (Figures 43 and 44), specimens on subcutaneous tissues display a smaller range of temperatures between 75 and 125 ºC (Figure 45). This result indicates once again the different nature of the binding water inside the studied specimens. No other significant thermal events can be observed up to 300 ºC.

3.2.2   TGA Measurements

TGA was performed aiming at identifying phase transitions (thermal degradations) in the material over time as the temperature changes. The used protocol imposed a heating rate of 3 ºC/min on a set of samples constituted by cartilage, composite, and subcutaneous tissue. The results of the TGA are displayed in Figures 46, 47, and 48 for cartilage, composite, and subcutaneous tissue of the NS, ULC, and LLC, respectively. Alike section 3.1.3, in the referred figures, the WL curve represents the weight loss (in percentage) as a function of the temperature T (within the interval 30-500 ºC), while the DTG curve stands for the first derivative of the TG over the same interval of temperatures.

The first derivative peak, onset and endset temperatures (pairs of small squares depicted in Figures 46 to 48), corresponding weight losses (WL_i), and mass of dried residues at 500 ºC were determined for each case and registered in Tables 9 and 10.
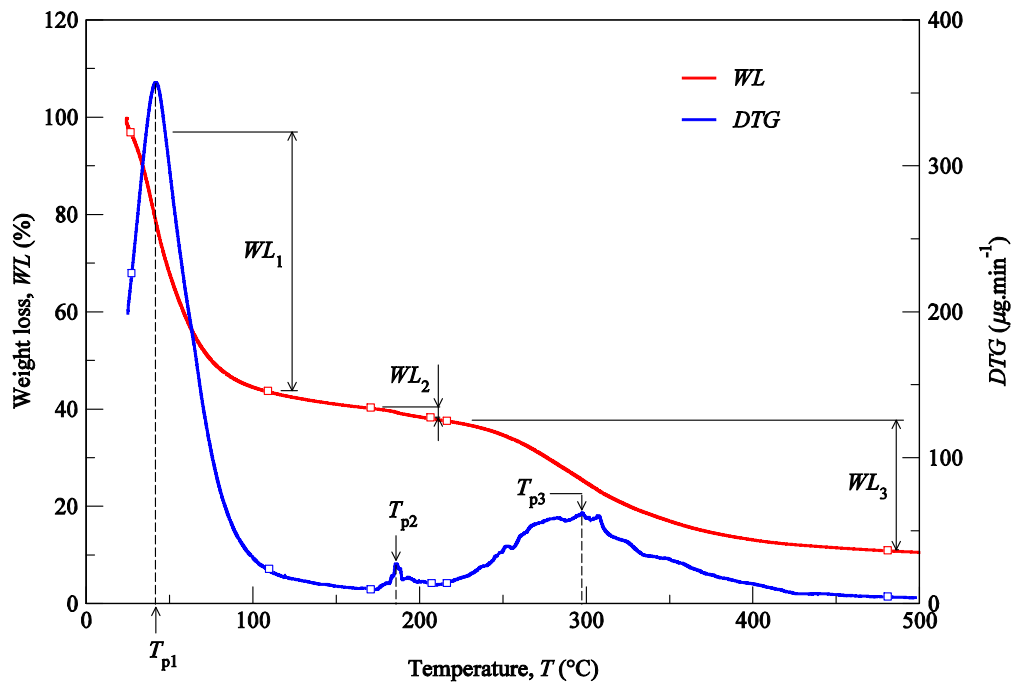
(a)
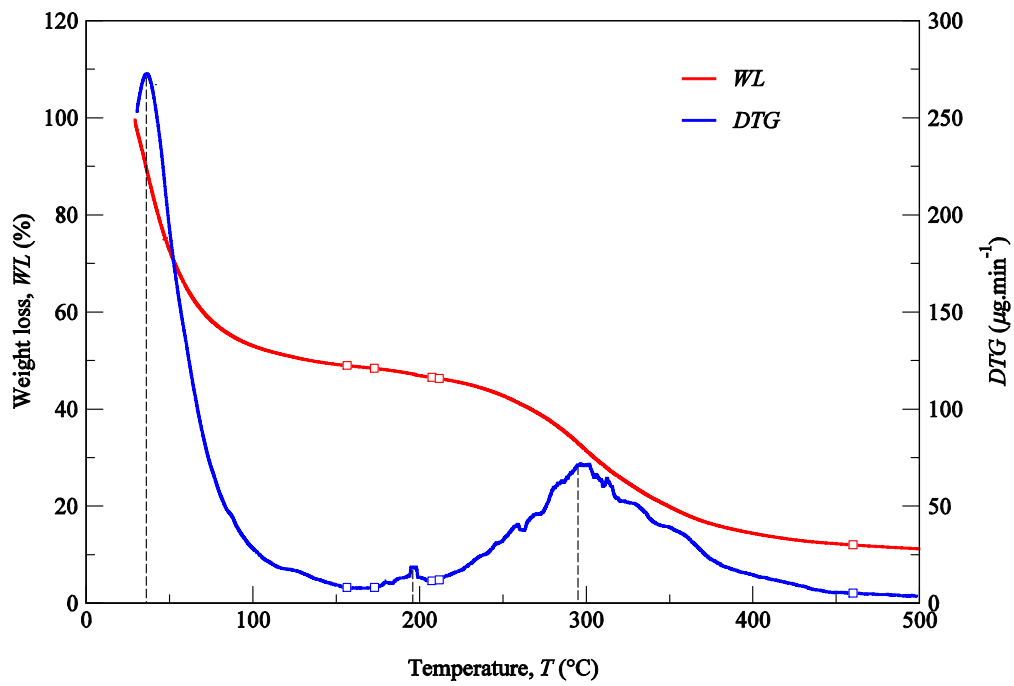
(b)
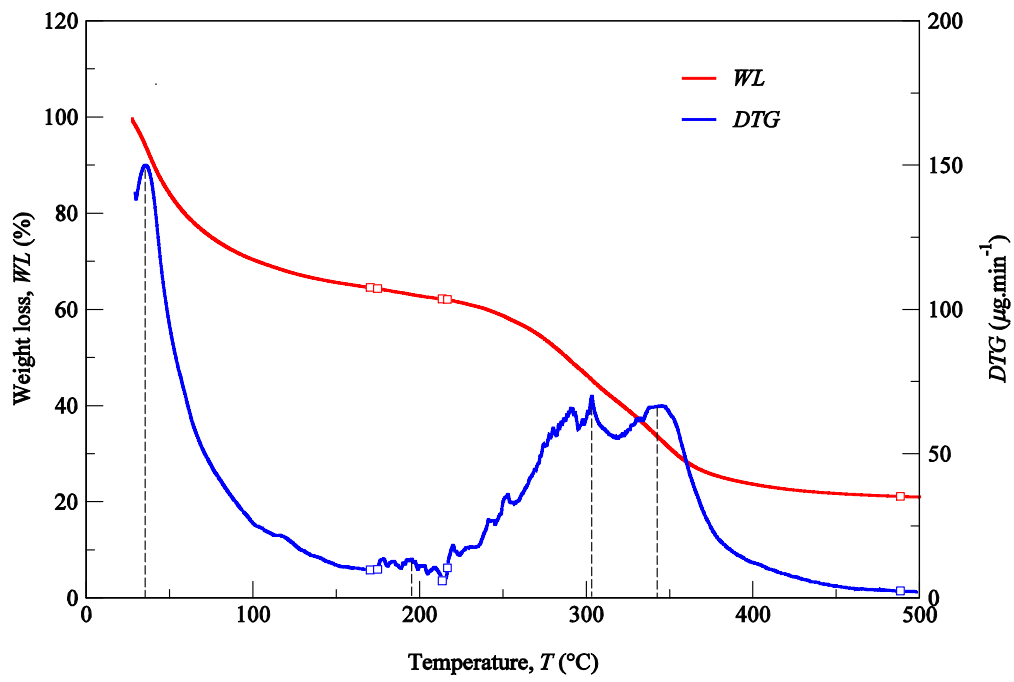
(c)

Figure 46: TG analyses of the LLC: **(a)** Cartilage; **(b)** Composite; **(c)** Subcutaneous tissue (specimen #1, donor #2).
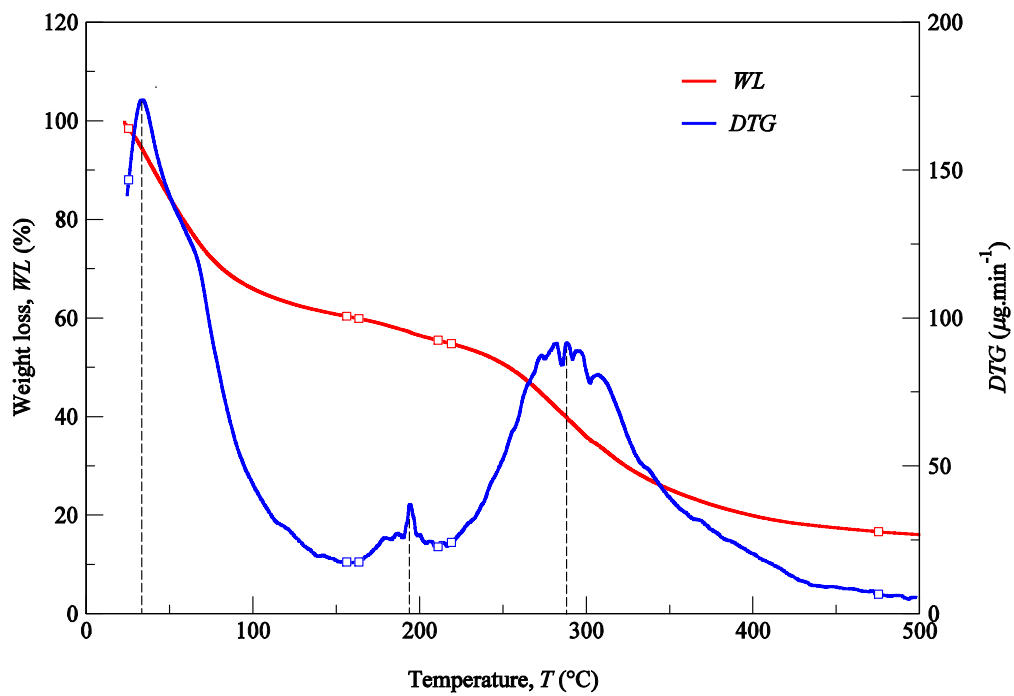
(a)
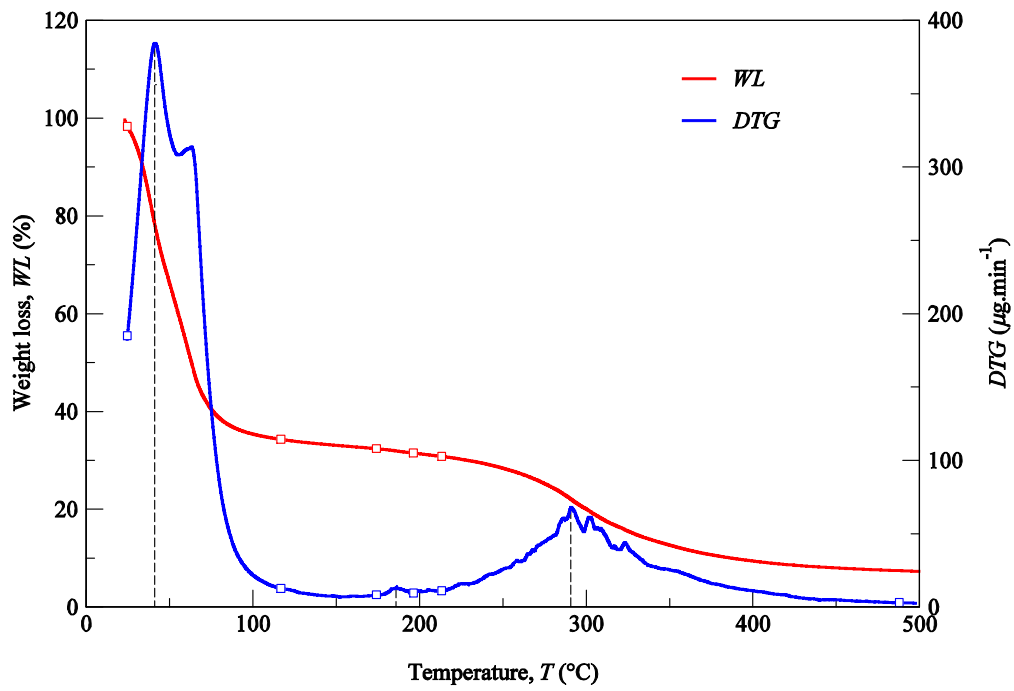
(b)
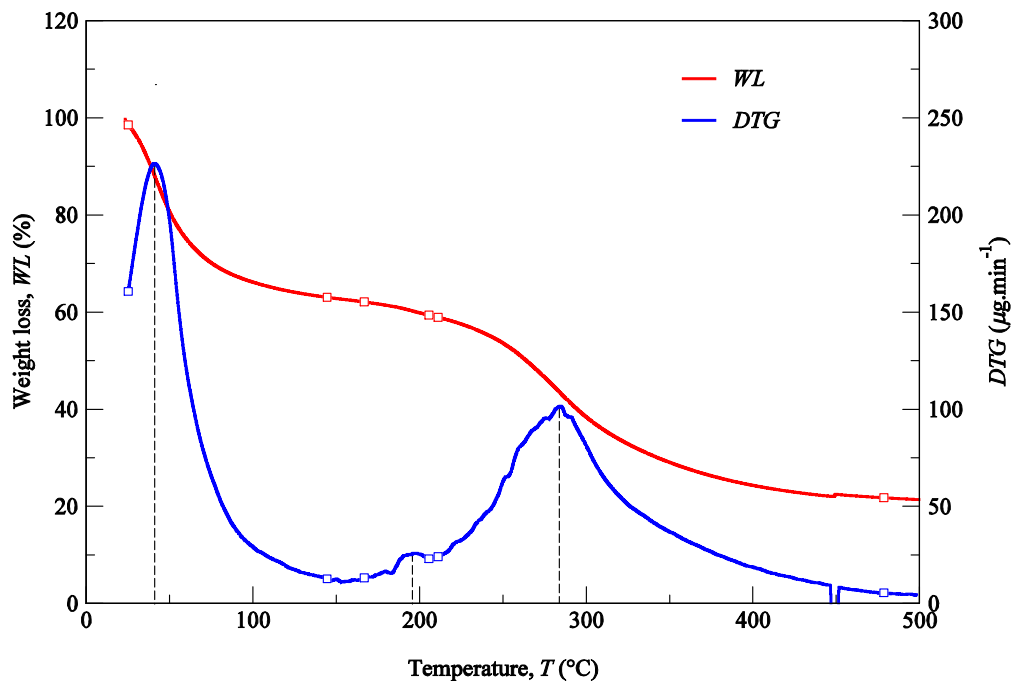
(c)

Figure 47: TG analyses of the ULC: **(a)** Cartilage (specimen #2, donor #2); **(b)** Composite (specimen #2, donor #2); **(c)** Subcutaneous tissue (specimen #1, donor #2).

(a)

(b)
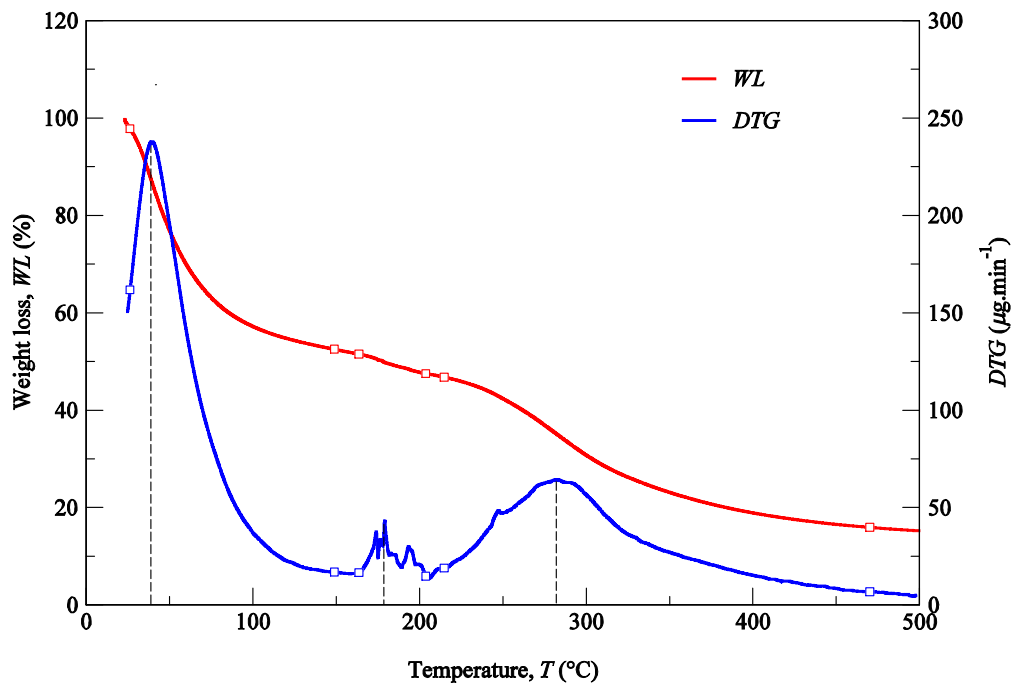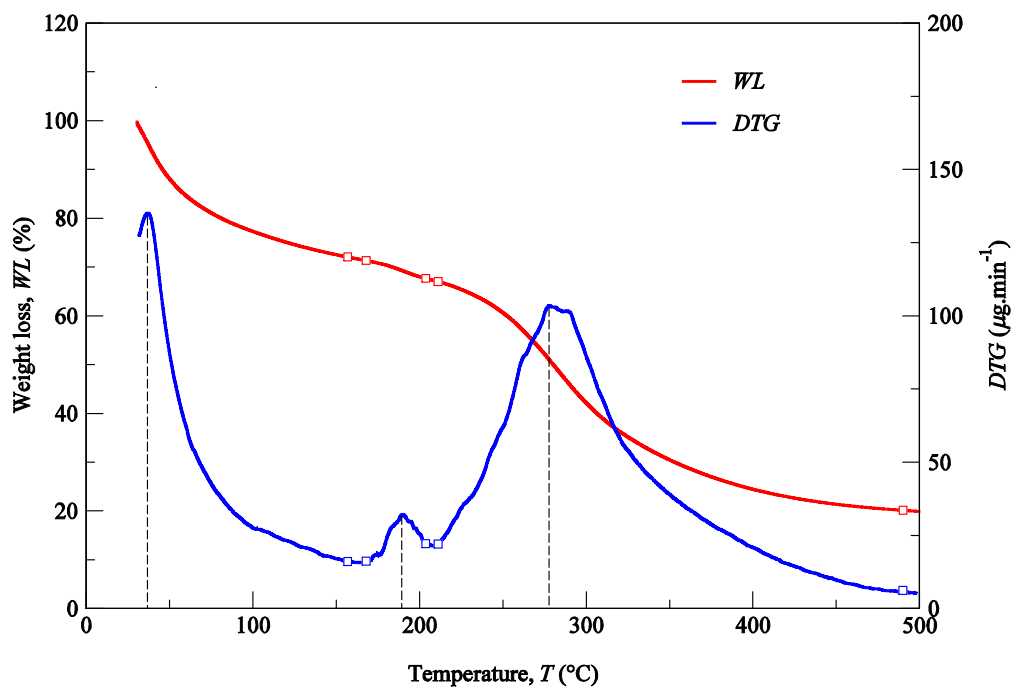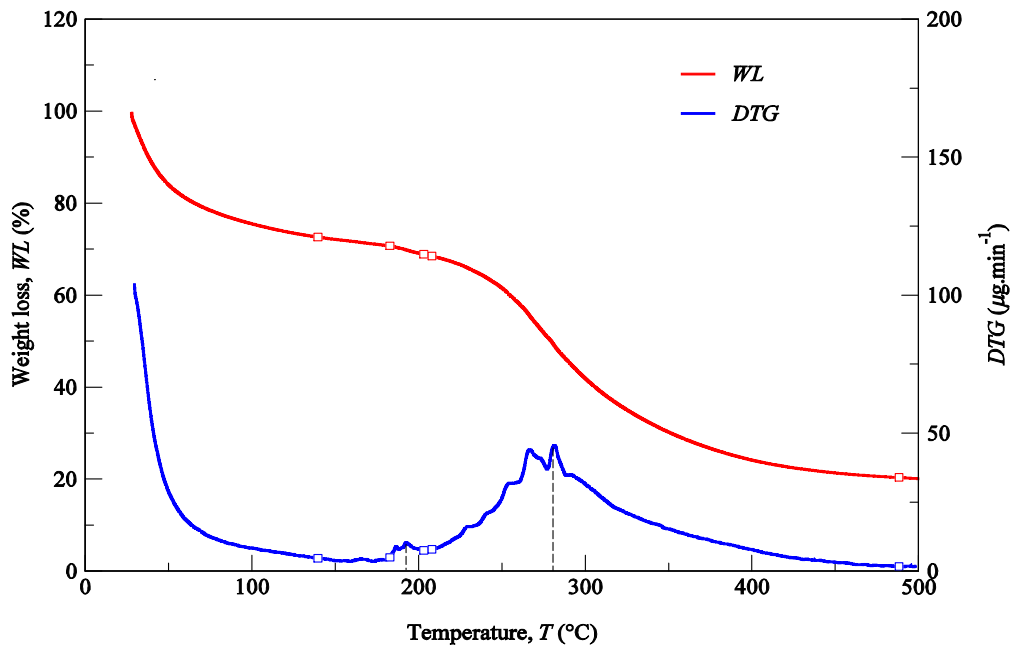
Figure 48: TG analyses of the NS: **(a)** Cartilage; **(b)** Composite; **(c)** Subcutaneous tissue (specimen #1, donor #1).

Table 9: Thermal properties determined by TG/DTG analyses. Average values underneath.

Specimen ID and biological structure		T peaks of 1st derivative, T_{pi} (ºC) [Weight loss, WL_i (%)]	1st *DTG* peak (µg/min)	Residual weight (%)
LLC #1	Cartilage	42.3 [57.17]; 186.5 [3.36]; 298.1 [27.25]	357.1	10.57
	Composite	36.0 [49.81]; 197.0 [0.51]; 295.0 [36.98]	272.7	11.26
	Subcutaneous	35.3 [40.60]; 195.2 [0.67]; 303.2 [13.86]; <u>342.5 [13.86]</u>	150.0	9.75
LLC #2	Cartilage	46.0 [55.67]; 192.7 [2.99]; 294.4 [28.01]	364.8	11.89
	Composite	42.3 [65.67]; 189.0 [3.42]; 308.0 [23.25]	334.6	6.61
	Subcutaneous	35.5 [35.49]; <u>177.3 [0.66]</u>; <u>217.3 [11.0]</u>; 303.0 [11.07]	150.0	21.0
ULC #1	Cartilage	26.7 [22.03]; 188.0 [7.63]; 284.0 [53.34]	39.9	15.6
	Composite	31.4 [45.14]; 141.5 [0.81]; 306.7 [20.2]; <u>347.4 [24.82]</u>	206.9	9.03
	Subcutaneous	41.1 [36.26]; 195.8 [0.79]; 283.9 [41.53]	226.7	21.42
ULC #2	Cartilage	33.3 [38.81]; 193.9 [5.76]; 288.2 [38.9]	173.8	16.09
	Composite	41.0 [65.85]; 185.9 [1.74]; 291.3 [23.78]	384.5	7.35
	Subcutaneous	30.0 [21.47]; 190.2 [5.43]; 283.0 [55.21]	81.8	17.48
NS #1	Cartilage	38.9 [45.32]; 178.5 [0.95]; 282.1 [37.6]	378.0	16.13
	Composite	36.7 [27.95]; 189.4 [4.38]; 277.7 [46.57]	135.1	19.94
	Subcutaneous	28.7 [26.32]; 192.5 [1.61]; 280.8 [51.94]	104.1	20.13
NS #2	Cartilage	39.2 [25.79]; 197.0 [7.28]; 285.0 [31.93]	209.3	15.25
	Composite	41.7 [51.74]; 190.8 [2.52]; 280.8 [30.71]	318.2	14.31
	Subcutaneous	31.2 [39.56]; 200.0 [3.67]; 283.0 [38.55]	154.3	16.29

LLC (Avg.)	Cartilage	44.2 [56.4]; 189.6 [3.2]; 296.3 [27.6]	361.0	11.2
	Composite	39.2 [57.7]; 193.0 [2.0]; 301.5 [30.1]	303.7	8.9
	Subcutaneous	35.4 [40.6]; (195.2 [0.7]); 303.1 [12.5]	150.0	15.4
ULC (Avg.)	Cartilage	30.0 [30.4]; 191.0 [6.7]; 286.1 [46.1]	106.9	15.8
	Composite	36.2 [55.5]; 163.7 [1.3]; 299.0 [22.0]	295.7	8.2
	Subcutaneous	35.6 [28.9]; 193.0 [3.1]; 283.5 [48.4]	154.3	19.5
NS (Avg.)	Cartilage	39.1 [35.6]; 187.8 [4.1]; 283.6 [34.8]	293.7	15.7
	Composite	39.2 [39.8]; 190.1 [3.5]; 279.3 [38.6]	226.7	17.1
	Subcutaneous	30.0 [32.9]; 196.3 [2.6]; 281.9 [45.2]	129.2	18.2

Table 10: Onset and endset temperatures of the thermal degradations obtained by TG/DTG analyses.

Specimen ID and biological structure		T_{p1}, onset/endset		T_{p2}, onset/endset		T_{p3}, onset/endset	
LLC #1	Cartilage	25.0	110.1	171.1	207.5	216.7	481.1
	Composite	25.5	156.3	173.0	207.5	211.8	460.8
	Subcutaneous	27.2	170.5	174.8	213.6	216.7	488.5
LLC #2	Cartilage	25.6	153.2	172.3	206.9	216.7	479.9
	Composite	23.8	145.8	171.1	214.9	219.8	477.4
	Subcutaneous	27.5	168.0			217.3	481.1
ULC #1	Cartilage	25.0	137.2	156.9	205.0	217.3	462.0
	Composite	25.3	126.1	137.8	211.8	219.2	481.1
	Subcutaneous	25.0	144.6	166.8	205.6	211.1	478.7
ULC #2	Cartilage	25.6	156.3	163.7	211.2	219.2	475.6
	Composite	25.0	116.9	174.2	196.4	213.6	487.9
	Subcutaneous	25.0	142.1	160.6	202.5	208.7	479.3
NS #1	Cartilage	26.3	148.9	163.7	203.7	214.9	470.0
	Composite	33.8	156.9	168.0	203.8	211.2	490.4
	Subcutaneous	29.9	139.7	182.8	203.2	208.1	488.5
NS #2	Cartilage	25.5	158.2	173.6	208.7	213.0	478.1
	Composite	29.9	110.7	174.2	205.0	213.6	479.3
	Subcutaneous	25.5	90.4	178.5	209.3	221.0	447.9
LLC (Avg.)	Cartilage	25.3	131.7	171.7	207.2	216.7	480.5
	Composite	24.7	151.1	172.1	211.2	215.8	469.1
	Subcutaneous	27.4	169.3	(174.8)	(213.6)	217.0	484.8

ULC (Avg.)	Cartilage	25.3	146.8	160.3	208.1	218.3	468.8
	Composite	25.2	121.5	156.0	204.1	216.4	484.5
	Subcutaneous	25.0	143.4	163.7	204.1	209.9	479.0

NS (Avg.)	Cartilage	25.9	153.6	168.7	206.2	214.0	474.1
	Composite	31.9	133.8	171.1	204.4	212.4	484.9
	Subcutaneous	27.7	115.1	180.7	206.3	214.6	468.2

Thermogravimetry curves showed that the degradation of cartilage, composite, and subcutaneous tissue of the NS, ULC, and LLC take place in three well-defined thermal events (Figures 46 to 48), represented as WL_i, with no significant differences in TGA curves being noticed for the mentioned biological structures. Table 9 shows the obtained measures regarding the referred events (three thermal peaks and corresponding weight losses), together with the mean values (underneath Table 9) that have been registered for each biological structure. As non-significant differences have been detected for the analyzed samples, one can comment on the attained intervals of mean temperatures for each peak considering the totality of the results, namely: 30-44.2 °C for the first peak; 163.7-196.3 °C for the second peak; Finally, 279.3-303.1 °C for the third peak.

Table 9 also shows three samples with four peaks on the first derivative of the TG, namely the LLC #1 subcutaneous tissue, LLC #2 subcutaneous tissue, and ULC #1 composite. For the referred cases, two samples have revealed the fourth peak in the vicinity of 350 °C (namely, the subcutaneous tissue from the LLC #1 and the composite from the ULC #1, underlined values in Table 9) that are most probably due to contamination with nose trimmers, fatty tissue, or due to bony/calcified cartilage traces. Regarding the remaining signalized sample (the subcutaneous tissue from LLC #2), it seems that the analysis has revealed two intermediate (thermal) peaks (177.3 and 217.3 °C), whose reason is yet unknown. For this reason, this particular result has not been considered in the calculation of the average values presented underneath Table 9. This table also disregards the fourth peak (above referred). The residual weight at 500 °C that was measured has also been found very disperse, which does not allow to establish a significant relation with a given biological structure.

Table 10 shows the onset and endset temperatures corresponding to each thermal event registered for every biological structure, together with the average values of these intervals (underneath). Hence, for all analyzed biological structures, the first thermal event arises on average between 24.7 and 169.3 °C (main peak at 36.5 °C, overall avg. in Table 9; CoV: 15%), which corresponds to the initial weight loss (in water). The weight loss due to water evaporation has been registered in 42% (on avg.), with high scatter (CoV: 33%), presenting values between 28.9 and 57.7

wt%. However, for most of the samples the water loss of the composite specimens was always higher than the one obtained for the subcutaneous tissues and cartilages (Table 9, on avg.: 57.7 wt% for LLC, 55.5 wt% for ULC, and 39.8 wt% for NS). A second small but consistent weight loss (overall avg. between 0.7 and 6.7 wt%) was observed in the temperature range of 156.0-213.6 ºC (on avg., Table 10), revealing that the weight loss in cartilage specimens was always higher than in the remaining structures (Table 9, on avg.: 3.2 wt% for LLC, 6.7 wt% for ULC, and 4.1 wt% for NS). Above the previous temperature interval, the weight continues to diminish until a third phase between 209.9 and 484.9 ºC is revealed (on avg., Table 10). A variable solid residue content at 500 ºC between 8.2 and 19.5 wt% was observed for all the specimens (on avg., Table 9).

Differently to other studies about hyaline cartilages that show high water content (up to 85%), in this work, cartilages have revealed lower values of water content (Table 9), with 42% on average of the net weight (Martinho et al., 2013). It is reasonably plausible that a given donor (cadaveric condition) can present gradients of water content within the body parts due to natural dehydration mechanisms. Another reason might be attributed to donors' age (seventy-year-old males), who could present high content in calcified cartilage, which is expected to have less water content. However, despite the existence of an age-dependent relationship between biochemical composition and mechanical properties of nasal cartilages (Rotter et al., 2002), usually no significant variations in water content as a function of age or gender have been observed. The most plausible explanation for the lower water content could be attributed to storage procedure and manipulation of the specimens (Homicz et al., 2003). In this study, the samples were not kept in isotonic solution at 4 ºC, as usually reported in the literature. As referred in section 2.2.2, after dissection of biological parts, the samples were immediately shaped by metallic die-cutting tools and dry frozen at -40 ºC. This procedure was adopted after the observation of significant changes in the mechanical and physiological properties of the samples (i.e., in porcine tissues) after storage in isotonic solution. Effectively, with the adoption of such procedure for porcine tissues (referred in the literature), the specimens were found excessively turgid and swelled, barely after a few hours at 4 ºC. This condition was found inappropriate to assure the reproducibility and repeatability of the issued measures.

The speed of the water content loss represented by the first DTG peak and the weight loss (in percentage) reported in Table 9 showed different behaviour in cartilages and subcutaneous tissues for LLC, ULC, and NS structures. It was found that cartilage release more water and more rapidly than the subcutaneous tissues. A reasonable explanation for this could be attributed to proteoglycans and collagen molecules actions that promote a matrix with a very efficient water-binding capacity. However,

water is predominantly weakly bonded to aminoglycan side chains of aggrecan molecules (Spahn et al., 2006). In general subcutaneous tissues water content range between 6 and 26%, however there is no information in the literature regarding nasal subcutaneous tissues (Thomas et al., 1962). Subcutaneous specimens have a higher amount of adipose and collagen tissues. Collagen fibers produce a large surface area and form extensive networks, with high water-binding capacity (Gniadecka, 1995), supporting somehow the observed results. The small peak detected in the range of 180-200 ºC can be attributed to tightly bonded water. Chemically bonded water is estimated to be around 4% in cartilage and it is expected to evaporate at temperatures around 200 ºC (Ficai et al., 2011). The degradation that occurs between 209.9 and 484.9 ºC (on avg., Table 10) is attributed to protein structure components decomposition, such as deamination, decarboxylation, and depolymerization of the polypeptide bonds (da Costa et al., 2017). The solid residues at 500 ºC seem to be in accordance with previous similar analyses. No relevant literature is found about thermogravimetric analysis of cartilage at such high temperatures (Bobacz et al., 2004).

3.2.3 DMA: Multi-frequency Tensile and Compressive Loading of NS

The results of the DMA for tensile and compressive multi-frequency analyses are displayed in Figures 49 and 50, respectively, for cartilaginous tissues of the nasal septum (NS) (that does not contain subcutaneous tissue). DMA is the most sensitive technique for the measurement of glass transition temperatures and for detection of secondary relaxation events that are not detectable by other thermal techniques, such as DSC, resulting in data regarding the stiffness of a polymer, molecular motion, relaxation process, structural hetero groups, and morphology of the polymer blend systems (Rahimi et al., 2011).

As referred in section 2.3.2, the results are expressed as storage (E') and loss (E'') moduli, and damping factor (tanδ). The storage modulus represents the ability of a material to store energy, then more prone to deform elastically (Wilcox et al., 2014). The loss modulus represents the ability of a material to dissipate energy (Wilcox et al., 2014). The tanδ is the ratio of the loss modulus to the storage modulus (Equation 2.3) and provides information on the relative contribution of the viscous and elastic components of a viscoelastic material (Menard, 2008). Therefore, a high tanδ value implies a material with a significant non-elastic strain component and a low value indicates one with a high elastic contribution (Moraes et al., 2017).
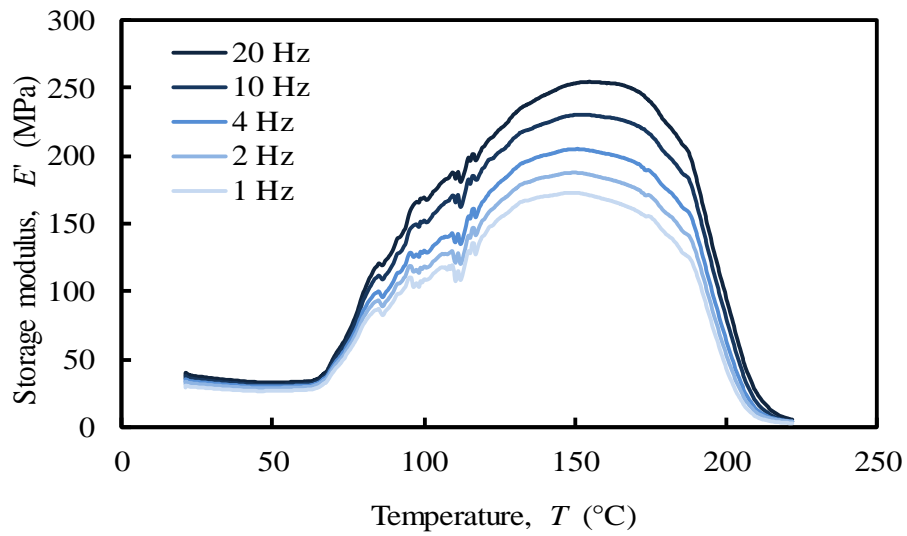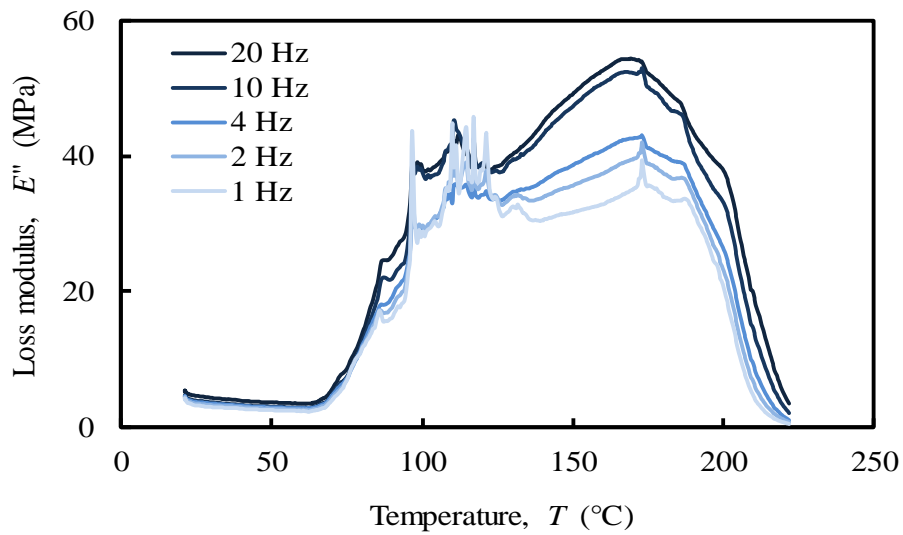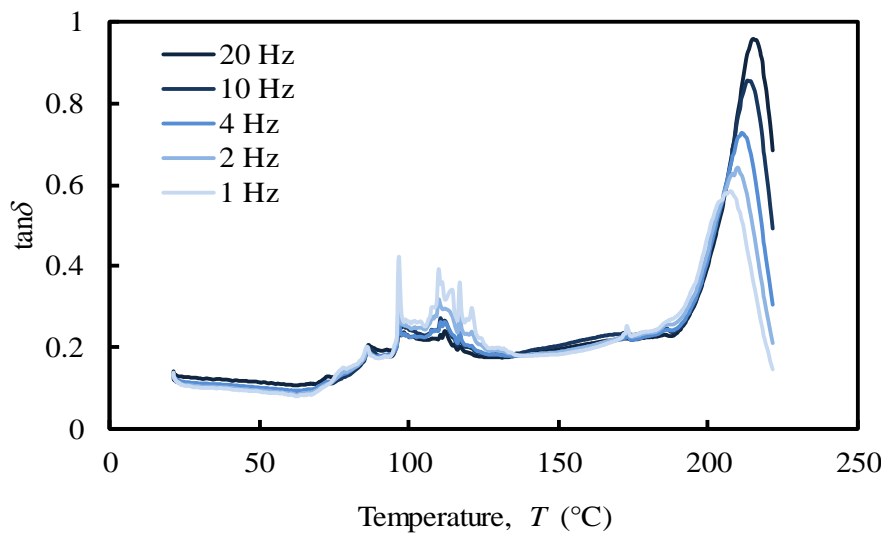
Figure 49: Tensile multi-frequency **(a)** storage and **(b)** loss moduli, **(c)** damping of the NS (specimen #2, donor #1).
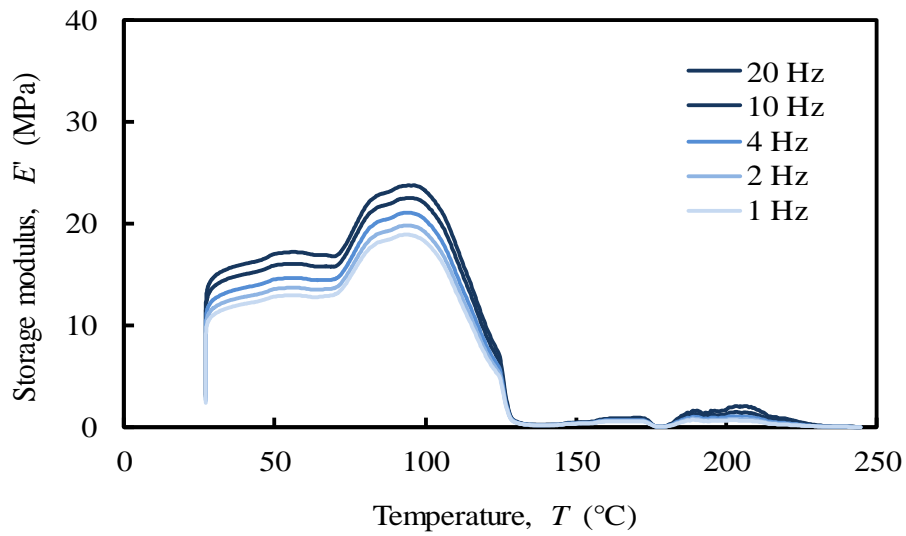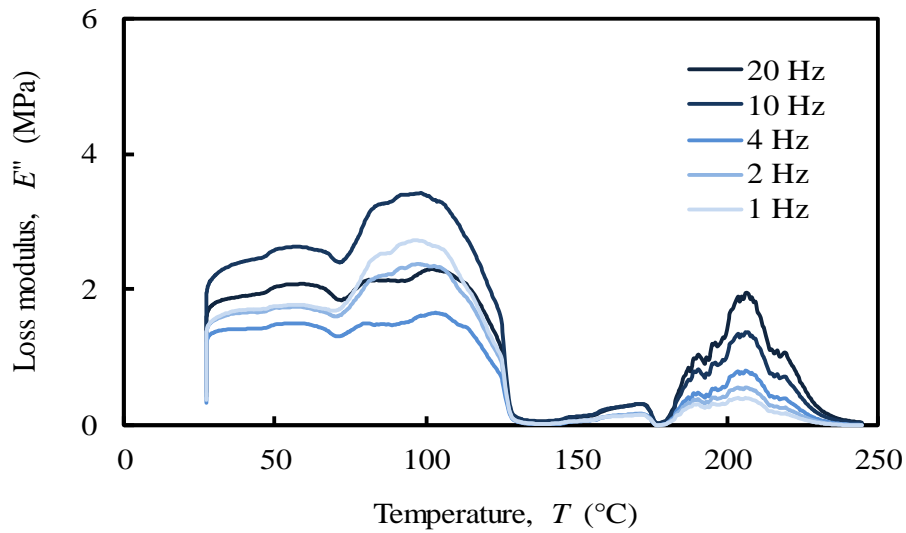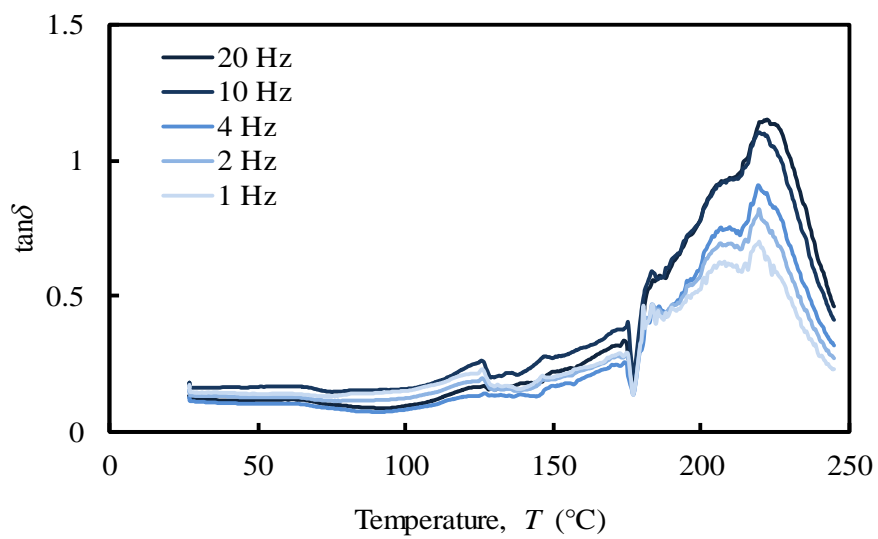
Figure 50: Compressive multi-frequency **(a)** storage and **(b)** loss moduli, **(c)** damping of the NS (specimen #3, donor #1).

DMA has been previously used to determine the viscoelastic properties of human lower limb joint and mandibular articular cartilages, with imposed frequencies from 0.1 to 10 Hz (Sadeghi et al., 2015; Espino et al., 2014). However, the evaluation of the viscoelastic properties of nasal cartilages at high temperatures and over a similar frequency range has never been studied. Typically, the literature analyses the relationship between oscillation frequencies and moduli at fixed temperatures, more frequently at the physiological temperature of 37 °C or in a range of temperatures up to 100 °C. In this work, a relationship among frequencies (1-20 Hz), temperatures (up to 250 °C), and moduli was investigated to deeply understand the thermo-mechanical behaviour of nasal cartilages. The aim is to undergo a comprehensive study on thermo-mechanical properties of nasal cartilages for a future design of a composite (polymeric) material that could be used in reconstruction surgery of the human nose regions.

The analysis of the tensile loading mode (Figure 49) showed a different behaviour of the NS tissues comparatively to the compressive loading mode (Figure 50). In the first case, a series of secondary frequency-independent relaxation peaks in the range of 70-100 °C (Figure 49c) was revealed due to melting of crystalline regions of collagen. The motions of the main and side chains of collagen molecules become significant in this region when a tensile force is applied, causing an irreversible spatial reorganization within the cartilage matrix (June and Fyhrie, 2010; Tóth et al., 2007). This behaviour is in accordance with the previously described different structural organization of collagen that has been reported to be composed of an unstable crystalline region with little orientation that melts at low temperatures (80-180 °C), a natural amorphous region associated to second-order phase transitions that melts at around 120 °C, and a stable crystalline region with a melting point at 200 °C (Okamoto and Saeki, 1964). At the physiological temperature (app. 37 °C) no significant events in storage (E') and loss (E'') moduli were recorded. The system is clearly frequency-independent in tensile mode at this temperature. In the compression analysis the system showed a peak in the storage modulus within the interval 90-100 °C (Figure 50a), which was noticed to increase with the imposed frequency (1-20 Hz). However, in the tensile analysis the system showed a similar frequency-dependent behaviour, but with a maximum peak at around 150-160 °C in both storage and loss moduli (Figures 49a and 49b). Moreover, the involved moduli in tension are 10 times higher than the ones measured under compression. The values of the loss modulus (Figure 49b) showed a clear relationship between the imposed frequency and the dissipated energy. Indeed, it has been shown that higher frequencies (e.g., 10 and 20 Hz) lead to dissipate more energy than lower ones. The storage and loss moduli showed a maximum value at around 250 MPa and 50 MPa, respectively (Figures 49a and 49b), which

can be attributed to the well-known collagen high tensile strength, though low strength in compression (Havaldar et al., 2014). Differently to the compressive mode the peak at approximately 200 ºC in the tensile mode showed a frequency-dependent behaviour over the temperature in tanδ curve (Figure 49c), with the increase of the imposed frequency, which clearly indicates the presence of a glass transition point. The glass transition temperature (T_g) of a polymer is a very important material characteristic to understand the material effects on mechanical behaviour, the degree of crosslinking, and the changes that occur within the bulk at a specific temperature. Despite T_g measures are very common for synthetic polymers at high temperatures, little is known about the behaviour of protein polymers (Aldred et al., 2007). The increase in tanδ peak temperatures with the imposed frequency (1-20 Hz) was used to calculate the apparent activation energy. Hence, an Arrhenius plot, in which the log of the imposed frequency is plotted against the inverse of the peak temperatures, was performed. The slope of the best-fit linearization of the obtained data corresponds to the apparent activation energy that was estimated as 780 kJ/mol. The value of the activation energy may provide important information about the degree of crosslink of viscoelastic polymers and on the nature of the molecular relaxation transitions. The observed activation energy is in the range of previously observed thermal denaturation process of collagen matrices indicating a relatively high physical entanglement of the collagen chains. The increase of tanδ is frequently associated to material degradations and to an increased mobility of the molecular chains that increase the energy consumption (Nagasawa et al., 2008). Thus, the data of the melting of the stable crystalline structure of collagen at 200 ºC suggests that the phase transition of dry collagen is more probably a denaturation than a melting of crystalline zone and the value of activation energy confirms that dry denaturation is a complex process, which probably consists in a rate-limited reversible step leading to an irreversibly denatured state of the protein (Ding et al., 2015).

In the compressive analysis (Figure 50), for the physiological temperature (i.e., in the vicinity of 37 ºC), the storage modulus (E') of the NS (Figure 50a) increases with the imposed frequency (from app. 12 MPa at 1 Hz to app. 16 MPa at 20 Hz, i.e., an increasing rate of 33%). This result is consistent with previous studies using similar frequency ranges (Schwartz and Bahadur, 2007; Tanaka et al., 2006). The loss modulus (E'') of the NS (Figure 50b) was, as expected, an order of magnitude lower than the one registered for the storage modulus over all the tested frequencies (from app. 1.4 MPa at 4 Hz to app. 2.4 MPa at 10 Hz, i.e., an increasing rate of 71%). Differently to articular cartilage, in which restrictions caused by the bones have been referred as the reason to prevent an increase in loss modulus with the imposed frequency (Fulcher et al., 2009), the characterization performed in the present study revealed that for nasal cartilages the loss modulus varies with the imposed frequency, but

without clear relationship between oscillations and dissipated energy (the dependence was not coherent with the frequency). Previous studies have already shown that the loss modulus of the cartilage was insensitive to loading frequency under compression (Schwartz and Bahadur, 2007; Tanaka et al., 2006). This behaviour can be correlated to the hydration degree of cartilages, which was observed to be frequency-independent (at least coherently). Effectively, it seems that cartilage viscoelastic properties in unconfined compression are only triggered by the fluid mobility and structural interactions between the fiber reinforcing collagen and the surrounding matrix gel (Pearson and Espino, 2013). The analysis of the tanδ under compressive loading (Figure 50c), as a function of the temperature up to 250 °C, exhibits three relaxation peaks with different elastic behaviour. These peaks at around 120, 180, and 220 °C could be related to a second-order phase transition of the amorphous regions of collagen (app. 120 °C) and to melting of the crystalline zone of collagen (app. 200 °C) and proteoglycans (app. 220 °C) matrices within the cartilage structure, respectively (Samouillan et al., 1999; Chien, 1975). However, since in the physiological state cartilage is heavily hydrated, these peaks are very likely to be associated to the mobility of water that is bonded to the cartilage solid structure. Despite the high loss of water, the peak at 120 °C shows tanδ values ranging from 0.2 to 0.3, which indicates that under compressive loading the system is primarily elastic at this temperature, presenting a small, though not negligible viscosity. In fact, at 120 °C the system mostly adsorbs energy as it undergoes elastic deformation (high storage modulus), while little energy is dissipated as heat (low loss modulus) (Figures 50a and 50b). The peaks at 180 and 220 °C, fundamentally associated to the water strongly bonded to cartilage, are considerably higher denoting a predominant viscous behaviour.

At 180 °C the values of storage and loss moduli (E' and E'', respectively) are very similar to each other, which indicates that almost all the applied energy is dissipated as heat, with an increase in viscosity of the material (Zhou et al., 2014; Lang et al., 2009). At higher temperatures (app. 230 °C) a sharp drop of the tanδ is observed due to proteins denaturation (Pietrucha, 2007).

The observed differences between tensile and compressive modes can be attributed to different properties that control the viscoelastic cartilage performance. The unconfined compressive mode of action tested in this work is clearly ruled by a flow-dependent mechanism caused by the frictional force of the interstitial fluid (fluid pressurization) that flows within the porous cartilage matrix. Moreover, the increase in compression of cartilage matrix results in a higher tissue density, which reduces the frequency dependence. A small contribution can also be attributed to tensile strains that develop within the collagen-proteoglycan matrix in radial and circumferential directions (Park et al., 2004). Tensile mode of action is instead ruled by a flow-independent mechanism produced by the time-dependent

deformability of the solid cartilage matrix that is strongly frequency-dependent (Jeng et al., 2013), showing a clear glass transition point at around 200 °C.

3.2.4 DMA: Creep-recovery Tests

It is well-known that cartilage tissues exhibit a transient response due to interactions of collagen fibres, proteoglycans (PGs), and water movements throughout the matrix (Barthelemy et al., 2016; Li et al., 2008). As referred in section 1.6.1 (and proved in section 3.1.5 with porcine samples), when the stress is held constant, the resulting strain increases along time towards an asymptotic value (i.e., a steady-state strain) (Li et al., 2008).

This section aims at investigating the time-dependent behaviour of nasoseptal cartilages (NS), concerning the location from which they were harvested: one from the bony septum (posterior part of the quadrilateral cartilage, QLC); And another from the cartilaginous septum (anterior part of the QLC) (section 1.2).

Data fitting to a general Kelvin-Voigt model was carried out to estimate time-dependent parameters. Moreover, insights into the contribution of tissue's structure is addressed since some microstructural mechanisms might be activated.

To our knowledge, creep-recovery experiments have been performed mostly in articular cartilage under short-term loading conditions, e.g., 300 s for aortic valves (Anssari-Benam et al., 2011b) or 900 s for intervertebral discs, both under compression (Barthelemy et al., 2016). The reason for these short loading periods is that cartilage strains occur mainly within a very short period of time (few seconds) of the loading process, after which cartilage continues to deform under lower creep rate. When loading time becomes excessive, also unwarranted strains begin to occur, which likely induce failure either on the surface, over-stretching subcutaneous layers, or in depth, breaking up some collagen fibrils (Halonen et al., 2014) (visible in Figure 36c). This was the reason why a maximum creep time of around 3000 s was chosen in this study (for specimen #2).

Figure 51 shows typical creep curves (true strain normalized by the imposed true stress value of approximately 0.7 MPa) of human nasoseptal cartilages: specimen #1 from the cartilaginous septum and specimen #2 from the bony septum region.
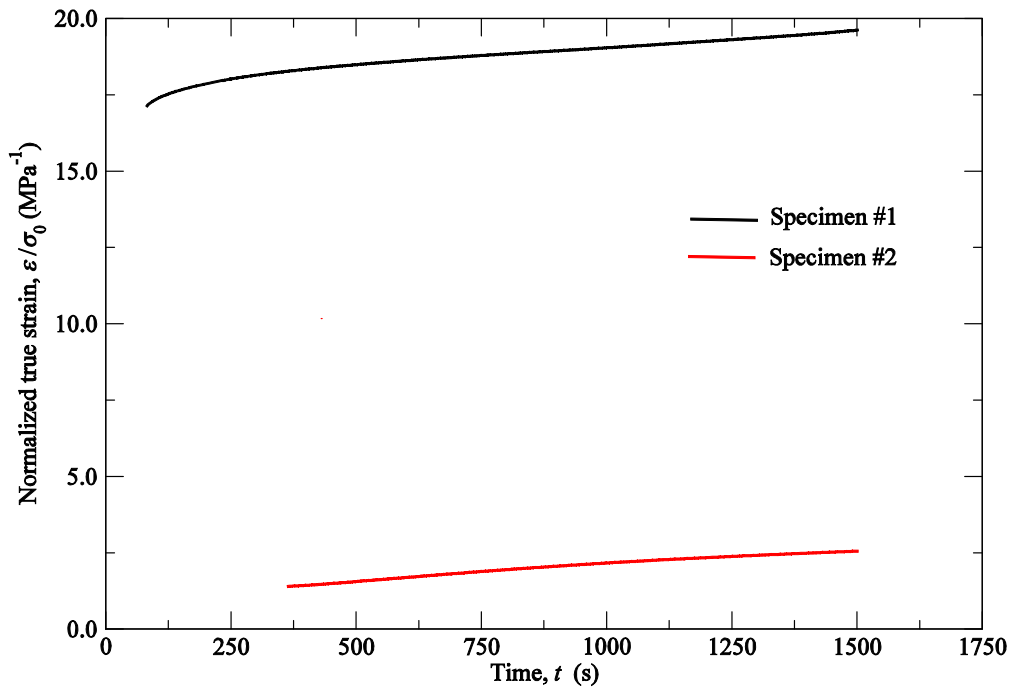
Figure 51: Comparison of creep behaviour shown by specimens #1 and #2 up to 1500 s.

Specimen #1 revealed an instantaneous normalized true strain value of about 17.5 MPa^{-1} (glassy compliance), followed by a successively higher deformation from 125 s to 1500 s under approximately constant creep rate (Figure 51). The normalized deformation was gradually build up until 19.5 MPa^{-1} (rubbery compliance), time from which a typical plateau region will be likely more pronounced (Roylance, 2001). By definition, glassy compliance is the material's initial strain corresponding to its elastic deformation due to fibres recruitment and/or rearrangements (or fluid pressure load carrying capability if it is under compression); Rubbery compliance is the equilibrium deformation corresponding to the material's rubbery extension (Li et al., 2008; Roylance, 2001). For specimen #2, the glassy compliance was approximately 1.3 MPa^{-1} (Figure 51). A typical rubbery compliance was not observed.

Typical creep curves for general soft tissues, such as articular cartilage (Schmidt et al., 1990), ligaments (Thornton et al., 2001), and aortic valves (Anssari-Benam et al., 2011b) may exhibit three distinct moments: (a) Primary creep, in which the curve is concave down; (b) Secondary creep, in which deformation is approximately proportional to time; And (c) tertiary creep, in which deformation increases exponentially until creep rupture occurs (not shown here) (Novitskaya et al., 2014; Lakes, 2009; Schmidt et al., 1990).

In this study, both specimens have shown typical creep behaviours. For specimen #1, primary creep dominated the first 500 s. Secondary creep was registered approximately from 500 s to 1500 s. The creep-compliance at 500 s was around 18.3 MPa^{-1} and at 1500 s was slightly above 19.5 MPa^{-1}.

Although secondary creep is almost represented by a straight line, it does not mean that the material behaves as a linearly viscoelastic one. Effectively, linear viscoelasticity reflects a linear relationship between stress and strain at any given time (Lakes, 2009), and thus, if the stress is increased the corresponding strain will proportionally increase too. For other stress magnitudes (not tested in this work), cartilage creep behaviour may not be linear. Further investigations to assess creep dependency on the applied stress must be performed.

Specimen #2 did not show an instantaneous strain at the initial loading time (Figure 51). Hence, the value of K_0 (Equation 1.9) is substantially lower for specimen #2 than for specimen #1, which indicates a less pronounced instantaneous elastic response. Despite the time of the experiment (3000 s) has been significantly higher for specimen #2 (Figure 53) than for specimen #1 (Figure 52), the transition between primary and secondary creep moments were less defined. Primary creep in specimen #2 was verified up to 1500 s, while a secondary creep was registered from around 1500 s to 3000 s. The normalized true strain at 1500 s was approximately equal to 2.5 MPa^{-1}, and slightly above 3 MPa^{-1} at 3000 s. Creep recoveries were not shown.

Data fitting to Kelvin-Voigt model (Equation 1.9) shown in Figures 52 and 53 yielded a correlation coefficient of 0.997 and 0.999 for specimens #1 and #2, respectively.

Chi-square = 0.968468
Correlation coefficient = 0.996886
RMS per cent error = 0.00239335

$J(t) = 1/19.326 + 1/0.0573782[1-e^{(-t/25.4687)}] + 1/0.344272[1-e^{(-t/1239.50)}]$
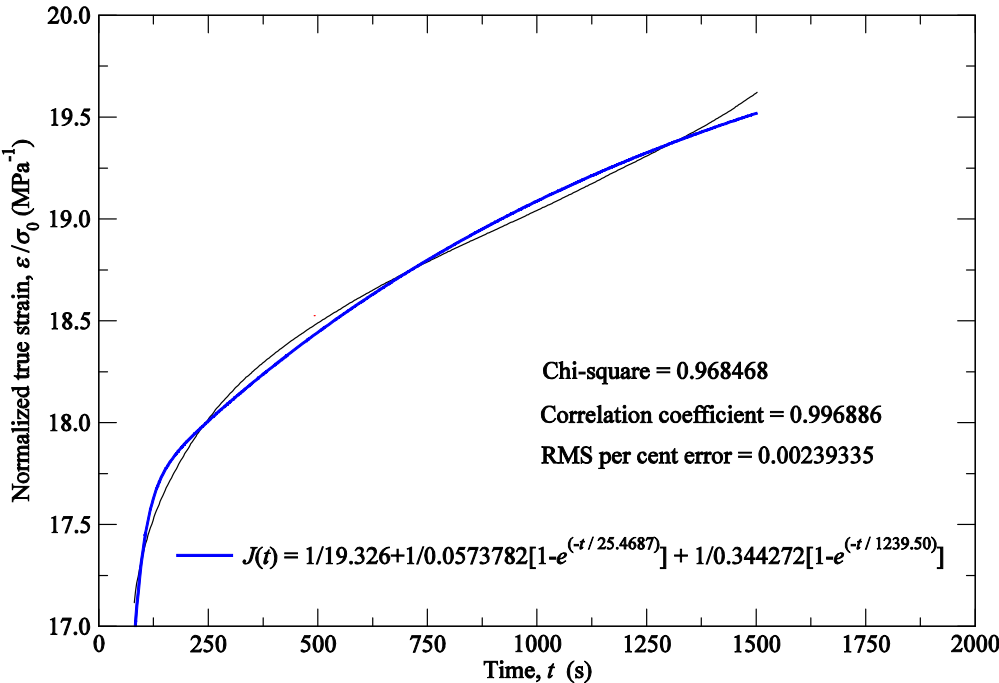
Figure 52: Data fitting of the experimental creep curve for specimen #1 (anterior part of the QLC).

$$J(t) = 1/1.45891+1/98.0968[1-e^{(-t/0.0002)}] + 1/0.377078[1-e^{(-t/1245.51)}]$$

Chi-square = 0.0558107
Correlation coefficient = 0.999867
RMS per cent error = 0.00403085
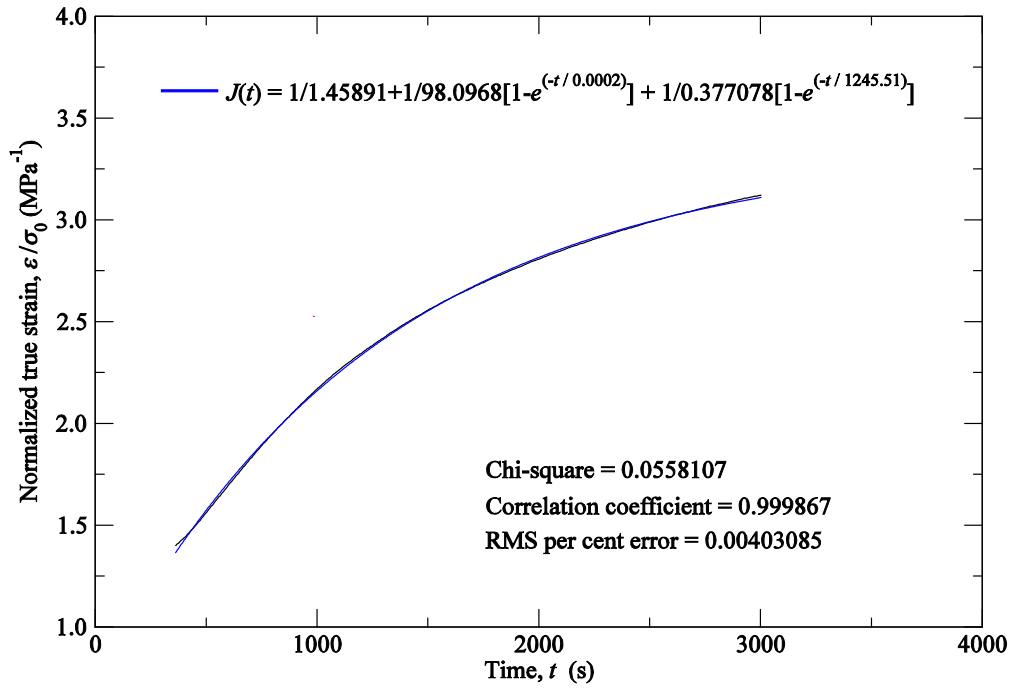
Figure 53: Data fitting of the experimental creep curve for specimen #2 (posterior part of the QLC).

Tables 11 and 12 resume the non-normalized creep viscoelastic time-dependent parameters determined by the Kelvin-Voigt model for specimen #1 and specimen #2, respectively.

Table 11: Creep time-dependent parameters of specimen #1 (anterior part of the QLC), according to Equation 1.9.

Constitutive parameter	Fitting value
K_0	15.499
K_1	0.046
K_2	0.276
τ_1 [s]	25.469
τ_2 [s]	1239.5

Table 12: Creep time-dependent parameters of specimen #2 (posterior part of the QLC), according to Equation 1.9.

Constitutive parameter	Fitting value
K_0	1.024
K_1	68.864
K_2	0.265
τ_1 [s]	0.0002
τ_2 [s]	1245.5

The retardation times were obtained by applying two model branches of the Prony series (Equation 1.9). It was verified a drastically increase from τ_1 to τ_2, giving the idea that a steady state is likely to occur above τ_2. The strain magnitudes were also considerably different concerning the sample location. Specimen #1 from the cartilaginous septum, which is located caudally to the nasal pyramid and closer to S-area (section 1.2), had more flexibility. Specimen #2 from posterior part of the QLC presented higher stiffness.

According to multi-frequency dynamic results from DMA, at 1 Hz, which mimics the quasi-static physiological condition, the storage and loss moduli did not register any significant variation between 20-40 ºC (Figures 49 and 50). Hence, the chosen temperature range (23±1 ºC) in this study is compatible with the physiological temperature of soft tissues (about 37 ºC). Besides, it was faster to achieve, easier to stabilize, and less aggressive, avoiding over-dehydration of cartilage surface. The applied force was calculated for each specimen according to their cross-sectional areas (787 mN and 1240 mN, respectively) in order to maintain the same stress magnitude of about 0.7 MPa.

Regarding linear biphasic theories, different phenomena might be activated to explain the viscoelastic creep response in soft biological materials. The first one is the frictional drag of the interstitial fluid throughout the porous-permeable ECM (Joshi et al., 1995). When the force is applied, the initial elastic deformation of the matrix is followed by a compliance behaviour as PGs bound water moves into free spaces. When the force is removed, osmotic swelling pressure increases, and PGs tend to re-imbibe water attaining a new equilibrium (Gu and Li, 2011). Consequently, as reported in previous studies (Julkunen et al., 2007), mechanical properties change with these microscopic structural variations. Some authors (Li et al., 2008) believe in other reasons to justify this type of transient response. Besides fluid pore pressure variations, collagen fibres are continuously recruited along time (Li et al., 2008). Some fibres can be oriented through the loading direction and others cannot, presenting a tendency to rearrange later (Li et al., 2008; Li et al., 2005). Actually, cartilage uniaxial creep test is just a simplified mechanism to assess viscoelastic properties of an isolated deformation response, without the compounding effects of other directions. Aiming at reducing fibre arrangement effects, some studies pointed out the need of preconditioning, which could be determinant to attain reproducible results. Preconditioning is a pre-testing step, in which one applies a certain number of loading-unloading cycles (Einat and Yoram, 2009; Carew et al., 2004). It involves a pronounced softening that reduces the hysteresis effect, even in quasi-static experiments. After some cycles, the response stabilizes and approaches a steady state (Holzapfel et al., 2000; Fung, 1993). However, the mechanical response of human tissues during any clinical practice corresponds to a natural state rather

than a preconditioned state. Changes in the mechanical behaviour of soft biological tissues associated to preconditioning cycles are related to microstructural alterations and internal rearrangements, either of fibre directions or new disposition of other solid components, which are associated to dissipation of material's energy (Ehret and Itskov, 2009; Nava et al., 2004). This dissipative behaviour in early cycles might be significant for realistic modelling of soft biological tissues, and thus, should be considered (Nava et al., 2004).

Nevertheless, as an additional test, a porcine auricular cartilage specimen was strained up to 20 and 40% of the prescribed force before it was held constant. The results were not significantly different from those achieved with non-preconditioned specimens, registering a maximum true deformation of around 17%. Despite slightly variations in the instantaneous strain level, experimental data showed that specimens consistently attained an equilibrium state within the estimated relaxation times, suggesting that previous loading history did not produce a noticeable constrain on the specimen recovery.

To sum up, creep response is controlled by the fluid flow and collagen-PGs interactions within the ECM (Barthelemy et al., 2016). The viscous components of collagen fibres primarily control the initial compliance and fluid flow affects creep rate as cartilage continues to deform (Halonen et al., 2014). In a parametric study, Halonen et al. (2014) proved that collagen fibrils stiffness changing shifted the creep curve drastically, and thus, it could change the transient short-term cartilage response (of the knee). On the other hand, the non-fibrillar matrix (mainly the effect of PGs and water) alters creep rates and controls the long-term time points until the equilibrium is achieved.

Thornton et al. (2001) also found that there is a striking difference between fibre recruitment during creep and lack of recruitment during relaxation. At the initial (instantaneous) step, some fibres become immediately straightened, while others remain crimped. The subsequent stress redistribution over a successively large number of fibres (non-linear recruitment) contributes to moderate creep (Thornton et al., 2001). This takes much more time than the first compliance, and thus, the second retardation time is usually much longer. The permeability of soft tissues plays also an important role, especially at the early stage of the experiment when creep rate is the highest (Julkunen et al., 2007; Schmidt et al., 1990). These facts have undoubtedly proven that different internal mechanisms are activated during creep experiments in soft biological tissues.

3.2.5   DMA: Stress-relaxation Tests

Stress-relaxation experiments were conducted by applying a constant displacement of 0.8 mm in two nasoseptal cartilage specimens harvested from the caudal and cephalic nasal areas. Experimental

curves were fitted to a general Maxwell model (Equation 1.12) giving some insights into the microstructure and internal activated mechanisms. Typical normalized curves are shown in Figure 54.
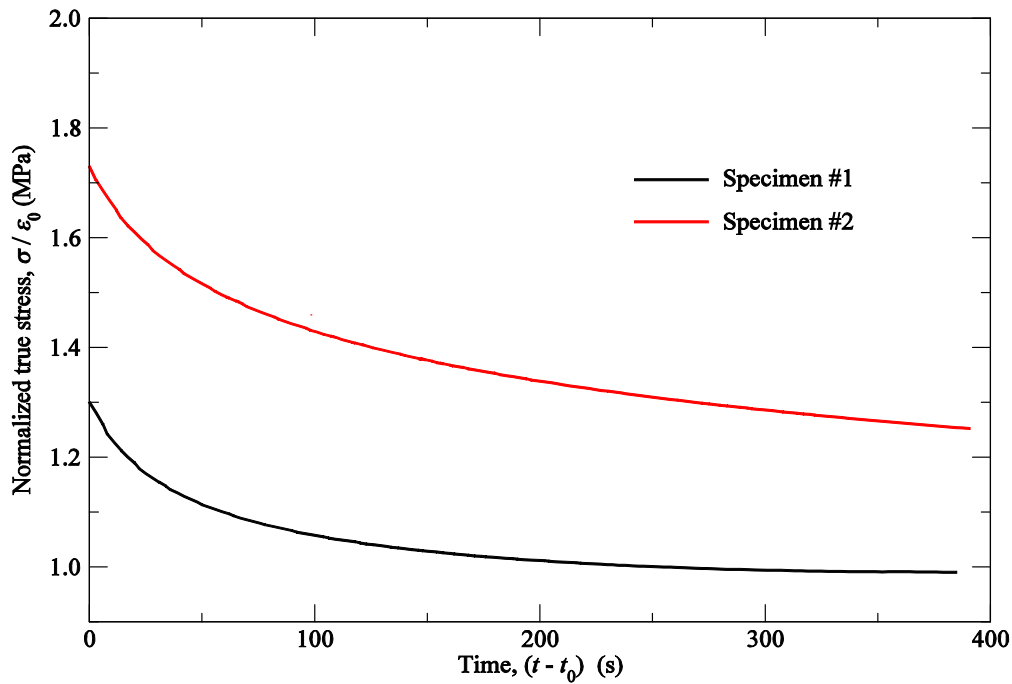
Figure 54: Comparison of the relaxation phase for specimens #1 and #2 up to 400 s.

Typical normalized relaxation curves were presented for an elapsed time of 400 s (Figure 54). At short loading times, the highest stress intensity, corresponding to a glassy modulus, falls exponentially to a lower equilibrium rubbery modulus, as the solid matrix gradually accommodate the strain, as long as the conformational extension takes place (Roylance, 2001). Specimen #2 showed higher stress intensity (1.7 MPa of normalized true stress) at $t = t_0$ comparing to the one obtained for specimen #1 (1.3 MPa of normalized true stress). Since both specimens were harvested from human male donors of about the same age and cross-sectional areas were also very similar (1.987 mm^2 and 1.931 mm^2, respectively), this result may be related to structural composition and molecular organization regarding specimen location.

Experimental data was fitted to a general Maxwell model (Equation 1.12) with two branches, providing the results shown in Figures 55 and 56 for specimen #1 and specimen #2, respectively. Modelling specific differences to reproduce relaxation curves is not always easy. Hence, one must adequate the number of model branches to predict accurately the time-dependent material parameters. For instance, Anssari-Benam et al. (2001b) reported the necessity of using one single mode to describe stress-relaxation of aortic valves for strains below 5% of strain at failure, and a double mode for higher

strain increments in circumferential directions. As shown in Figures 55 and 56, an excellent agreement has been accomplished with two branches, which allowed attaining a correlation coefficient of about 0.999 in both cases.

$$R(t) = 0.986142 + 0.113088\,e^{(-t/18.2486)} + 0.202651\,e^{(-t/96.1366)}$$

Chi-square = 6.15739×10^{-5}
Correlation coefficient = 0.999950
RMS per cent error = 0.000643895
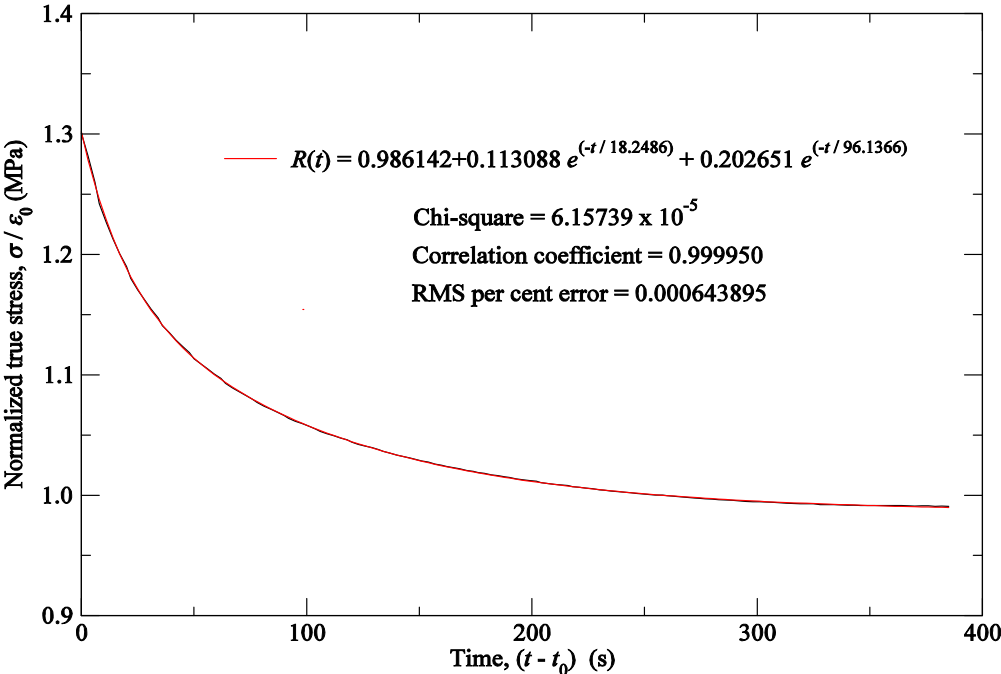
Figure 55: Data fitting of the experimental relaxation curve for specimen #1 (anterior part of the QLC).

$$R(t) = 1.07244 + 0.256508\,e^{(-t/51.2784)} + 0.38434\,e^{(-t/519.298)}$$

Chi-square = 0.00187254
Correlation coefficient = 0.999792
RMS per cent error = 0.00194756
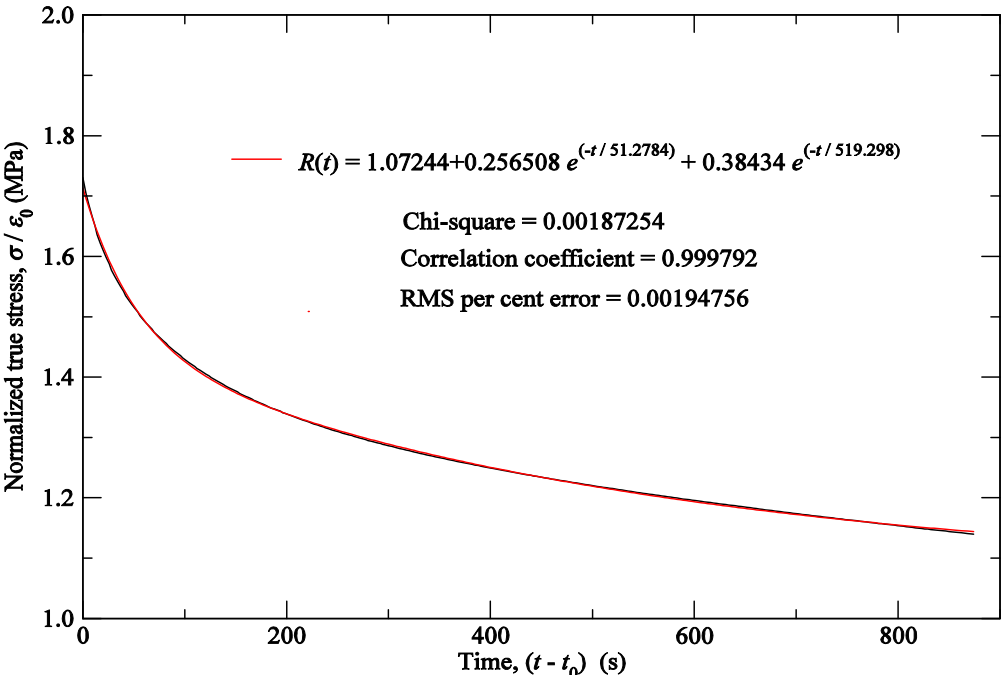
Figure 56: Data fitting of the experimental relaxation curve for specimen #2 (posterior part of the QLC).

Tables 13 and 14 present the estimated non-normalized discrete viscoelastic parametric values.

Table 13: Relaxation time-dependent parameters of specimen #1 (anterior part of the QLC), according to Equation 1.12 (unities as represented in Figure 55).

Constitutive parameter	Fitting value
K_0	0.063
K_1	0.007
K_2	0.013
τ_1	18.249
τ_2	96.137

Table 14: Relaxation time-dependent parameters of specimen #2 (posterior part of the QLC), according to Equation 1.12 (unities as represented in Figure 56).

Constitutive parameter	Fitting value
K_0	0.082
K_1	0.020
K_2	0.030
τ_1	51.278
τ_2	519.298

Two relaxation times were identified as "fast" and "slow". The increased relaxation time indicates a clear retardation in the recovery process that are related to different behaviours of the matrix molecules.

It is well-accepted that the relaxation behaviour is mostly influenced by the presence of water, especially in the ramp phase, whereas collagen fibres directly affect the peak stress during ramp. Thus, specimen #2 must present higher collagen content concerning its cephalic location in the QLC (or at least higher portion initially aligned in the loading direction) regarding its stiffer response. As so, more fibres were loaded in specimen #2 at the application of the instantaneous displacement, which agrees with the findings of Fung (1993). Earlier studies have been emphasizing the role of PGs in the following equilibrium response (Julkunen et al., 2008).

Besides structural influence of the elastin and GAGs content that takes place immediately after loading, the necessity for a double exponential decay (Anssari-Benam, 2014; Screen et al., 2013) is related to the initial collagen fibres recruitment, together with crimped portions, which are orthogonally

oriented in a direction different from that of the loading action or will not stretch. Because the deformation does not change over time, the measured behaviour will solely be that of the initially recruited fibres (Julkunen et al., 2007; Thornton et al., 2001).

Further, it was previously shown that sliding and reorganization of the stretched fibres is a mechanism of relaxation, e.g., in human ligaments and tendons (Screen et al., 2013; Anssari-Benam et al., 2011b; Gupta et al., 2010; Purslow et al., 1998; Mijailovich et al., 1993), which might also happen in NS. Moreover, due to its multilaminar collagenous architecture, water is free to move in a wide range of combinations and the relaxation will vary accordingly (Barthelemy et al., 2016). To understand better the nature of the active mechanisms in time-dependent relaxation response, further microstructural studies must be performed, including at the cell level, since the organization and distribution of the chondrocytes implicate the activation of certain mechanisms that could influence the viscoelasticity of soft biological tissues as well.

Despite the temperature has been held constant (23±1 °C) in this study, dehydration is likely to occur during the experiments. Thornton et al. (2001) did not find significant variations in water content after relaxation for medial collateral ligaments. However, in the present work, dehydration was not negligible and therefore played an important role. Despite the efforts developed during the specimen preparation, storing, and stabilizing before testing, nor a direct control on the fluid flow out of the matrix, neither on water loss along cartilage surface has been exerted. Consequently, water content changing might undoubtedly induce some non-linearities both in creep and relaxation responses. Moreover, fluids will obviously flow faster in high permeability zones then within the remaining ones. Since these spaces are slightly changing over time, the rate of relaxation will also vary (Screen et al., 2013; Julkunen et al., 2007).

The present study suggests that there are specific mechanisms that take place in stress-relaxation responses that look similar to the ones that act in creep. Nasal cartilages relaxation is associated to some intrinsic viscoelastic properties of the fibre-reinforced collage-PGs matrix and generated frictional forces that resist to an eventual collagen rearrangement in tension. At small strain and stress intensities, the frictional resistance between collagen and PGs can be strong enough as to maintain an approximately linear behaviour (Schmidt et al., 1990). Besides, by comparing both damper characteristic times, it is possible to conclude that the equilibrium state was attained faster in the relaxation (response) than in creep. This is the reason why the characteristic time of creep is called retardation (Roylance, 2001; Akisuki et al., 1986).

3.3 Numerical Simulations of the Nasoseptal Cartilages in Creep and Stress-relaxation

A set of fundamental simulations was conducted in order to gain some insight into the sensibility of each parameter on time-dependent responses both in creep and relaxation. The initial state of the specimens was barely known concerning the parameters that were not obtained by curve-fitting. Hence, the ECM isotropic parameters were unknown, the initial orientation of the collagen fibres and their stress-like related parameters were also unknown, and data on tissue's permeability was not available. Therefore, some reference values from other similar tissues were incorporated in the numerical models, as the initial state of the nasoseptal cartilages (Table 3).

The initial values were successively adjusted until the simulations provide an acceptable agreement with the experimental time-dependent responses. Since the unicity of individual constitutive parameters is not guaranteed, it is believed that the current combination of ten material parameters is valid.

Table 15 presents the final values of the creep numerical results and Figure 57 reveals the best numerical-experimental agreement that has been achieved for creep test of specimen #1.

Table 15: Constitutive parameters used in creep simulation for specimen #1.

Constitutive parameters		Final values	Equations
Isotropy	C_{10}^{MR} [MPa]	0.75	2.33
	C_{01}^{MR} [MPa]	0.02	2.33
Anisotropy	k_1 [MPa]	10.0	2.34
	k_2	2.5	2.34
Permeability	k_0 [m^4.N^{-1}.s^{-1}]	1.99E-15	2.56
	M	7.1	2.56
Viscoelasticity	K_1	0.046	1.9
	K_2	0.276	1.9
	τ_1 [s]	25.469	1.10
	τ_2 [s]	1239.5	1.10
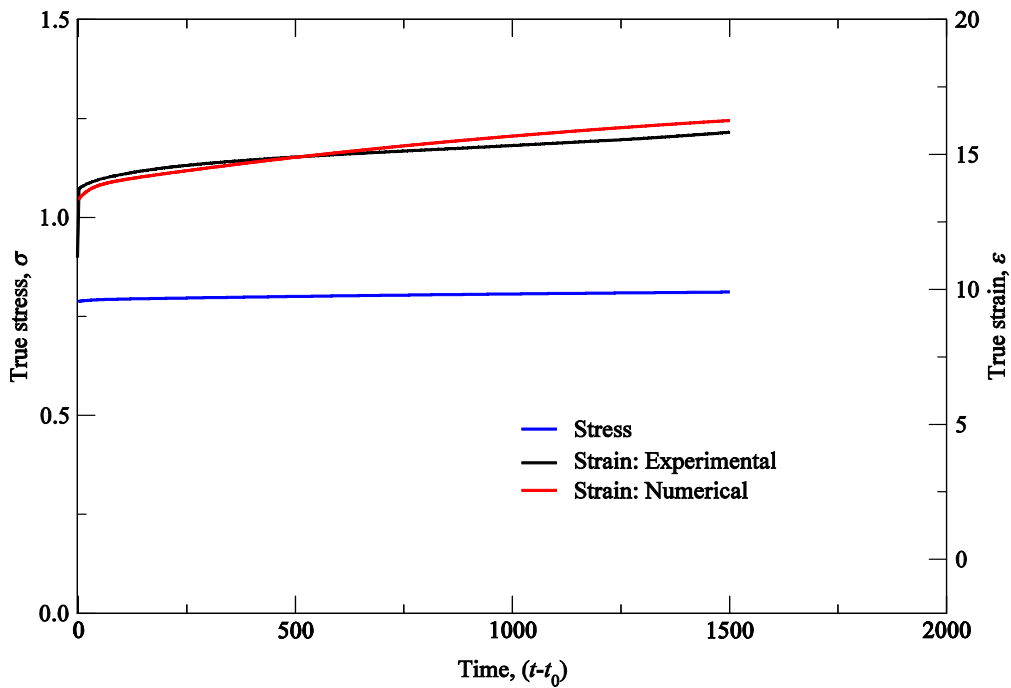
Figure 57: Numerical-experimental agreement of the creep behaviour for specimen #1 (anterior part of the QLC).

Figure 58 illustrates the imposed boundary conditions in agreement with the ones employed in the experiments for the creep tests. The loading action was imposed in two steps: (a) An instantaneous loading step (0.47 s); And (b) a holding step up to 1500 s.

The resultant (axial) force is the sum of the estimated nodal quantities over the set of nodes in one extremity, which was found equal to the applied force by the DMA equipment. The maximum displacement registered (after 1500 s) was about 1.766 mm.
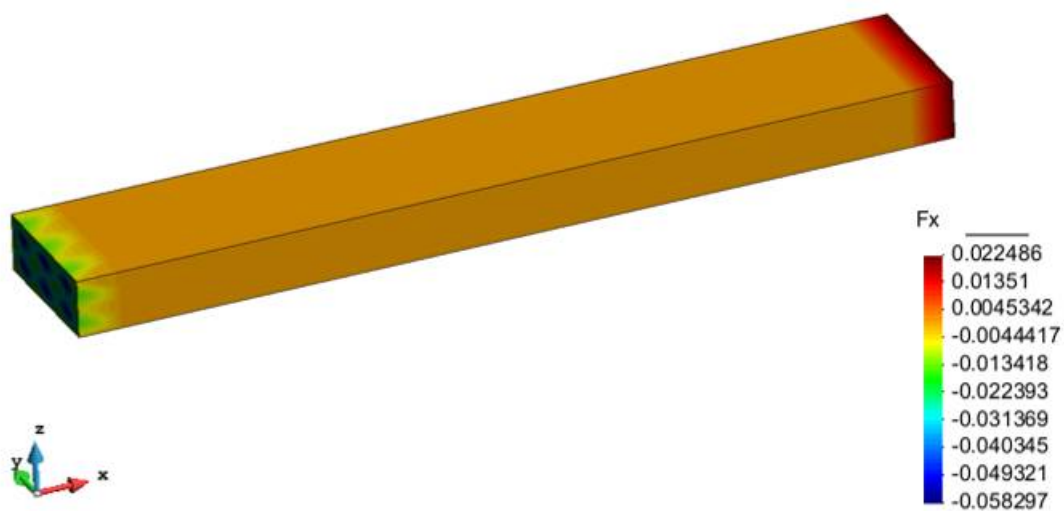
Figure 58: Representation of the loading boundary conditions (creep): equivalent nodal forces (N).

Table 16 presents the set of numerical parameters that allowed mimicking the experimental response under relaxation. Figure 59 reveals the best numerical-experimental agreement that has been obtained for relaxation using specimen #1.

Table 16: Constitutive parameters used in relaxation simulation for specimen #1.

Constitutive parameters		Final values	Equations
Isotropy	C_{10}^{MR} [MPa]	0.15	2.33
	C_{01}^{MR} [MPa]	0.011	2.33
Anisotropy	k_1 [MPa]	7.5	2.34
	k_2	1.0	2.34
Permeability	k_0 [m⁴.N⁻¹.s⁻¹]	1.99E-15	2.56
	M	7.1	2.56
Viscoelasticity	K_1 [MPa]	0.007	1.12
	K_2 [MPa]	0.013	1.12
	τ_1 [s]	18.249	1.13
	τ_2 [s]	96.137	1.13
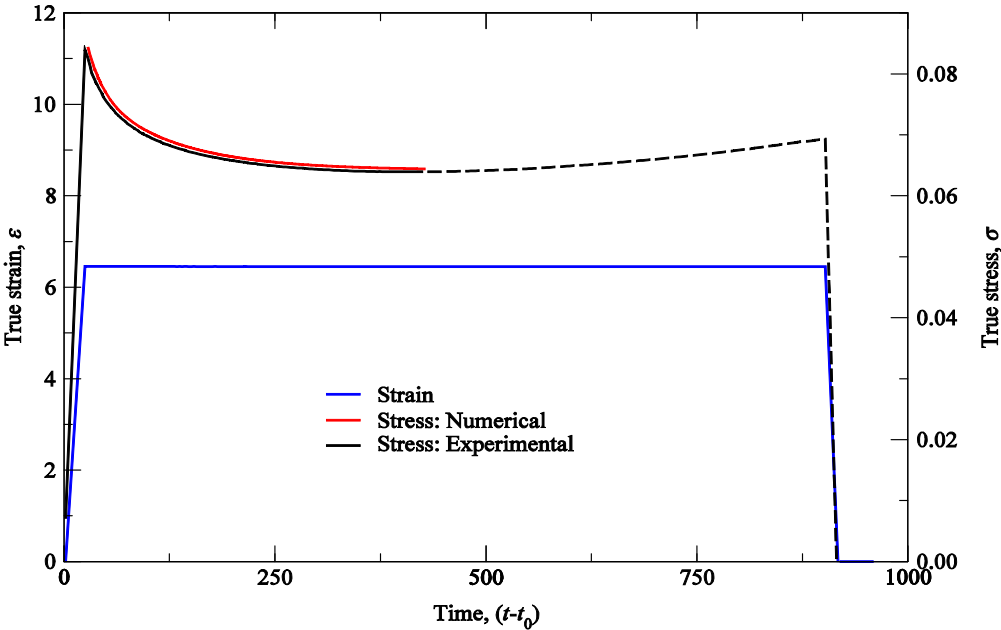
Figure 59: Numerical-experimental agreement of the relaxation behaviour for specimen #1 (anterior part of the QLC).

The correct definition of the boundary conditions is once again fundamental to accurately simulate the relaxation behaviour of the specimen (specimen #1).

Figure 60 illustrates the applied boundary conditions, in compatibility with the experimental relaxation test. In this simulation, the loading (displacement) was imposed through an instantaneous displacement of 0.8 mm in an extreme section for 400 s, while the attained force (after 0.48 s) has been monitored (157 mN was the maximum registered).
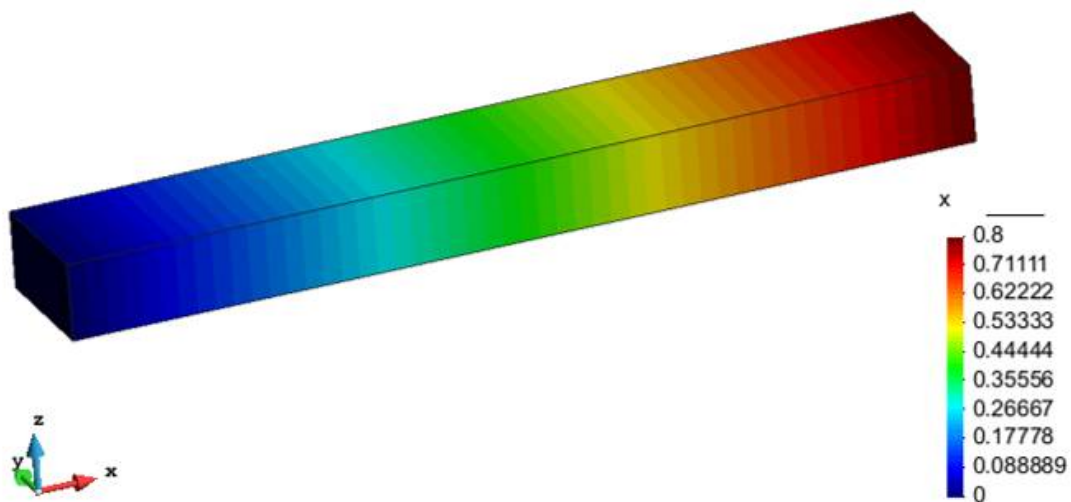
Figure 60: Representation of the boundary conditions (relaxation): displacement field (mm) in the loading direction.

The values used for the permeability parameters were the same for both viscoelastic features because the samples were extracted from the same nasal region (anterior part of the QLC). Actually, the apparent permeability is well-accepted as long as it is in the range of 10E-13-10E-16 $m^4.N^{-1}.s^{-1}$ (Reynaud and Quinn, 2006; Holmes and Mow, 1990; Mak, 1986). Such low permeabilities mean that large frictional drag forces are exerted by the interstitial fluid as it flows through the matrix. However, this study did not account for dissociating the water trapped between collagen fibres (intra-fibrillar water) from other portions (extra-fibrillar water) (Barthelemy et al., 2016). Further attempts must be done on this topic in a near future.

The most relevant variables in these agreements were the Mooney-Rivlin isotropic parameters, shifting the curves in the Y-axis with small variations (± 10% of the reference values). The modifications induced by the anisotropic constitutive parameters were less significant with no changes in a given domain (± 50% of the reference values). These conclusions were taken from a brief parametric study.

"If you want to explain yourself, you must present something tangible"

Joseph Beuys

CHAPTER 4

Concluding Remarks

This chapter summarizes the fundamental outcomes of this dissertation, being accomplished a small critical review of the author. Additionally, further investigations for the improvement of experimental protocols and numerical simulations are suggested, which will increase the complexity of the FE mesh. Moreover, the consideration of the material microstructure will allow modelling the mechanical behaviour of the biological tissues in a more realistic way.

4. CONCLUDING REMARKS

The literature review endorsed the cartilage as a very complex porous-permeable tissue that contains solid (type II collagen and proteoglycans, PGs) and fluid materials. In compression, cartilage behaves like an isotropic solid because collagen fibres are not stretched (do not respond due to their high length to diameter ratio). Load distribution is conducted through the movement of free interfibrillar water within the incompressible matrix. On the other hand, in tension, collagen fibres are recruited and stretched to resist under extension. Cartilage transient response depends essentially on the harvesting locations, fibres architecture, and loading direction that contribute for a noticeable anisotropic behaviour.

However, prior to numerical modelling, one must know what kind of response cartilage is likely to produce. Thus, experimental protocols were repeatedly tested and reformulated using porcine auricular cartilages (PAC) to establish a final protocol to be applied to nasal cartilages.

The quasi-static mechanical behaviour of PAC has shown to be highly anisotropic, reflecting a complex collagen fibre kinematics. As briefly explained, this may be attributed to gradual recruitment and alignment of collagen fibres and their increasing role in load bearing capacity, which was a good indicator that PAC specimens are suitable to validate creep and relaxation experimental protocols. Hence, Differential Scanning Calorimetry (DSC), Thermogravimetric Analysis (TGA), and Dynamic Mechanical Analysis (DMA) have been also considered essential analyses to undergo a comprehensive mechanical characterization of nasal cartilages tissues, namely the nasal septum (NS), upper lateral cartilages (ULC), and lower lateral cartilages (LLC).

Regarding thermal features assessed by DSC and TGA, a lot of variability was found for NS, ULC, and LLC. However, the variability appears to be intrinsic to own tissues. Concerning the DSC analysis, it must be highlighted that a consistent peak occurred for all the samples between 100 °C and 130 °C due to water evaporation. The distinction between free and trapped water showed to be significant in these results. In general, a higher temperature peak was detected in subcutaneous tissues comparatively to cartilages, being attributed to their higher water-binding capacity that results in higher difficulty for water to move out from the tissues (this conclusion is also supported by TGA). Moreover, the consistent narrow peaks of the subcutaneous tissues may induce different mechanisms of water-binding, and consequently, distinct corresponding viscoelastic behaviours. In TGA, the degradation curves of cartilage, composite, and subcutaneous tissue from NS, ULC, and LLC specimens, occurred in three well-defined stages, being the first between 24.7 °C and 169.3 °C, on average (water loss), with

a main peak at around 36.5 ºC, the second between 156.0 ºC and 213.6 ºC, on average (small, but consistent, perhaps related to tightly bounded water), and finally, the third in the range of 209.9-484.9 ºC (degradation of proteins). They all converged to a final state from which the dried residues were calculated. The residues variably changed from 8.2 wt% to 19.5 wt% (on average) up to 500 ºC. An important conclusion from this thermal analysis is that the water content of nasal cartilages was estimated to be around 42% (on average) of the net weight, differently from other well-known hyaline cartilages. However, it must be emphasised that this value showed high scatter (coefficient of variance, CoV: 33%), presenting values in the range of 28.9-57.7 wt%.

Tensile and compressive DMA results of the NS showed obviously different behaviours. In tension, the viscoelastic performance of NS was ruled by a flow-independent mechanism produced by the solid matrix, which is strongly frequency-dependent presenting a clear glass transition point at around 200 ºC. Moreover, a set of secondary frequency-independent relaxation peaks in the range of 70-100 ºC was registered due to melting of crystalline regions of collagen. Both conclusions were taken from the variation of the tanδ curve (the ratio of the loss to storage moduli) over the temperature (up to 250 ºC). Under unconfined compression, three relaxation peaks (at 120 ºC, 180 ºC, and 220 ºC) were registered through tanδ curve associated to a second-order phase transition within the amorphous region of collagen, and to melting of crystalline zones of collagen and proteoglycans matrices, respectively. However, since cartilage is also rather hydrated, these peaks can also be related to water mobility within the cartilage structure. In fact, under compressive loading, the material is ruled by a flow-dependent mechanism caused by the frictional forces of the interstitial fluid that flows throughout the matrix. Also, the increase in tissue density under compression reduced somehow the frequency dependence mainly of the loss modulus. In dynamic analysis, the hydration of the specimens prior and during the experiment could be very important. DMA was performed with no internal bath and samples were directly stored in a freezer after dissection to preserve their natural turgidity. Therefore, a detailed protocol should be developed to assess this topic – a future study to evaluate the effects of hyper-hydration on viscoelastic behaviour of nasal cartilages, comparing the results of naturally turgid specimens with others that had been stored in an isotonic solution and/or buffered during the experiments – to make deeper conclusions.

The basic features of viscoelasticity (creep and relaxation) were also evaluated. It is well-accepted that small differences in length and shape can occur due to tissue loss during dissection that may affect the reproducibly of the results. However, the most important factors were the region of harvesting and the orientation of the specimens, concerning the whole structure.

The present study suggests that there are different activated time-dependent mechanisms in creep and stress-relaxation. Moreover, the location from which specimens were harvested was paramount to understand their mechanical transient responses. The specimen from anterior part of the quadrilateral cartilage (QLC) presented higher glassy compliance, followed by a successively higher deformation under constant creep rate, until a rubbery compliance took place. It was shown that cartilage strains occurred at the first seconds of the experiment and at a given point it tends to a plateau. On the other hand, in the specimen from posterior part of the QLC, the glassy compliance was much lower, and no rubbery compliance was clearly observed. As an explanation, creep response was due to collagen-PGs interactions and the fluid flow. The viscous components of the collagen fibres primarily controlled the initial compliance and the fluid flow affected posterior creep rate as cartilage continued to deform. Besides fluid pore pressure variations, collagen fibres were continuously recruited and rearranged along time increasing drastically the damper characteristic times.

Concerning the relaxation aspects at short loading times, the glassy modulus fell exponentially to a lower equilibrium rubbery modulus for the specimens from anterior and posterior part of the QLC (the second specimen presented obviously a higher initial stress intensity). The relaxation was mostly influenced by the presence of water, especially at the ramp phase, and collagen fibres affected directly the peak stress. Since the deformation has not changed over time, the measured behaviour has reflected the initially recruited set of fibres, as no further recruitments took place. It was concluded that further microstructural studies must be performed to understand the relaxation phenomena in more detail, including at the cell level, since the organization and distribution of the chondrocytes can also determine the activation of certain viscoelastic mechanisms. It was concluded that the relaxation moves toward its equilibrium faster than creep, leading to lower damper characteristic times.

The permeability was held constant during both creep and stress-relaxation experiments. However, a more comprehensive study could be interesting on this topic, since the permeability is a paramount aspect on the fluid flow, which affects directly the cartilage ability to redistribute loading under compression and to reach a new equilibrium in tension.

In order to achieve valid numerical results, the nasal structures should be accurately modelled. Despite a complete nasal structure (with nasal bones and soft tissues) has been fully segmented from CT-scans, only a set of basic creep and relaxation simulations were successfully performed. Those studies were based on a previously developed hyper-viscoelastic mathematical formulation that describes all the constitutive laws, through the V-Biomech, a home-developed finite element (FE) solver for general incompressible soft biological materials. The commercial solvers are powerful tools with

multiple solutions and a large community of users, which means that there are also multiple sources of information to solve any doubts. However, the outcomes presented here proved that a home-developed FE solver can equal the performance of commercial FE packages.

Creep and stress-relaxation agreements were obtained with respect to the imposed boundary conditions, with a fairly reasonable accuracy. However, this process resulted from an iterative procedure that was very time consuming and did not assure the unicity of the attained solution (or even the global optimum). Therefore, an optimization algorithm could be very useful to determine the constitutive parameters aiming at reproducing the experimental outputs in a very effective way. Even though, since the unicity of individual parameters was not verified, it is believed that the presented combination is valid. The most important constitutive parameters within the numerical-experimental agreements were the Mooney-Rivlin isotropic constants.

In resume, the numerical simulations through Finite Element Models (FEM), using V-Biomech, showed their validity and potential to contribute to the understanding on the nasal structures biomechanics, even at higher complexity.

Finally, one should undoubtedly recognize that this is a fascinating and promising subject. The author of this Thesis is deeply persuaded that the outcomes of this work are still very far from a full understanding of the plenitude of the mechanical behaviour of the nasal structures, both as individual entities and in the context of their interactions within a living system. Future will bring us new amazing achievements on this field of scientific knowledge.

CHAPTER 5

References

This chapter enunciates the bibliographic references consulted during the elaboration of this thesis.

REFERENCES

Adelson, R. T., DeFatta, R. J., & Bassischis, B. A. (2008). Objective assessment of the accuracy of computer-simulated imaging in rhinoplasty. American Journal of Otolaryngology, 29(3), 151-155.

Aldred, N., Wills, T., Williams, D. N., & Clare, A. S. (2007). Tensile and dynamic mechanical analysis of the distal portion of mussel (Mytilus edulis) byssal threads. Journal of the Royal Society Interface, 4(17), 1159-1167.

Akizuki, S., Mow, V. C., Müller, F., Pita, J. C., Howell, D. S., & Manicourt, D. H. (1986). Tensile properties of human knee joint cartilage: I. Influence of ionic conditions, weight bearing, and fibrillation on the tensile modulus. Journal of Orthopaedic Research, 4(4), 379-392.

Alastrué, V., Rodríguez, J. F., Calvo, B., & Doblaré, M. (2007). Structural damage models for fibrous biological soft tissues. International Journal of Solids and Structures, 44(18), 5894-5911.

Alves, J. L., Yamamura, N., Oda, T., & Teodosiu, C. (2010). Numerical simulation of musculo-skeletal systems by V-Biomech. CMBBE2010.

Anderson, J. R. (1971). New approach to rhinoplasty: A five-year reappraisal. Archives of Otolaryngology, 93(3), 284-291.

Annaidh, A. N., Bruyère, K., Destrade, M., Gilchrist, M. D., & Otténio, M. (2012). Characterization of the anisotropic mechanical properties of excised human skin. Journal of the Mechanical Behavior of Biomedical Materials, 5(1), 139-148.

Ansari, K., Asaria, J., Hilger, P., & Adamson, P. A. (2008). Grafts and implants in rhinoplasty—techniques and long-term results. Operative Techniques in Otolaryngology-Head and Neck Surgery, 19(1), 42-58.

Anssari-Benam, A. (2014). Is the time-dependent behaviour of the aortic valve intrinsically quasi-linear?. Mechanics of Time-Dependent Materials, 18(2), 339-348.

Anssari-Benam, A., Bader, D. L., & Screen, H. R. (2011a). A combined experimental and modelling approach to aortic valve viscoelasticity in tensile deformation. Journal of Materials Science: Materials in Medicine, 22(2), 253-262.

Anssari-Benam, A., Bader, D. L., & Screen, H. R. (2011b). Anisotropic time-dependant behaviour of the aortic valve. Journal of the Mechanical Behavior of Biomedical Materials, 4(8), 1603-1610.

Anssari-Benam, A., Bucchi, A., & Bader, D. L. (2015). Unified viscoelasticity: Applying discrete element models to soft tissues with two characteristic times. Journal of Biomechanics, 48(12), 3128-3134.

Arroyave, A. I., Lima, R. G., Martins, P. A. L. S., Ramião, N., & Jorge, R. M. N. (2015). Methodology for Mechanical Characterization of Soft Biological Tissues: Arteries. Procedia Engineering, 110, 74-81.

Ashrafi, A. T. (2014). Management of upper lateral cartilages (ULCs) in rhinoplasty. World Journal of Plastic Surgery, 3(2), 129.

Asran, A. S., Henning, S., & Michler, G. H. (2010). Polyvinyl alcohol–collagen–hydroxyapatite biocomposite nanofibrous scaffold: mimicking the key features of natural bone at the nanoscale level. Polymer, 51(4), 868-876.

Avanzini, A., Battini, D., Bagozzi, L., & Bisleri, G. (2014). Biomechanical evaluation of ascending aortic aneurysms. BioMed Research International.

Banks, H. T., Hu, S., & Kenz, Z. R. (2011). A brief review of elasticity and viscoelasticity for solids. Advances in Applied Mathematics and Mechanics, 3(1), 1-51.

Barthelemy, V. M. P., Van Rijsbergen, M. M., Wilson, W., Huyghe, J. M., Van Rietbergen, B., & Ito, K. (2016). A computational spinal motion segment model incorporating a matrix composition-based model of the intervertebral disc. Journal of the Mechanical Behavior of Biomedical Materials, 54, 194-204.

Baumgaertel, M., & Winter, H. H. (1992). Interrelation between continuous and discrete relaxation time spectra. Journal of Non-Newtonian Fluid Mechanics, 44, 15-36.

Becker, D. G., Ransom, E., Guy, C., & Bloom, J. (2010). Surgical treatment of nasal obstruction in rhinoplasty. Aesthetic Surgery Journal, 30(3), 347-378.

Beillas, P., Lee, S. W., Tashman, S., & Yang, K. H. (2007). Sensitivity of the tibio-femoral response to finite element modeling parameters. Computer Methods in Biomechanics and Biomedical Engineering, 10(3), 209-221.

Beillas, P., Papaioannou, G., Tashman, S., & Yang, K. H. (2004). A new method to investigate in vivo knee behavior using a finite element model of the lower limb. Journal of Biomechanics, 37(7), 1019-1030.

Bobacz, K., Erlacher, L., Smolen, J., Soleiman, A., & Graninger, W. B. (2004). Chondrocyte number and proteoglycan synthesis in the aging and osteoarthritic human articular cartilage. Annals of the Rheumatic Diseases, 63(12), 1618-1622.

Bonet, J., & Wood, R. D. (1997). Nonlinear continuum mechanics for finite element analysis. Cambridge University Press.

Bonifasi-Lista, C., Lakez, S. P., Small, M. S., & Weiss, J. A. (2005). Viscoelastic properties of the human medial collateral ligament under longitudinal, transverse and shear loading. Journal of Orthopaedic Research, 23(1), 67-76.

Borthakur, A., Mellon, E., Niyogi, S., Witschey, W., Kneeland, J. B., & Reddy, R. (2006). Sodium and T1ρ MRI for molecular and diagnostic imaging of articular cartilage. NMR in Biomedicine, 19(7), 781-821.

Boyer, G., Molimard, J., Tkaya, M. B., Zahouani, H., Pericoi, M., & Avril, S. (2013). Assessment of the in-plane biomechanical properties of human skin using a finite element model updating approach

combined with an optical full-field measurement on a new tensile device. Journal of the Mechanical Behavior of Biomedical Materials, 27, 273-282.

Brink, U., & Stein, E. (1996). On some mixed finite element methods for incompressible and nearly incompressible finite elasticity. Computational Mechanics, 19(1), 105-119.

Brostow, W., Datashvili, T., McCarty, R., & White, J. B. (2010). Copper viscoelasticity manifested in scratch recovery. Materials Chemistry and Physics, 124(1), 371-376.

Byrd, H. S., Meade, R. A., & Gonyon Jr, D. L. (2007). Using the autospreader flap in primary rhinoplasty. Plastic and Reconstructive Surgery, 119(6), 1897-1902.

Carew, E. O., Garg, A., Barber, J. E., & Vesely, I. (2004). Stress relaxation preconditioning of porcine aortic valves. Annals of Biomedical Engineering, 32(4), 563-572.

Castro, A. P. G., Wilson, W., Huyghe, J. M., Ito, K., & Alves, J. L. (2014). Intervertebral disc creep behavior assessment through an open source finite element solver. Journal of Biomechanics, 47(1), 297-301.

Chang, T. Y. P., Saleeb, A. F., & Li, G. (1991). Large strain analysis of rubber-like materials based on a perturbed Lagrangian variational principle. Computational Mechanics, 8(4), 221-233.

Chien, J. C. (1975). Solid-state characterization of the structure and property of collagen. Journal of Macromolecular Science — Reviews in Macromolecular Chemistry, 12(1), 1-80.

Choi, J. A., & Gold, G. E. (2011). MR imaging of articular cartilage physiology. Magnetic Resonance Imaging Clinics of North America, 19(2), 249-282.

Clark, J. M. (1985). The organization of collagen in cryofractured rabbit articular cartilage: a scanning electron microscopic study. Journal of Orthopaedic Research, 3(1), 17-29.

Cohen, N. P., Foster, R. J., & Mow, V. C. (1998). Composition and dynamics of articular cartilage: structure, function, and maintaining healthy state. Journal of Orthopaedic & Sports Physical Therapy, 28(4), 203-215.

Conesa, J. A., Fullana, A., & Font, R. (2003). Thermal decomposition of meat and bone meal. Journal of Analytical and Applied Pyrolysis, 70(2), 619-630.

Cortez, S., Completo, A., & Alves, J. L. (2016). A novel computational modelling to describe the anisotropic, remodelling and reorientation behaviour of collagen fibres in articular cartilage. *arXiv preprint arXiv:1601.05295*.

da Costa, A., Pereira, A., Gomes, A., Rodriguez-Cabello, J., Sencadas, V., Casal, M., & Machado, R. (2017). Single step fabrication of antimicrobial fibre mats from a bioengineered protein-based polymer. Biomedical Materials.

Daniel, R. K. (2009). Tip refinement grafts: the designer tip. Aesthetic Surgery Journal, 29(6), 528-537.

De Greef, D., Buytaert, J. A., Aerts, J. R., Van Hoorebeke, L., Dierick, M., & Dirckx, J. (2015). Details of human middle ear morphology based on micro-CT imaging of phosphotungstic acid stained samples. Journal of Morphology, 276(9), 1025-1046.

De Greef, D., Pires, F., & Dirckx, J. J. (2017). Effects of model definitions and parameter values in finite element modeling of human middle ear mechanics. Hearing Research, 344, 195-206.

DeRosa, J. (2016). Does the Nose Have a Function Beyond Breathing?. Facial Plastic Surgery, 32(01), 009-016.

Ding, C., Zhang, M., & Li, G. (2015). Effect of cyclic freeze–thawing process on the structure and properties of collagen. International Journal of Biological Macromolecules, 80, 317-323.

DiSilvestro, M. R., & Suh, J. K. F. (2002). Biphasic poroviscoelastic characteristics of proteoglycan-depleted articular cartilage: simulation of degeneration. Annals of Biomedical Engineering, 30(6), 792-800.

Doblaré, M., & García-Aznar, J. M. (2010). Modelling living tissues: mechanical and mechanobiological aspects. In Progress in Industrial Mathematics at ECMI 2008 (pp. 3-8). Springer Berlin Heidelberg.

Ehret, A. E., & Itskov, M. (2009). Modeling of anisotropic softening phenomena: application to soft biological tissues. International Journal of Plasticity, 25(5), 901-919.

Einat, R., & Yoram, L. (2009). Recruitment viscoelasticity of the tendon. Journal of Biomechanical Engineering, 131(11), 111008.

Espino, D. M., Shepherd, D. E., & Hukins, D. W. (2014). Viscoelastic properties of bovine knee joint articular cartilage: dependency on thickness and loading frequency. BMC Musculoskeletal Disorders, 15(1), 205.

Fallah, A., Ahmadian, M. T., Firozbakhsh, K., & Aghdam, M. M. (2016). Micromechanics and constitutive modeling of connective soft tissues. Journal of the Mechanical Behavior of Biomedical Materials, 60, 157-176.

Federico, S. (2010). Volumetric-distortional decomposition of deformation and elasticity tensor. Mathematics and Mechanics of Solids, 15(6), 672-690.

Fedok, F. G. (2016). Costal cartilage grafts in rhinoplasty. Clinics in Plastic Surgery, 43(1), 201-212.

Fedorov, A., Beichel, R., Kalpathy-Cramer, J., Finet, J., Fillion-Robin, J. C., Pujol, S., ... & Buatti, J. (2012). 3D Slicer as an image computing platform for the Quantitative Imaging Network. Magnetic Resonance Imaging, 30(9), 1323-1341.

Feng, Z. Q., Peyraut, F., & He, Q. C. (2006). Finite deformations of Ogden's materials under impact loading. International Journal of Non-Linear Mechanics, 41(4), 575-585.

Ferreira, M. G., Monteiro, D., Reis, C., & e Sousa, C. A. (2016). Spare Roof Technique: A Middle Third New Technique. Facial Plastic Surgery, 32(01), 111-116.

Ficai, A., Ficai, D., Andronescu, E., Maganu, M., Voicu, G., & Sonmez, M. (2011). Biomimetic mineralization of the human nasal septum cartilage. Digest Journal of Nanomaterials & Biostructures, 6(3).

Fortis, A. P., Kostopoulos, V., Panagiotopoulos, E., Tsantzalis, S., & Kokkinos, A. (2004). Viscoelastic properties of cartilage-subchondral bone complex in osteoarthritis. Journal of Medical Engineering & Technology, 28(5), 223-226.

Freutel, M., Schmidt, H., Dürselen, L., Ignatius, A., & Galbusera, F. (2014). Finite element modeling of soft tissues: material models, tissue interaction and challenges. Clinical Biomechanics, 29(4), 363-372.

Friedman, O., & Coblens, O. (2016). The conchal cartilage butterfly graft. Facial Plastic Surgery, 32(01), 042-048.

Frijns, A. J. H., Huyghe, J. M., & Janssen, J. D. (1997). A validation of the quadriphasic mixture theory for intervertebral disc tissue. International Journal of Engineering Science, 35(15), 1419-1429.

Fripp, J., Crozier, S., Warfield, S. K., & Ourselin, S. (2010). Automatic segmentation and quantitative analysis of the articular cartilages from magnetic resonance images of the knee. IEEE Transactions on Medical Imaging, 29(1), 55-64.

Fulcher, G. R., Hukins, D. W., & Shepherd, D. E. (2009). Viscoelastic properties of bovine articular cartilage attached to subchondral bone at high frequencies. BMC Musculoskeletal Disorders, 10(1), 61.

Fung, Y. C. (1993). Biomechanics: mechanical properties of living tissues. New York.

Gardiner, J. C., & Weiss, J. A. (2003). Subject-specific finite element analysis of the human medial collateral ligament during valgus knee loading. Journal of Orthopaedic Research, 21(6), 1098-1106.

Gasser, T. C., Ogden, R. W., & Holzapfel, G. A. (2006). Hyperelastic modelling of arterial layers with distributed collagen fibre orientations. Journal of the Royal Society Interface, 3(6), 15-35.

Gauvin, R., Parenteau-Bareil, R., Larouche, D., Marcoux, H., Bisson, F., Bonnet, A., ... & Germain, L. (2011). Dynamic mechanical stimulations induce anisotropy and improve the tensile properties of engineered tissues produced without exogenous scaffolding. Acta Biomaterialia, 7(9), 3294-3301.

Gniadecka, M. (1995). Non-invasive methods for determination of oedema and water behaviour in the skin. Skin Research and Technology, 1(2), 55-60.

Gray, L. P. (1978). Deviated nasal septum incidence and etiology. Annals of Otology, Rhinology & Laryngology, 87(3_suppl2), 3-20.

Griffin, M. F., Premakumar, Y., Seifalian, A. M., Szarko, M., & Butler, P. E. M. (2016). Biomechanical Characterisation of the Human Auricular Cartilages; Implications for Tissue Engineering. Annals of Biomedical Engineering, 44(12), 3460-3467.

Gruber, R. P., Melkun, E. T., Woodward, J. F., & Perkins, S. W. (2011). Dorsal reduction and spreader flaps. Aesthetic Surgery Journal, 31(4), 456-464.

Gruber, R. P., Park, E., Newman, J., Berkowitz, L., & Oneal, R. (2007). The spreader flap in primary rhinoplasty. Plastic and Reconstructive Surgery, 119(6), 1903-1910.

Gruber, R. P., & Perkins, S. W. (2010). Humpectomy and spreader flaps. Clinics in Plastic Surgery, 37(2), 285-291.

Gu, K. B., & Li, L. P. (2011). A human knee joint model considering fluid pressure and fiber orientation in cartilages and menisci. Medical Engineering & Physics, 33(4), 497-503.

Guo, H., Maher, S. A., & Torzilli, P. A. (2015). A biphasic finite element study on the role of the articular cartilage superficial zone in confined compression. Journal of Biomechanics, 48(1), 166-170.

Gupta, H. S., Seto, J., Krauss, S., Boesecke, P., & Screen, H. R. C. (2010). In situ multi-level analysis of viscoelastic deformation mechanisms in tendon collagen. Journal of Structural Biology, 169(2), 183-191.

Guyuron, B., DeLuca, L., & Lash, R. (2000). Supratip deformity: a closer look. Plastic and Reconstructive Surgery, 105(3), 1140-1151.

Hafezi, F., Naghibzadeh, B., & Nouhi, A. H. (2010). Applied anatomy of the nasal lower lateral cartilage: a new finding. Aesthetic Plastic Surgery, 34(2), 244-248.

Halonen, K. S., Mononen, M. E., Jurvelin, J. S., Töyräs, J., Salo, J., & Korhonen, R. K. (2014). Deformation of articular cartilage during static loading of a knee joint–experimental and finite element analysis. Journal of Biomechanics, 47(10), 2467-2474.

Hamilton III, G. S. (2016). Form and function of the nasal tip: reorienting and reshaping the lateral crus. Facial Plastic Surgery, 32(01), 049-058.

Han, S. K., Lee, D. G., Kim, J. B., & Kim, W. K. (2004). An anatomic study of nasal tip supporting structures. Annals of Plastic Surgery, 52(2), 134-139.

Haut Donahue, T. L., Hull, M. L., Rashid, M. M., & Jacobs, C. R. (2002). A finite element model of the human knee joint for the study of tibio-femoral contact. Journal of Biomechanical Engineering, 124(3), 273-280.

Haut Donahue, T. L., Hull, M. L., Rashid, M. M., & Jacobs, C. R. (2003). How the stiffness of meniscal attachments and meniscal material properties affect tibio-femoral contact pressure computed using a validated finite element model of the human knee joint. Journal of Biomechanics, 36(1), 19-34.

Havaldar, R., Pilli, S. C., & Putti, B. B. (2014). Insights into the effects of tensile and compressive loadings on human femur bone. Advanced Biomedical Research, 3.

Hawkes, D. J., Barratt, D., Blackall, J. M., Chan, C., Edwards, P. J., Rhode, K., ... & Hill, D. L. (2005). Tissue deformation and shape models in image-guided interventions: a discussion paper. Medical Image Analysis, 9(2), 163-175.

Hayes, W. C., & Bodine, A. J. (1978). Flow-independent viscoelastic properties of articular cartilage matrix. Journal of Biomechanics, 11(8-9), 407-419.

Hingorani, R. V., Provenzano, P. P., Lakes, R. S., Escarcega, A., & Vanderby, R. (2004). Nonlinear viscoelasticity in rabbit medial collateral ligament. Annals of Biomedical Engineering, 32(2), 306-312.

Hoch, D. H., Grodzinsky, A. J., Koob, T. J., Albert, M. L., & Eyre, D. R. (1983). Early changes in material properties of rabbit articular cartilage after meniscectomy. Journal of Orthopaedic Research, 1(1), 4-12.

Holmes, M. H., Lai, W. M., & Mow, V. C. (1985). Singular perturbation analysis of the nonlinear, flow-dependent compressive stress relaxation behavior of articular cartilage. Journal of Biomechanical Engineering, 107(3), 206-218.

Holmes, M. H., & Mow, V. C. (1990). The nonlinear characteristics of soft gels and hydrated connective tissues in ultrafiltration. Journal of Biomechanics, 23(11), 1145-1156.

Holzapfel, G. A. (2000a). Biomechanics of soft tissue. The handbook of materials behavior models, 3(1), 1049-1063.

Holzapfel, G. A. (2000b). Nonlinear Solid Mechanics: A Continuum Approach for Engineerring. Wiley.

Holzapfel, G. A., Gasser, T. C., & Ogden, R. W. (2000). A new constitutive framework for arterial wall mechanics and a comparative study of material models. Journal of Elasticity and the Physical Science of Solids, 61(1-3), 1-48.

Holzapfel, G. A., Gasser, T. C., & Stadler, M. (2002). A structural model for the viscoelastic behavior of arterial walls: continuum formulation and finite element analysis. European Journal of Mechanics-A/Solids, 21(3), 441-463.

Holzapfel, G. A., & Gasser, T. C. (2001). A viscoelastic model for fiber-reinforced composites at finite strains: Continuum basis, computational aspects and applications. Computer Methods in Applied Mechanics and Engineering, 190(34), 4379-4403.

Homicz, M. R., McGowan, K. B., Lottman, L. M., Beh, G., Sah, R. L., & Watson, D. (2003). A compositional analysis of human nasal septal cartilage. Archives of Facial Plastic Surgery, 5(1), 53-58.

Huda, W., & Slone, R. M. (2003). Review of radiologic physics. Lippincott Williams & Wilkins.

Huyghe, J. M., van Campen, D. H., Arts, T., & Heethaar, R. M. (1991). A two-phase finite element model of the diastolic left ventricle. Journal of Biomechanics, 24(7), 527-538.

Immerman, S., White, W. M., & Constantinides, M. (2011). Cartilage grafting in nasal reconstruction. Facial Plastic Surgery Clinics of North America, 19(1), 175-182.

Jaffe, F. F., Mankin, H. J., Weiss, H., & Zarins, A. (1974). Water binding in the articular cartilage of rabbits. Journal of Bone and Joint Surgery, 56(5), 1031-1039.

Jeffery, A. K., Blunn, G. W., Archer, C. W., & Bentley, G. (1991). Three-dimensional collagen architecture in bovine articular cartilage. Bone & Joint Journal, 73(5), 795-801.

Jeng, Y. R., Mao, C. P., & Wu, K. T. (2013). Instrumented indentation investigation on the viscoelastic properties of porcine cartilage. Journal of Bionic Engineering, 10(4), 522-531.

Joshi, M. D., Suh, J. K., Marui, T., & Woo, S. L. Y. (1995). Interspecies variation of compressive biomechanical properties of the meniscus. Journal of Biomedical Materials Research Part A, 29(7), 823-828.

Julkunen, P., Kiviranta, P., Wilson, W., Jurvelin, J. S., & Korhonen, R. K. (2007). Characterization of articular cartilage by combining microscopic analysis with a fibril-reinforced finite-element model. Journal of Biomechanics, 40(8), 1862-1870.

Julkunen, P., Wilson, W., Jurvelin, J. S., Rieppo, J., Qu, C. J., Lammi, M. J., & Korhonen, R. K. (2008). Stress–relaxation of human patellar articular cartilage in unconfined compression: prediction of mechanical response by tissue composition and structure. Journal of Biomechanics, 41(9), 1978-1986.

June, R. K., & Fyhrie, D. P. (2010). Temperature effects in articular cartilage biomechanics. Journal of Experimental Biology, 213(22), 3934-3940.

Kempson, G. E., Freeman, M. A. R., & Swanson, S. A. V. (1971). The determination of a creep modulus for articular cartilage from indentation tests on the human femoral head. Journal of Biomechanics, 4(4), 239-250.

Katz, E. P., & Li, S. T. (1973). The intermolecular space of reconstituted collagen fibrils. Journal of Molecular Biology, 73(3), 351-369.

Kelm, B. M., Wels, M., Zhou, S. K., Seifert, S., Suehling, M., Zheng, Y., & Comaniciu, D. (2013). Spine detection in CT and MR using iterated marginal space learning. Medical Image Analysis, 17(8), 1283-1292.

Kida, N., & Adachi, T. (2015). Finite element formulation and analysis for an arterial wall with residual and active stresses. Computer Methods in Biomechanics and Biomedical Engineering, 18(11), 1143-1159.

Kim, I. S., Chung, Y. J., & Lee, Y. I. (2008). An anatomic study on the overlap patterns of structural components in the keystone area in noses of Koreans. Clinical and Experimental Otorhinolaryngology, 1(3), 158.

Kim, J. H., Avril, S., Duprey, A., & Favre, J. P. (2012). Experimental characterization of rupture in human aortic aneurysms using a full-field measurement technique. Biomechanics and Modeling in Mechanobiology, 11(6), 841-853.

Kim, L., & Papel, I. D. (2016). Spreader grafts in functional rhinoplasty. Facial Plastic Surgery, 32(01), 029-035.

Koch, R. J., Chavez, A., Dagum, P., & Newman, J. P. (1998). Advantages and disadvantages of computer imaging in cosmetic surgery. Dermatologic Surgery, 24(2), 195-198.

Koupai, S. A., Bakhshi, A., & Tabrizi, V. V. (2017). Experimental investigation on effects of elastomer components on dynamic and mechanical properties in seismic isolator compounds. Construction and Building Materials, 135, 267-278.

Kovacevic, M., Riedel, F., Göksel, A., & Wurm, J. (2016). Options for middle vault and dorsum restoration after hump removal in primary rhinoplasty. Facial Plastic Surgery, 32(04), 374-383.

Kovacevic, M., & Wurm, J. (2015). Spreader flaps for middle vault contour and stabilization. Facial Plastic Surgery Clinics, 23(1), 1-9.

Kutubidze, A. (2015). Nasal dorsal aesthetic lines and rhinoplasty technical tricks. Plastic and Aesthetic Research, 2, 315-319.

Kwan, M. K., Lai, W. M., & Mow, V. C. (1990). A finite deformation theory for cartilage and other soft hydrated connective tissues—I. Equilibrium results. Journal of Biomechanics, 23(2), 145-155.

Lai, W. M., Hou, J. S., & Mow, V. C. (1991). A triphasic theory for the swelling and deformation behaviors of articular cartilage. Journal of Biomechanical Engineering, 113(3), 245-258.

Lai, W. M., Mow, V., & Roth, V. (1981). Effects of nonlinear strain-dependent permeability and rate of compression on the stress behavior of articular cartilage. Journal of Biomechanical Engineering, 103, 61.

Lai, W. M., Rubin, D. H., Rubin, D., & Krempl, E. (2009). Introduction to continuum mechanics. Butterworth-Heinemann.

Lakes, R. S. (2009). Viscoelastic materials. Cambridge University Press.

Lang, U., Naujoks, N., & Dual, J. (2009). Mechanical characterization of PEDOT: PSS thin films. Synthetic Metals, 159(5), 473-479.

Latorre, M., Romero, X., & Montáns, F. J. (2016). The relevance of transverse deformation effects in modeling soft biological tissues. International Journal of Solids and Structures, 99, 57-70.

Lee, S. (2004). Three-dimensional photography and its application to facial plastic surgery. Archives of Facial Plastic Surgery, 6(6), 410-414.

Lessard, M. L., & Daniel, R. K. (1985). Surgical anatomy of septorhinoplasty. Archives of Otolaryngology, 111(1), 25-29.

Letourneau, A., & Daniel, R. K. (1988). The superficial musculoaponeurotic system of the nose. Plastic and Reconstructive Surgery, 82(1), 48-55.

Lekakis, G., Claes, P., Hamilton III, G. S., & Hellings, P. W. (2016a). Evolution of preoperative rhinoplasty consult by computer imaging. Facial Plastic Surgery, 32(01), 080-087.

Lekakis, G., Claes, P., Hamilton III, G. S., & Hellings, P. W. (2016b). Three-dimensional surface imaging and the continuous evolution of preoperative and postoperative assessment in rhinoplasty. Facial Plastic Surgery, 32(01), 088-094.

Li, G., Gil, J., Kanamori, A., & Woo, S. Y. (1999). A validated three-dimensional computational model of a human knee joint. Journal of Biomechanical Engineering, 121(6), 657-662.

Li, H., & Wang, Z. (2006). Intervertebral disc biomechanical analysis using the finite element modeling based on medical images. Computerized Medical Imaging and Graphics, 30(6), 363-370.

Li, L. P., Herzog, W., Korhonen, R. K., & Jurvelin, J. S. (2005). The role of viscoelasticity of collagen fibers in articular cartilage: axial tension versus compression. Medical Engineering & Physics, 27(1), 51-57.

Li, L. P., Korhonen, R. K., Iivarinen, J., Jurvelin, J. S., & Herzog, W. (2008). Fluid pressure driven fibril reinforcement in creep and relaxation tests of articular cartilage. Medical Engineering & Physics, 30(2), 182-189.

Limbert, G., & Middleton, J. (2004). A transversely isotropic viscohyperelastic material: application to the modeling of biological soft connective tissues. International Journal of Solids and Structures, 41(15), 4237-4260.

Lukeš, V., & Rohan, E. (2010). Microstructure based two-scale modelling of soft tissues. Mathematics and Computers in Simulation, 80(6), 1289-1301.

Maas, S., Rawlins, D., Weiss, J. A., & Ateshian, G. A. (2011). FEBio: Finite Elements for Biomechanics, Theory Manual.

Majda, D., Bhattarai, A., Riikonen, J., Napruszewska, B. D., Zimowska, M., Michalik-Zym, A., ... & Lehto, V. P. (2017). New approach for determining cartilage pore size distribution: NaCl-thermoporometry. Microporous and Mesoporous Materials, 241, 238-245.

Mak, A. F. (1986). The apparent viscoelastic behavior of articular cartilage—the contributions from the intrinsic matrix viscoelasticity and interstitial fluid flows. Journal of Biomechanical Engineering, 108(2), 123-130.

Mak, A. F., Lai, W. M., & Mow, V. C. (1987). Biphasic indentation of articular cartilage—I. Theoretical analysis. Journal of Biomechanics, 20(7), 703-714.

Marchesseau, S., Heimann, T., Chatelin, S., Willinger, R., & Delingette, H. (2010). Fast porous visco-hyperelastic soft tissue model for surgery simulation: application to liver surgery. Progress in Biophysics and Molecular Biology, 103(2), 185-196.

Maroudas, A. (1976). Balance between swelling pressure and collagen tension in normal and degenerate cartilage. Nature, 260(5554), 808-809.

Martinho, A. C., Alves-Claro, A. R., Pino, E. S., Machado, L. D. B., Herson, M. R., Santin, S. P., & Mathor, M. B. (2013). Effects of ionizing radiation and preservation on biomechanical properties of human costal cartilage. Cell and Tissue Banking, 14(1), 117-124.

Menard, K. P. (2008). Dynamic mechanical analysis: a practical introduction. CRC Press.

Mijailovich, S. M., Stamenovic, D. I., & Fredberg, J. J. (1993). Toward a kinetic theory of connective tissue micromechanics. Journal of Applied Physiology, 74(2), 665-681.

Mkukuma, L. D., Skakle, J. M. S., Gibson, I. R., Imrie, C. T., Aspden, R. M., & Hukins, D. W. L. (2004). Effect of the proportion of organic material in bone on thermal decomposition of bone mineral: an investigation of a variety of bones from different species using thermogravimetric analysis coupled to mass spectrometry, high-temperature X-ray diffraction, and Fourier transform infrared spectroscopy. Calcified Tissue International, 75(4), 321-328.

Mononen, M. E., Mikkola, M. T., Julkunen, P., Ojala, R., Nieminen, M. T., Jurvelin, J. S., & Korhonen, R. K. (2012). Effect of superficial collagen patterns and fibrillation of femoral articular cartilage on knee joint mechanics—a 3D finite element analysis. Journal of Biomechanics, 45(3), 579-587.

Mooney, M. (1940). A theory of large elastic deformation. Journal of Applied Physics, 11(9), 582-592.

Moraes, M. R., Alves, A. C., Toptan, F., Martins, M. S., Vieira, E. M., Paleo, A. J., ... & Zille, A. (2017). Glycerol/PEDOT: PSS coated woven fabric as a flexible heating element on textiles. Journal of Materials Chemistry C, 5(15), 3807-3822.

Moubayed, S. P., & Most, S. P. (2016). The autospreader flap for midvault reconstruction following dorsal hump resection. Facial Plastic Surgery, 32(01), 036-041.

Mow, V. C., Gibbs, M. C., Lai, W. M., Zhu, W. B., & Athanasiou, K. A. (1989). Biphasic indentation of articular cartilage—II. A numerical algorithm and an experimental study. Journal of Biomechanics, 22(8-9), 853-861.

Mow, V. C., Kuei, S. C., Lai, W. M., & Armstrong, C. G. (1980). Biphasic creep and stress relaxation of articular cartilage in compression: theory and experiments. Journal of Biomechanical Engineering, 102(1), 73-84.

Nagasawa, K., Noguchi, M., Ikoma, K., & Kubo, T. (2008). Static and dynamic biomechanical properties of the regenerating rabbit Achilles tendon. Clinical Biomechanics, 23(6), 832-838.

Natali, A. N., Pavan, P. G., Venturato, C., & Komatsu, K. (2011). Constitutive modeling of the non-linear visco-elasticity of the periodontal ligament. Computer Methods and Programs in Biomedicine, 104(2), 193-198.

Natvig, P., Sether, L. A., Gingrass, R. P., & Gardner, W. D. (1971). Anatomical details of the osseous-cartilaginous framework of the nose. Plastic and Reconstructive Surgery, 48(6), 528-532.

Nava, A., Mazza, E., Haefner, O., & Bajka, M. (2004). Experimental observation and modelling of preconditioning in soft biological tissues. Medical Simulation, 1-8.

Nicolle, S., Vezin, P., & Palierne, J. F. (2010). A strain-hardening bi-power law for the nonlinear behaviour of biological soft tissues. Journal of Biomechanics, 43(5), 927-932.

Nimeskern, L., Pleumeekers, M. M., Pawson, D. J., Koevoet, W. L., Lehtoviita, I., Soyka, M. B., ... & Stok, K. S. (2015). Mechanical and biochemical mapping of human auricular cartilage for reliable assessment of tissue-engineered constructs. Journal of Biomechanics, 48(10), 1721-1729.

Noailly, J., Van Oosterwyck, H., Wilson, W., Quinn, T. M., & Ito, K. (2008). A poroviscoelastic description of fibrin gels. Journal of Biomechanics, 41(15), 3265-3269.

Novitskaya, E., Zin, C., Chang, N., Cory, E., Chen, P., D'Lima, D., ... & McKittrick, J. (2014). Creep of trabecular bone from the human proximal tibia. Materials Science and Engineering: C, 40, 219-227.

Okamoto, Y., & Saeki, K. (1964). Phase transition of collagen and gelatin. Colloid & Polymer Science, 194(2), 124-135.

Oneal, R. M., & Beil, R. J. (2010). Surgical anatomy of the nose. Clinics in Plastic Surgery, 37(2), 191.

Öztürk, C. N., & Albayrak, S. (2016). Automatic segmentation of cartilage in high-field magnetic resonance images of the knee joint with an improved voxel-classification-driven region-growing algorithm using vicinity-correlated subsampling. Computers in Biology and Medicine, 72, 90-107.

Palhazi, P., Daniel, R. K., & Kosins, A. M. (2015). The osseocartilaginous vault of the nose: anatomy and surgical observations. Aesthetic Surgery Journal, 35(3), 242-251.

Park, S., Hung, C. T., & Ateshian, G. A. (2004). Mechanical response of bovine articular cartilage under dynamic unconfined compression loading at physiological stress levels. Osteoarthritis and Cartilage, 12(1), 65-73.

Pearson, B., & Espino, D. M. (2013). Effect of hydration on the frequency-dependent viscoelastic properties of articular cartilage. Proceedings of the Institution of Mechanical Engineers, Part H: Journal of Engineering in Medicine, 227(11), 1246-1252.

Peña, E. (2014). Computational aspects of the numerical modelling of softening, damage and permanent set in soft biological tissues. Computers & Structures, 130, 57-72.

Peña, E., Calvo, B., Martinez, M. A., Palanca, D., & Doblaré, M. (2005b). Finite element analysis of the effect of meniscal tears and meniscectomies on human knee biomechanics. Clinical Biomechanics, 20(5), 498-507.

Peña, E., Calvo, B., Martinez, M. A., & Doblare, M. (2006). A three-dimensional finite element analysis of the combined behavior of ligaments and menisci in the healthy human knee joint. Journal of Biomechanics, 39(9), 1686-1701.

Peña, E., Calvo, B., Martínez, M. A., & Doblaré, M. (2007a). Effect of the size and location of osteochondral defects in degenerative arthritis. A finite element simulation. Computers in Biology and Medicine, 37(3), 376-387.

Peña, E., Calvo, B., Martinez, M. A., & Doblaré, M. (2007b). An anisotropic visco-hyperelastic model for ligaments at finite strains. Formulation and computational aspects. International Journal of Solids and Structures, 44(3), 760-778.

Peña, E., Martinez, M. A., Calvo, B., Palanca, D., & Doblaré, M. (2005a). A finite element simulation of the effect of graft stiffness and graft tensioning in ACL reconstruction. Clinical Biomechanics, 20(6), 636-644.

Peña, E., Peña, J. A., & Doblare, M. (2008). On modelling nonlinear viscoelastic effects in ligaments. Journal of Biomechanics, 41(12), 2659-2666.

Périé, D., & Hobatho, M. C. (1998). In vivo determination of contact areas and pressure of the femorotibial joint using non-linear finite element analysis. Clinical Biomechanics, 13(6), 394-402.

Pietrucha, K. (2007). Some Biological and Thermoanalytical Studies of Cross-linked Collagen Sponges. In World Congress on Medical Physics and Biomedical Engineering 2006 (pp. 3369-3372). Springer, Berlin, Heidelberg.

Poole, C. A. (1997). Articular cartilage chondrons: form, function and failure. The Journal of Anatomy, 191(1), 1-13.

Poole, C. A., Flint, M. H., & Beaumont, B. W. (1987). Chondrons in cartilage: ultrastructural analysis of the pericellular microenvironment in adult human articular cartilages. Journal of Orthopaedic Research, 5(4), 509-522.

Purslow, P. P., Wess, T. J., & Hukins, D. W. (1998). Collagen orientation and molecular spacing during creep and stress-relaxation in soft connective tissues. Journal of Experimental Biology, 201(1), 135-142.

Puso, M. A., & Weiss, J. A. (1998). Finite element implementation of anisotropic quasi-linear viscoelasticity using a discrete spectrum approximation. Journal of Biomechanical Engineering, 120(1), 62-70.

Quatela, V. C., Leake, D. S., & Sabini, P. (2004). Surgical management of concavities of the distal nose. Facial Plastic Surgery Clinics of North America, 12(1), 133-156.

Quinn, T. M., Dierickx, P., & Grodzinsky, A. J. (2001). Glycosaminoglycan network geometry may contribute to anisotropic hydraulic permeability in cartilage under compression. Journal of Biomechanics, 34(11), 1483-1490.

Quinn, T. M., & Morel, V. (2007). Microstructural modeling of collagen network mechanics and interactions with the proteoglycan gel in articular cartilage. Biomechanics and Modeling in Mechanobiology, 6(1), 73-82.

Rahimi, M. H., Parvinzadeh, M., Navid, M. Y., & Ahmadi, S. (2011). Thermal characterization and flammability of polyester fiber coated with nonionic and cationic softeners. Journal of Surfactants and Detergents, 14(4), 595-603.

Rajagopal, K. R., & Wineman, A. S. (2008). A quasi-correspondence principle for Quasi-Linear viscoelastic solids. Mechanics of Time-Dependent Materials, 12(1), 1-14.

Ramaniraka, N. A., Saunier, P., Siegrist, O., & Pioletti, D. P. (2007). Biomechanical evaluation of intra-articular and extra-articular procedures in anterior cruciate ligament reconstruction: a finite element analysis. Clinical Biomechanics, 22(3), 336-343.

Ramprasad, V. H., & Frank-Ito, D. O. (2016). A computational analysis of nasal vestibule morphologic variabilities on nasal function. Journal of Biomechanics, 49(3), 450-457.

Ratner, B. D., Hoffman, A. S., Schoen, F. J., Lemons, J. E. (2004) Biomaterials Science: An Introduction to Materials in Medicine (2nd Edition). Elsevier Academic Press, California.

Ravikumar, K. M., & Hwang, W. (2008). Region-specific role of water in collagen unwinding and assembly. Proteins: Structure, Function, and Bioinformatics, 72(4), 1320-1332.

Recker, C., & Hamilton III, G. S. (2016). Evaluation of the Patient with Nasal Obstruction. Facial Plastic Surgery, 32(01), 003-008.

Reynaud, B., & Quinn, T. M. (2006). Anisotropic hydraulic permeability in compressed articular cartilage. Journal of Biomechanics, 39(1), 131-137.

Richard, F., Villars, M., & Thibaud, S. (2013). Viscoelastic modeling and quantitative experimental characterization of normal and osteoarthritic human articular cartilage using indentation. Journal of the Mechanical Behavior of Biomedical Materials, 24, 41-52.

Rohrich, R. J., Muzaffar, A. R., & Janis, J. E. (2004). Component dorsal hump reduction: the importance of maintaining dorsal aesthetic lines in rhinoplasty. Plastic and Reconstructive Surgery, 114(5), 1298-1308.

Ronken, S., Arnold, M. P., Garcia, H. A., Jeger, A., Daniels, A. U., & Wirz, D. (2012). A comparison of healthy human and swine articular cartilage dynamic indentation mechanics. Biomechanics and Modeling in Mechanobiology, 11(5), 631-639.

Rotter, N., Tobias, G., Lebl, M., Roy, A. K., Hansen, M. C., Vacanti, C. A., & Bonassar, L. J. (2002). Age-related changes in the composition and mechanical properties of human nasal cartilage. Archives of Biochemistry and Biophysics, 403(1), 132-140.

Roylance, D. (2001). Engineering viscoelasticity. Department of Materials Science and Engineering–Massachusetts Institute of Technology, Cambridge MA, 2139, 1-37.

Sadeghi, H., Espino, D. M., & Shepherd, D. E. (2015). Variation in viscoelastic properties of bovine articular cartilage below, up to and above healthy gait-relevant loading frequencies. Proceedings of the Institution of Mechanical Engineers, Part H: Journal of Engineering in Medicine, 229(2), 115-123.

Safadi, M. M., & Rubin, M. B. (2014). Modeling rate-independent hysteresis in large deformations of preconditioned soft tissues. International Journal of Solids and Structures, 51(18), 3265-3272.

Sajjadian, A., & Guyuron, B. (2010). Primary rhinoplasty. Aesthetic Surgery Journal, 30(4), 527-539.

Samouillan, V., Dandurand-Lods, J., Lamure, A., Maurel, E., Lacabanne, C., Gerosa, G., ... & Spina, M. (1999). Thermal analysis characterization of aortic tissues for cardiac valve bioprostheses. Journal of Biomedical Materials Research, 46(4), 531-538.

Sands, N. B., & Adamson, P. A. (2015). Nasal tip deprojection with crural cartilage overlap: the M-arch model. Facial Plastic Surgery Clinics of North America, 23(1), 93-104.

Sauren, A. A. H. J., Huson, A., & Schouten, R. Y. (1984). An axisymmetric finite element analysis of the mechanical function of the meniscus. International Journal of Sports Medicine, 5(S 1), S93-S95.

Sayed, T. E., Mota, A., Fraternali, F., & Ortiz, M. (2008). A variational constitutive model for soft biological tissues. Journal of Biomechanics, 41(7), 1458-1466.

Schmidt, H., Shirazi-Adl, A., Galbusera, F., & Wilke, H. J. (2010). Response analysis of the lumbar spine during regular daily activities—a finite element analysis. Journal of Biomechanics, 43(10), 1849-1856.

Schmidt, M. B., Mow, V. C., Chun, L. E., & Eyre, D. R. (1990). Effects of proteoglycan extraction on the tensile behavior of articular cartilage. Journal of Orthopaedic Research, 8(3), 353-363.

Schmidt, T., Balzani, D., & Holzapfel, G. A. (2014). Statistical approach for a continuum description of damage evolution in soft collagenous tissues. Computer Methods in Applied Mechanics and Engineering, 278, 41-61.

Schreppers, G. J. M. A., Sauren, A. A. H. J., & Huson, A. (1990). A numerical model of the load transmission in the tibio-femoral contact area. Proceedings of the Institution of Mechanical Engineers, Part H: Journal of Engineering in Medicine, 204(1), 53-59.

Schröder, J., & Neff, P. (2003). Invariant formulation of hyperelastic transverse isotropy based on polyconvex free energy functions. International Journal of Solids and Structures, 40(2), 401-445.

Schwartz, C. J., & Bahadur, S. (2007). Investigation of articular cartilage and counterface compliance in multi-directional sliding as in orthopedic implants. Wear, 262(11), 1315-1320.

Screen, H. R. C., Toorani, S., & Shelton, J. C. (2013). Microstructural stress relaxation mechanics in functionally different tendons. Medical Engineering & Physics, 35(1), 96-102.

Seifzadeh, A., Oguamanam, D. C. D., Trutiak, N., Hurtig, M., & Papini, M. (2012). Determination of nonlinear fibre-reinforced biphasic poroviscoelastic constitutive parameters of articular cartilage using stress relaxation indentation testing and an optimizing finite element analysis. Computer Methods and Programs in Biomedicine, 107(2), 315-326.

Seifzadeh, A., Wang, J., Oguamanam, D. C. D., & Papini, M. (2011). A nonlinear biphasic fiber-reinforced porohyperviscoelastic model of articular cartilage incorporating fiber reorientation and dispersion. Journal of Biomechanical Engineering, 133(8), 081004.

Seitz, A. M., Galbusera, F., Krais, C., Ignatius, A., & Dürselen, L. (2013). Stress-relaxation response of human menisci under confined compression conditions. Journal of the Mechanical Behavior of Biomedical Materials, 26, 68-80.

Sheen, J. H. (1984). Spreader graft: a method of reconstructing the roof of the middle nasal vault following rhinoplasty. Plastic and Reconstructive Surgery, 73(2), 230-237.

Simo, J. C., & Taylor, R. L. (1991). Quasi-incompressible finite elasticity in principal stretches. Continuum basis and numerical algorithms. Computer Methods in Applied Mechanics and Engineering, 85(3), 273-310.

Simon, B. R. (1992). Multiphase poroelastic finite element models for soft tissue structures. Applied Mechanics Reviews, 45(6), 191-218.

Sozansky, J., & Houser, S. M. (2015). Pathophysiology of empty nose syndrome. The Laryngoscope, 125(1), 70-74.

Spahn, G., Plettenberg, H., Nagel, H., Kahl, E., Klinger, H. M., Günther, M., ... & Hofmann, G. O. (2006). Karl Fischer titration and coulometry for measurement of water content in small cartilage specimens/Bestimmung des Wassergehalts in kleinen Knorpelproben durch Karl-Fischer-Titration und Coulometrie. Biomedizinische Technik, 51(5/6), 355-359.

Spencer, A. J. M. (1970). The static theory of finite elasticity. IMA Journal of Applied Mathematics, 6(2), 164-200.

Spilker, R. L., Donzelli, P. S., & Mow, V. C. (1992). A transversely isotropic biphasic finite element model of the meniscus. Journal of Biomechanics, 25(9), 1027-1045.

Spilker, R. L., Suh, J. K., & Mow, V. C. (1992). A finite element analysis of the indentation stress-relaxation response of linear biphasic articular cartilage. Journal of Biomechanical Engineering, 114(2), 191-201.

Spilker, R. L., & Suh, J. K. (1990). Formulation and evaluation of a finite element model for the biphasic model of hydrated soft tissues. Computers & Structures, 35(4), 425-439.

Stevens, M. R., & Emam, H. A. (2012). Applied surgical anatomy of the nose. Oral and Maxillofacial Surgery Clinics of North America, 24(1), 25-38.

Stolz, M., Raiteri, R., Daniels, A. U., VanLandingham, M. R., Baschong, W., & Aebi, U. (2004). Dynamic elastic modulus of porcine articular cartilage determined at two different levels of tissue organization by indentation-type atomic force microscopy. Biophysical Journal, 86(5), 3269-3283.

Sugavaneswaran, M., & Arumaikkannu, G. (2014). Modelling for randomly oriented multi material additive manufacturing component and its fabrication. Materials & Design, 54, 779-785.

Sussman, T., & Bathe, K. J. (1987). A finite element formulation for nonlinear incompressible elastic and inelastic analysis. Computers & Structures, 26(1-2), 357-409.

Taffetani, M., Griebel, M., Gastaldi, D., Klisch, S. M., & Vena, P. (2014). Poroviscoelastic finite element model including continuous fiber distribution for the simulation of nanoindentation tests on articular cartilage. Journal of the Mechanical Behavior of Biomedical Materials, 32, 17-30.

Tanaka, E., Yamano, E., Dalla-Bona, D. A., Watanabe, M., Inubushi, T., Shirakura, M., ... & Tanne, K. (2006). Dynamic compressive properties of the mandibular condylar cartilage. Journal of Dental Research, 85(6), 571-575.

Temple, D. K., Cederlund, A. A., Lawless, B. M., Aspden, R. M., & Espino, D. M. (2016). Viscoelastic properties of human and bovine articular cartilage: a comparison of frequency-dependent trends. BMC Musculoskeletal Disorders, 17(1), 419.

Teng, Z., Tang, D., Zheng, J., Woodard, P. K., & Hoffman, A. H. (2009). An experimental study on the ultimate strength of the adventitia and media of human atherosclerotic carotid arteries in circumferential and axial directions. Journal of Biomechanics, 42(15), 2535-2539.

Thibbotuwawa, N., Oloyede, A., Senadeera, W., Li, T., & Gu, Y. (2015). Investigation of the mechanical behavior of kangaroo humeral head cartilage tissue by a porohyperelastic model based on the strain-rate-dependent permeability. Journal of the Mechanical Behavior of Biomedical Materials, 51, 248-259.

Thomas, L. W. (1962). The chemical composition of adipose tissue of man and mice. Experimental Physiology, 47(2), 179-188.

Thornton, G. M., Frank, C. B., & Shrive, N. G. (2001). Ligament creep behavior can be predicted from stress relaxation by incorporating fiber recruitment. Journal of Rheology, 45(2), 493-507.

Tong, P., & Fung, Y. C. (1976). The stress-strain relationship for the skin. Journal of Biomechanics, 9(10), 649-657.

Torzilli, P. A. (1985). Influence of cartilage conformation on its equilibrium water partition. Journal of Orthopaedic Research, 3(4), 473-483.

Tóth, K., Aigner, Z., Wellinger, K., Szabó-Révész, P., & Sohár, G. (2010). Thermoanalytical investigation of different hip joint arthropathies. Thermochimica Acta, 506(1), 94-97.

Tóth, K., Sohár, G., Pallagi, E., & Szabó-Révész, P. (2007). Further characterization of degenerated human cartilage with differential scanning calorimetry. Thermochimica Acta, 464(1), 75-77.

Tyndyk, M. A., Barron, V., McHugh, P. E., & O Mahoney, D. (2007). Generation of a finite element model of the thoracolumbar spine. Acta of Bioengineering and Biomechanics, 9(1), 35.

Vadher, S. P., Nayeb-Hashemi, H., Canavan, P. K., & Warner, G. M. (2006). Finite element modeling following partial meniscectomy: effect of various size of resection. In Engineering in Medicine and Biology Society, 2006. EMBS'06. 28th Annual International Conference of the IEEE (pp. 2098-2101). IEEE.

van den Bogert, P. A. J., De Borst, R., Luiten, G. T., & Zeilmaker, J. (1991). Robust finite elements for 3D-analysis of rubber-like materials. Engineering Computations, 8(1), 3-17.

van Loon, R., Huyghe, J. M., Wijlaars, M. W., & Baaijens, F. P. T. (2003). 3D FE implementation of an incompressible quadriphasic mixture model. International Journal for Numerical Methods in Engineering, 57(9), 1243-1258.

Vena, P., Franzoso, G., Gastaldi, D., Contro, R., & Dallolio, V. (2005). A finite element model of the L4–L5 spinal motion segment: biomechanical compatibility of an interspinous device. Computer Methods in Biomechanics and Biomedical Engineering, 8(1), 7-16.

Weiss, J. A., Gardiner, J. C., Ellis, B. J., Lujan, T. J., & Phatak, N. S. (2005). Three-dimensional finite element modeling of ligaments: technical aspects. Medical Engineering & Physics, 27(10), 845-861.

Weiss, J. A., & Gardiner, J. C. (2001). Computational modeling of ligament mechanics. Critical Reviews in Biomedical Engineering, 29(3).

Wilcox, A. G., Buchan, K. G., & Espino, D. M. (2014). Frequency and diameter dependent viscoelastic properties of mitral valve chordae tendineae. Journal of the Mechanical Behavior of Biomedical Materials, 30, 186-195.

Willing, R. T., Lalone, E. A., Shannon, H., Johnson, J. A., & King, G. J. (2013). Validation of a finite element model of the human elbow for determining cartilage contact mechanics. Journal of Biomechanics, 46(10), 1767-1771.

Wilson, W., Van Donkelaar, C. C., Van Rietbergen, B., Ito, K., & Huiskes, R. (2004). Stresses in the local collagen network of articular cartilage: a poroviscoelastic fibril-reinforced finite element study. Journal of Biomechanics, 37(3), 357-366.

Wilson, W., Van Donkelaar, C. C., Van Rietbergen, B., & Huiskes, R. (2005a). A fibril-reinforced poroviscoelastic swelling model for articular cartilage. Journal of biomechanics, 38(6), 1195-1204.

Wilson, W., Van Donkelaar, C. C., & Huyghe, J. M. (2005b). A comparison between mechano-electrochemical and biphasic swelling theories for soft hydrated tissues. Transactions of the ASME-K-Journal of Biomechanical Engineering, 127(1), 158-165.

Wurm, J., & Kovacevic, M. (2013). A new classification of spreader flap techniques. Facial Plastic Surgery, 29(06), 506-514.

Xia, Y., Moody, J. B., Burton-Wurster, N., & Lust, G. (2001). Quantitative in situ correlation between microscopic MRI and polarized light microscopy studies of articular cartilage. Osteoarthritis and Cartilage, 9(5), 393-406.

Yeh, C. H., Su, F. C., Goryacheva, I., Martynenko, Y., Dosaev, M. Z., & Ju, M. S. (2014). Image-assisted method for estimating local stiffness of soft tissues and calibration of bias due to aqueous humor effect. Sensors and Actuators A: Physical, 212, 42-51.

Yin, Y., Zhang, X., Williams, R., Wu, X., Anderson, D. D., & Sonka, M. (2010). LOGISMOS—layered optimal graph image segmentation of multiple objects and surfaces: cartilage segmentation in the knee joint. IEEE Transactions on Medical Imaging, 29(12), 2023-2037.

Zanjani-Pour, S., Winlove, C. P., Smith, C. W., & Meakin, J. R. (2016). Image driven subject-specific finite element models of spinal biomechanics. Journal of Biomechanics, 49(6), 919-925.

Zhang, X., Gao, X., Zhang, P., Guo, Y., Lin, H., Diao, X., ... & Chen, X. (2017). Dynamic mechanical analysis to assess viscoelasticity of liver tissue in a rat model of nonalcoholic fatty liver disease. Medical Engineering & Physics, 44, 79-86.

Zhou, J., Aguilar Ventura, I., & Lubineau, G. (2014). Probing the role of poly (3, 4-ethylenedioxythiophene)/poly (styrenesulfonate)-coated multiwalled carbon nanotubes in the thermal and mechanical properties of polycarbonate nanocomposites. Industrial & Engineering Chemistry Research, 53(9), 3539-3549.

Zhu, Y., Kang, G., Yu, C., & Poh, L. H. (2016). Logarithmic rate based elasto-viscoplastic cyclic constitutive model for soft biological tissues. Journal of the Mechanical Behavior of Biomedical Materials, 61, 397-409.